Multimodal Characterization of the Atrial Substrate

Risks and Rewards of Electrogram and Impedance Mapping

Zur Erlangung des akademischen Grades einer

DOKTORIN DER INGENIEURWISSENSCHAFTEN (Dr.-Ing.)

von der KIT-Fakultät für Elektrotechnik und Informationstechnik des

Karlsruher Instituts für Technologie (KIT)

angenommene

DISSERTATION

von

Laura Anna Unger, M.Sc.

geb. in Karlsruhe

Tag der mündlichen Prüfung:	22. Februar 2022
Hauptreferent:	Prof. Dr. rer. nat. Olaf Dössel
Korreferent:	PD Dr. med. Armin Luik

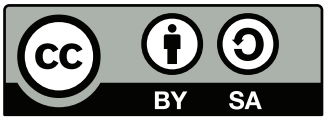

Abstract

The treatment of atrial rhythm disorders such as atrial fibrillation has remained a major challenge predominantly for patients with severely remodeled substrate. Individualized ablation strategies beyond pulmonary vein isolation in combination with real-time assessment of ablation lesion formation have been striven for insistently. Current approaches for identifying arrhythmogenic regions predominantly rely on electrogram-based features such as activation time and voltage or electrogram fractionation as a surrogate for tissue pathology. Despite bending every effort, large-scale clinical trials have yielded ambiguous results on the efficacy of various substrate mapping approaches without significant improvement of patient outcomes.

This work focuses on enhancing the understanding of electrogram features and local impedance measurements in the atria towards the extraction of clinically relevant and predictive substrate characteristics.

Features were extracted from intra-atrial electrograms with particular reference to the underlying excitation patterns to address morphological alterations caused by structural and functional changes. The noise level of unipolar electrograms was estimated and reduced by tailored filtering to enhance unipolar signal quality. Electrogram features exhibited narrow distributions for healthy substrate across patients while a wide range was observed for pathologically altered excitation.

Additionally, local impedance was investigated as a novel parameter and mapping modality. Having been introduced to the medical device market recently for monitoring ablative lesion formation, initial clinical experiences with local impedance-enabled catheters lack complementary systematic investigations. Confounding factors and the potential for application as a tool for substrate mapping need elucidation. This work pursued a trimodal approach combining *in human*, *in vitro*, and *in silico* experiments to quantitatively understand the effect of distinct ambient conditions on the measured local impedance. Forward simulations of the spread of the electrical field with a finite element approach as well as the application of inverse solution methods to reconstruct tissue conductivity were implemented *in silico*. Adequate preprocessing steps were developed for measurements *in human* to eliminate artefacts automatically. Two clinical studies on local impedance as an indicator for ablation lesion formation and on local impedance based substrate mapping were conducted. Local impedance recordings identified both previously ablated and native scar areas irrespective of local excitation. A highly detailed *in silico* environment for local impedance measurements

was validated with *in vitro* recordings and provided quantitative insights into the influence of changes in clinically relevant scenarios. Inverse reconstruction of relative tissue conductivity yielded promising results *in silico*.

This work demonstrates that local impedance mapping shows great potential to complement electrogram-based substrate mapping. A validated *in silico* environment for local impedance measurements can facilitate and optimize the development of next generation local impedance-enabled catheters. Conduction velocity, electrogram features, and reconstructed tissue conductivity suggest to be promising candidates for enhancing future clinical mapping systems.

Zusammenfassung

Die Behandlung von atrialen Rhythmusstörungen wie Vorhofflimmern ist insbesondere für Patienten mit pathologisch verändertem Substrat eine andauernde Herausforderung. Über die Pulmonalvenenisolation hinausgehende, individualisierte Ablationsstrategien werden mit Nachdruck verfolgt. Aktuelle Ansätze zur Identifikation von arrhythmogenen Regionen verlassen sich hauptsächlich auf Elektrogrammmerkmale wie Aktivierungszeiten und Amplitude oder Fraktionierung als Surrogat für die Pathologie des Gewebes. Trotz aller Bemühungen lieferten große klinische Studien unklare Ergebnisse bezüglich der Wirksamkeit verschiedener Ansätze des Substratmappings ohne signifikante Verbesserung des Behandlungsergebnisses für den Patienten.

Diese Arbeit legt den Fokus auf ein verbessertes Verständnis von Elektrogrammmerkmalen und lokalen Impedanzmessungen im Vorhof zur Extraktion von klinisch relevanten und aussagekräftigen Substratcharakteristika.

Elektrogrammmerkmale wurden mit besonderem Augenmerk auf die zugrundeliegenden Ausbreitungsmuster extrahiert, um strukturelle und funktionale Morphologieänderungen zu adressieren. Algorithmen zur Schätzung der Reduktion des Rauschlevels in unipolaren Elektrogrammen wurden implementiert und angewandt. Elektrogrammeigenschaften zeigten über viele Patienten hinweg schmale Verteilungen für gesundes Substrat, während eine breite Spannweite für pathologisch veränderte Erregungsausbreitung beobachtet wurde.

Außerdem wurde die lokale Impedanz als neuartiger Parameter und Mappingmodalität untersucht. Seit der kürzlichen Einführung in den Medizinproduktemarkt zur Überwachung der Ausbildung von Ablationsnarben wurden erste klinische Erfahrungen mit zur lokalen Impedanzmessung befähigten Kathetern gemacht. Ergänzende Studien zur Beleuchtung von unerwünschten Einflussfaktoren und der potentiellen Anwendung als Werkzeug für Substratmapping blieben bisher aus. Diese Arbeit verfolgte durch Kombination von *in human*, *in vitro* und *in silico* Experimenten einen trimodalen Ansatz, um die Auswirkung verschiedener Umgebungsbedingungen auf die lokale Impedanz zu quantifizieren und zu verstehen. Die Ausbreitung des elektrischen Feldes wurde im Computermodell mit Hilfe der Finite Elemente Methode berechnet. Durch Lösen des inversen Problems konnten im Anschluss Gewebeleitfähigkeiten rekonstruiert werden. Passende Vorverarbeitungsschritte für klinische Messungen wurden entwickelt, um Artefakte automatisch zu beseitigen. Zwei klinische Studien zur lokalen Impedanz als Indikator für die Ausbildung von Ablationsläsionen sowie zur Kartierung des Vorhofs basierend auf der lokalen Impedanz rundeten das

Forschungsprojekt ab. Lokale Impedanzmessungen identifizierten sowohl vorabladierte als auch native Narbenareale unabhängig von der Erregungsausbreitung. Eine detailgenaue Simulationsumgebung für lokale Impedanzmessungen wurde mit *in vitro* Aufnahmen validiert und lieferte quantitative Erkenntnisse über den Einfluss von Veränderungen der Umgebung im klinischen Kontext. Die inverse Rekonstruktion von relativen Gewebeleitfähigkeiten ergab vielversprechende Resultate im Computermodell.

Die Ergebnisse zeigten, dass lokales Impedanzmapping großes Potenzial zur Ergänzung von Elektrogramm-basiertem Substratmapping birgt. Eine validierte Simulationsumgebung für lokale Impedanzmessungen bietet die Möglichkeit zur vereinfachten und optimierten Entwicklung der nächsten Generation klinischer Katheter. Die Ausbreitungsgeschwindigkeit, Elektrogrammcharakteristika und rekonstruierte Gewebeleitfähigkeiten sind vielversprechende Kandidaten zur Verbesserung zukünftiger klinischer Mappingsysteme.

Acknowledgments

This work profited from the support by many associates who accompanied me on my way throughout four years of doctorate research and deserve my deepest gratitude.

My sincere gratitude goes to Prof. Dr. rer. nat. Olaf Dössel for giving me the opportunity to pursue my doctorate research at IBT: Thank you for having me be part of the amazing team you grew at IBT, for the valuable support and the research environment you provided throughout the years, and for the creative freedom you gave me. Thank you for the unique opportunity to jointly contribute to the organization of the 4th Atrial Signals Symposium at KIT and for keeping closely in touch with our favourite collaborators at Städtisches Klinikum Karlsruhe together every month.

I would also like to thank PD Dr. med. Armin Luik for countless onsite lessons in cardiac electrophysiology: You kept the doors of the electrophysiology department open for me at any time of the day. Without your trust and support from the very beginning, large parts of this thesis would not have been possible. Besides everything you taught me, you definitely infected me with your love of and dedication to cardiac electrophysiology. Without you, this work would have been nowhere near as fun, medically oriented, and — I dare to say — meaningful as it was.

I am beyond grateful for having been part of a fantastic team at IBT. Many thanks go to ...

- ... Dr.-Ing. Nicolas Pilia for being one of the most trustworthy colleagues and friends, for acrobatic recreation, scientific discussions, and countless talks on the most diverse set of topics.
- ... Dr.-Ing. Mark Nothstein and Dr.-Ing. Jorge Sánches for being loyal office mates in 413.1 who had a sympathetic ear and a helping hand for me anytime.
- ... Dr.-Ing. Michael Kircher for introducing me to the world of impedance.
- ... Carmen Martínez Antón for being my local impedance mentee and buddy.
- ... Tobias Gerach for sharing ups and downs of PhD life.
- ... Dr.-Ing. Steffen Schuler for never hesitating to help with a legendary set of skills.
- ... Dr. Tiago Almeida for bringing some Brazilian flair to Karlsruhe.
- ... Dr.-Ing. Giorgio Luongo and Dr.-Ing. Luca Azzolin for lessons on the Italian way of life.
- ... Dr.-Ing. Ady Naber for random visits to our office full of afternoon talks and juggling practice.
- ... Dr.-Ing. Andreas Wachter for lending a helping hand in IT and ice cream issues.

... Jochen Brenneisen for talks between neighbors.
... PD Dr.-Ing. Axel Loewe and Prof. Dr. rer. nat. Werner Nahm for many lively discussions and co-mentoring.
... Manfred Schroll for keeping the IT infrastructure running.
... the students who contributed to this work by means of Bachelor's and Master's theses as well as student research projects: Sophie An, Lena Heinemann, Jeanne Koch, Nick Lorenz, Claudia Nagel, Erik Oberschulte, Leonie Schicketanz, and Michael Stritt.
... all other colleagues and employees who made life at IBT fun and unique.

I would like to thank Annika Haas for being an amazing clinical point of contact: Thank you for answering any kind of question on electrophysiology and for finding practical solutions to countless complex hurdles. Many thanks go to the always receptive team at the electrophysiology lab at Städtisches Klinikum Karlsruhe for welcoming me to their territory and enduring extended study protocols with pleasure. I am grateful for extensive and dedicated support by Carina Jäger and Dr.-Ing. Tobias Oesterlein in any Rhythmia HDx enquiry. I would also like to thank Prof. Dr. med. Reza Wakili and his team at the West German Heart and Vascular Center at the University Hospital Essen for fruitful collaboration.

I am grateful for financial support by the German Research Foundation and Boston Scientific.

A sportive thank you goes to my gymnastics buddies: You always managed to get my mind off work and made me walk out of the gym with recharged batteries after practice.

I would like to thank all my friends and family, including those who are not with us anymore: You watched and followed the progress of this work with excitement and contributed to a pleasant work-life balance.

Finally, my most heartfelt thank you goes to my parents: Thank you Mama and Papa for providing the warmest home I could have ever asked for. Thank you for your unconditional love and support in any situation, for always believing in me, and for having made me the person I am today. I know you have my back whenever I need you.

Forever grateful,

Laura

Contents

Abbreviations

AFib	atrial fibrillation
AFlut	atrial flutter
CL	cycle length
CS	coronary sinus
CV	conduction velocity
EAMS	electroanatomical mapping system
ECG	electrocardiogram
EGM	electrogram
EIT	electrical impedance tomography
ERP	effective refractory period
IQR	interquartile range
LA	left atrium
LAT	local activation time
LI	local impedance
LIPV	left inferior pulmonary vein
LSPV	left superior pulmonary vein
NaCl	sodium chloride
PSD	power spectral density
PV	pulmonary vein
PVI	pulmonary vein isolation
RA	right atrium
RIPV	right inferior pulmonary vein
RSPV	right superior pulmonary vein
TMV	transmembrane voltage

Chapter 1

Introduction

1.1 Motivation

The treatment of atrial rhythm disorders such as atrial fibrillation has remained a major challenge predominantly for patients with severely remodeled substrate. Individualized ablation strategies beyond pulmonary vein isolation in combination with real-time assessment of ablation lesion formation have been striven for insistently. Current approaches for identifying arrhythmogenic regions predominantly rely on electrogram-based features such as activation time and voltage or electrogram fractionation as a surrogate for tissue pathology. Despite bending every effort, large-scale clinical trials have yielded ambiguous results on the efficacy of various substrate mapping approaches without significant improvement of patient outcomes.

The interpretation of pathological electrograms is a complex task and has to account for the interplay of underlying substrate, excitation patterns, and measurement techniques. Taking a closer look at electrogram features while keeping an eye on the underlying excitation mechanism will shed light on the risks and rewards of electrogram features as surrogates of substrate properties.

Since electrogram-based substrate mapping has been lacking the breakthrough into optimum outcomes for patients with severely remodeled substrate, local impedance as a potential novel mapping modality deserves attention. While the basic concept of local impedance-based substrate characterization seems straightforward, confounding factors have to be taken into account. Due to the novelty of the modality and the clinical focus on ablation lesion assessment rather than on mapping, local impedance lacks a series of baseline studies and considerations to elucidate risks and rewards of establishing a complementary substrate mapping modality.

1.2 Objective

This work focuses on enhancing the understanding of electrogram features and local impedance measurements in the atria towards a better understanding of *in human* measurements. The investigations conducted in the course of the work pave the way for potentially augmenting electrogram-based substrate mapping by local impedance measurements.

1.3 Structure

This work is structured in two main parts dealing with electrogram analysis and impedance measurements in the atria.

To start with Part I, electrogram features were introduced, calculated, and assessed in the presence of distinct wave propagation phenomena. Additionally, the noise level of unipolar and bipolar electrograms was calculated and lowered by advanced filtering methods. Both studies were conducted on a clinical cohort of 33 patients diagnosed with atypical atrial flutter.

Part II of this thesis deals with local impedance measurements and comprises four studies. Firstly, the morphology of local impedance drops during radio frequency ablation delivery was quantified with respect to ablation power, procedural timing, and anatomical region. The clinical study comprised 54 subjects diagnosed with atrial fibrillation.

Secondly, an *in silico* framework was built up and validated with *in vitro* experiments to conduct detailed simulations of local impedance measurements and quantitatively conclude on confounding factors. Clinically available catheters were modeled in detail and embedded into relevant surroundings.

Thirdly, a clinical study demonstrated the potential of local impedance mapping for a clinical cohort of 14 patients. Full chamber impedance maps were compiled. Previous ablation lesions as well as native scar areas were identifiable by means of local impedance.

Lastly, electrical impedance tomography was implemented for intra-atrial mapping catheters to reconstruct the relative conductivity of the underlying tissue in an *in silico* model. Both coarse and fine structures of scar tissue could be identified correctly in the reconstructed images.

PART I

FUNDAMENTALS

Chapter 2

Medical Fundamentals

2.1 Cardiac Anatomy

The human heart is composed of four chambers as depicted in the cross-section in Fig. 2.1. The right atrium (RA) collects deoxygenated blood from the systemic circulation via the superior and inferior vena cava and forwards it through the tricuspid valve to the right ventricle. The right ventricle pumps the blood through the pulmonary artery into the pulmonary circulation system towards the lungs where it is enriched with oxygen. From the lungs, the blood flows back to the left atrium (LA) via commonly four pulmonary veins (PVs), namely the left superior pulmonary vein (LSPV), left inferior pulmonary vein (LIPV), right superior pulmonary vein (RSPV), and right inferior pulmonary vein (RIPV). Via the mitral valve, the oxygenated blood enters the left ventricle which pumps the blood back into the systemic circulation system to supply cells with oxygen. All valves prevent retrograde blood flow. The wall shared by RA and LA is referred to as inter-atrial septum. Analogously, the ventricles share the inter-ventricular septum. The ventricular myocardium measures approximately one centimeter in thickness and finds the strength to pump the blood throughout the systemic and pulmonary circuit. The atrial myocardium, on the contrary, measures only few millimeters in thickness. While the inner surface of cardiac walls is referred to as endocardium, the outer surface is called epicardium. The embraced layer is called myocardium. The coronary sinus (CS) is the largest cardiac vein channeling blood from the myocardium back into the RA and is located at the posterior junction of the LA and the left ventricle. [1] [2] [3] [4]

2.2 Cardiac Electrophysiology

Cardiac myocyte contraction is provoked by electrical excitation. If the transmembrane voltage (TMV) being the potential difference between the exracellular and intracellular space exceeds a threshold potential of about $-70\,\mathrm{mV}$, a cardiac action potential is triggered and causes myocyte contraction. Electrical coupling between neighboring myocytes passes the

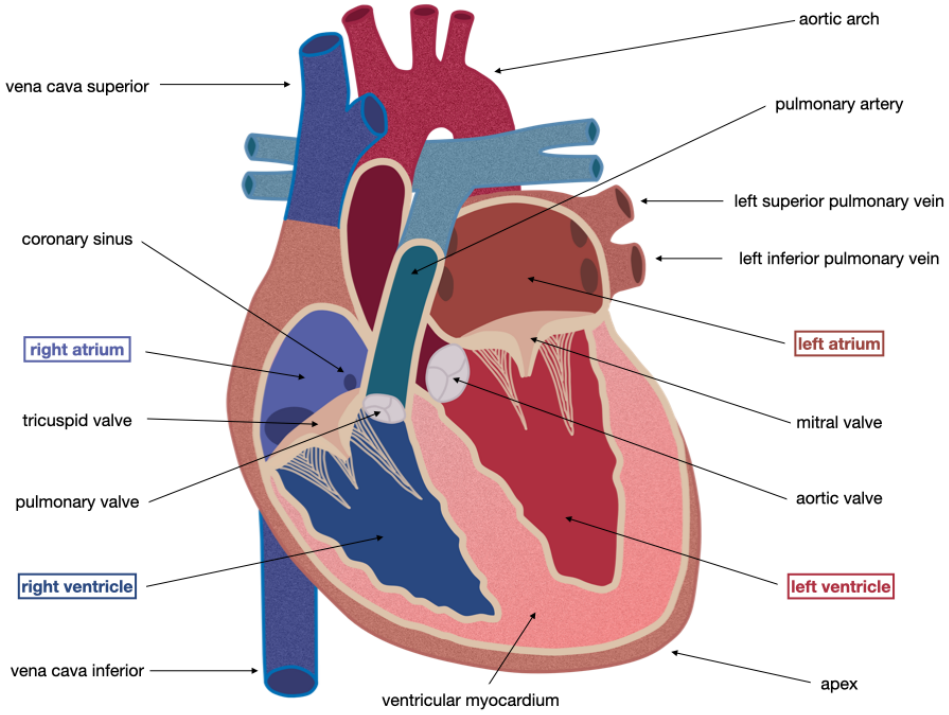

Figure 2.1: Cross-section of the human heart in anterior view. Schematic view of the left and right atrium, the left and right ventricle, the four cardiac valves, and connected great vessels. Chambers and vessels carrying oxygen-rich blood are colored in red while oxygen-deficient blood is denoted in blue.

excitation on to neighboring cells and results in an organized spread of a depolarization wavefront across the tissue. [1] [2] [3] [4]

2.2.1 Physiological Excitation Propagation

In physiological conditions, a cardiac excitation cycle starts from the electrically autorhythmic cells in the sinoatrial node located in the RA at the ostium of the superior vena cava. From the RA, the excitation wave passes on to the LA via the inter-atrial septum and Bachmann's bundle as part of the electrical conduction system. The atrio-ventricular node passes the excitation on to the ventricles with a delay. The cardiac rhythm initiated and maintained by the sinoatrial node is referred to as sinus rhythm. [1] [2] [3] [4]

2.2.2 Atrial Rhythm Disorders

Physiologically, a cardiac cell is non-responding to electrical stimuli during the effective refractory period (ERP) preventing immediate reexcitation of a cell. In pathological cases,

shortening of the refractory period in combination with a decrease in conduction velocity (CV) often enables the atria to maintain self-sustaining rhythms of increased excitation rate, so-called supraventricular tachycardia. The minimum of sustainable cycle lengths (CLs) is given by the product of ERP and CV:

$$CL_{\min} = ERP \cdot CV. \tag{2.1}$$

In the following, atrial flutter (AFlut) and atrial fibrillation (AFib) will be described in further detail.

Atrial Flutter

AFlut is a repetitive atrial tachycardia characterized by cyclic and self-sustained excitation around anatomical or structural obstacles. It is further classified as typical AFlut and atypical AFlut. For typical AFlut, the reentrant circuit is anchored to the tricuspid valve in the RA in clockwise or counter-clockwise direction. Atypical AFlut summarizes all other kinds of repetitive reentrant circuits in the RA and the LA [5] [6]. Commonly observed anatomically based forms of atypical AFlut propagate around the mitral valve or the PVs. Structural obstacles such as native scar tissue or incomplete lesions from previous atrial interventions are also prone to sustain reentrant circuits. All previously described forms of AFlut are referred to as macro-reentrant circuits. Mico-reentrant circuits and localized reentries, on the contrary, are less common forms of atypical AFlut manifesting within small areas of slower conduction [7].

The atrio-ventricular node prevents fast ventricular excitation rates by blocking high frequencies of atrial excitation. Acting as gatekeeper, the atrio-ventricular node passes on every n^{th} atrial excitation to the ventricles, which is referred to as n:1 conduction.

Atrial Fibrillation

AFib is a type of supraventricular tachycardia characterized by uncoordinated atrial electrical activation resulting in inefficient atrial contraction [8]. Focal triggers within the PVs [9] are described alongside with rotational and multi-wavelet reentrant patterns as initiating and maintaining mechanisms of AFib.

Being the most common sustained cardiac arrhythmia in adults worldwide with a prevalence of 2 % to 4 % [8][10], both patients and health care systems are significantly burdened by the lack of reliably successful therapies.

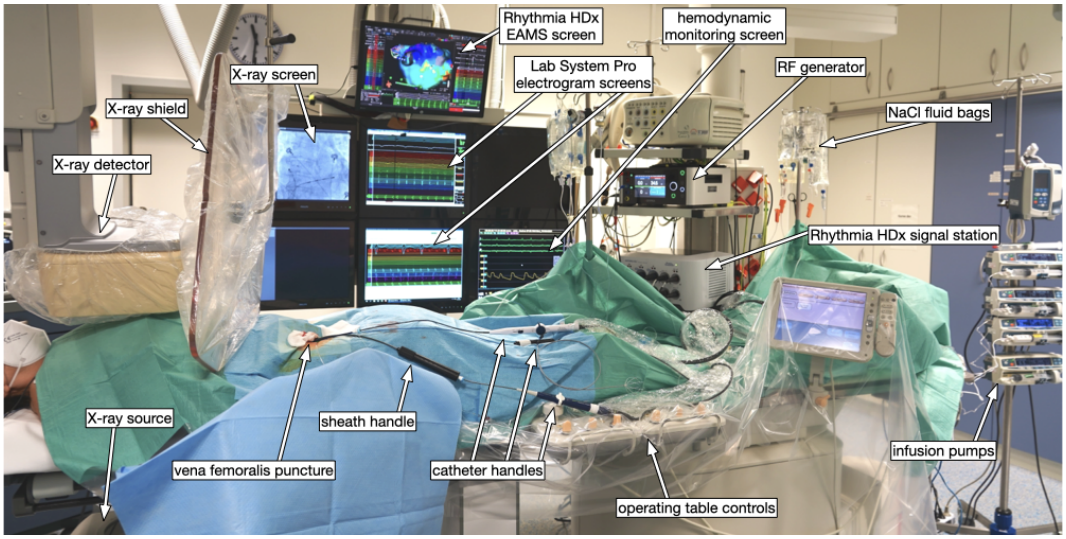

Figure 2.2: Typical setup in an electrophysiology lab. Screens behind the operating table display relevant information to the electrophysiologist.

2.2.3 Electrophysiological Study

An electrophysiological study is a minimally invasive, medical procedure to diagnose and treat heart rhythm disorders. Electrical excitation is measured with electrodes of intra-cardiac catheters. For atrial procedures, the vena femoralis is punctured at the patient's groin to introduce catheters via a sheath and forward them via the venous system to the inferior vena cava and the RA as depicted in Fig. 2.2 and Fig. 2.3. If access to the LA is needed, a transseptal needle punctures the inter-atrial septum to provide access for a mostly steerable sheath to the LA. Subsequently, a catheter can access the LA via the transseptal sheath. Optionally, a second transseptal puncture can guide a second sheath and catheter as depicted in Fig. 2.3.

A typical set of catheters for three-dimensional mapping procedures includes a mapping catheter such as the IntellaMap Orion™ or the Advisor™ HD Grid, an ablation catheter such as the IntellaNav MiFi™ OI or the IntellaNav Stablepoint™, and a CS catheter as depicted in Fig. 2.3 and Fig. 2.4. The CS catheter is typically an eight- or ten-pole linear catheter and enters the CS ostium from the RA as depicted in Fig. 2.3 to record the atrial rhythm from a fixed location. The mapping catheter typically comes with a large number of electrodes and is used to sample the atrial endocardium. The location is tracked by magnetic and/or impedance sensors to reconstruct the endocardial wall as the convex hull. Additionally, the information collected by the electrodes is projected to this endocardial shell and encoded by colors. The resulting colored atrial geometry is referred to as map and can present information on excitation propagation, electrogram amplitude, or substrate characteristics to the electrophysiologist. After determining sites of pathological excitation origin or maintenance, an ablation catheter is used to create myocardial lesions by destructive

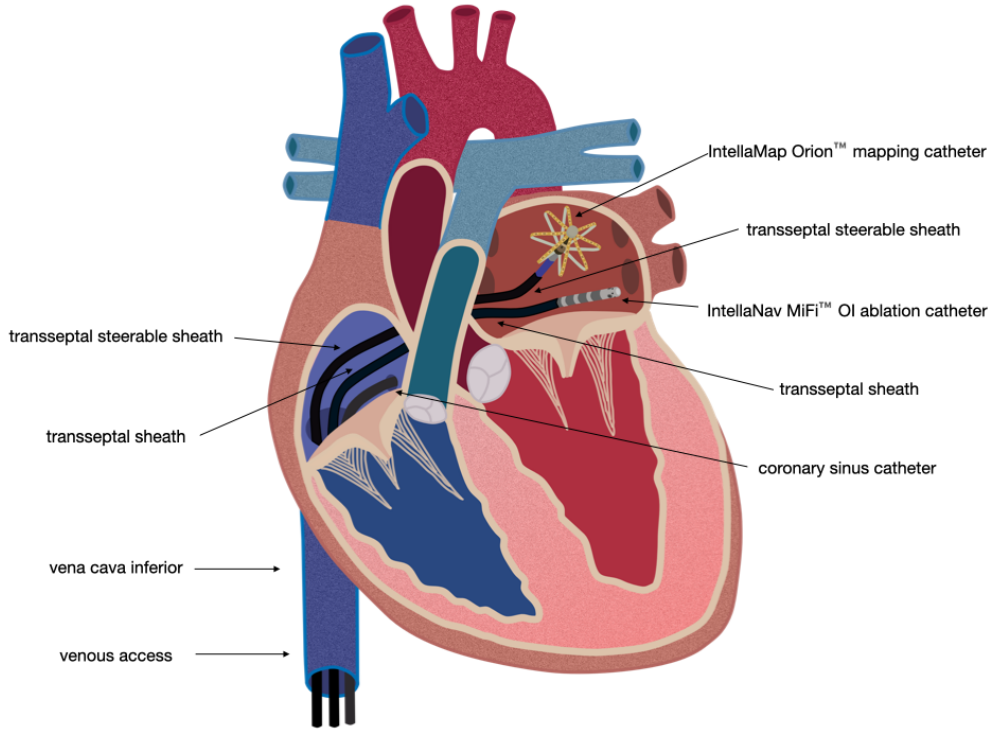

Figure 2.3: Left atrial access with a mapping and an ablation catheter via the vena cava inferior and transseptal punctures. The CS catheter is positioned in the CS.

tissue heating or cooling. Scar tissue does not conduct electrical impulses and prevents the establishment of undesired rhythms after the intervention.

Fig. 2.4 depicts two radio frequency ablation catheters in (a) and (b), a transseptal steerable sheath in (c), and two high-density mapping catheters in (d) and (e). The transseptal sheath is typically flushed with sodium chloride (NaCl) solution from irrigation fluid bags to prevent retrograde blood flow into the sheath, air embolism, and clotting. If equipped with a cooling system, an irrigation pump supplies NaCl solution to the ablation catheter as well.

Fig. 2.2 shows a typical setup of an electrophysiology lab equipped with an X-ray system, a 3D electroanatomical mapping system (EAMS), an electrogram recording system, a hemodynamic monitoring system, irrigation fluid bags and irrigation pump, infusion pumps, and the patient table. The operator maneuvers sheaths and catheters with their respective handles proximal to the puncture of the vena femoralis.

2.2.3.1 Intra-Atrial Electrograms

The electrical signal measured with electrodes on intra-atrial catheters is called intra-atrial electrogram (EGM). With the unipolar and the bipolar electrogram, two fundamentally different types of EGMs are differentiated. While the unipolar EGM is defined as the

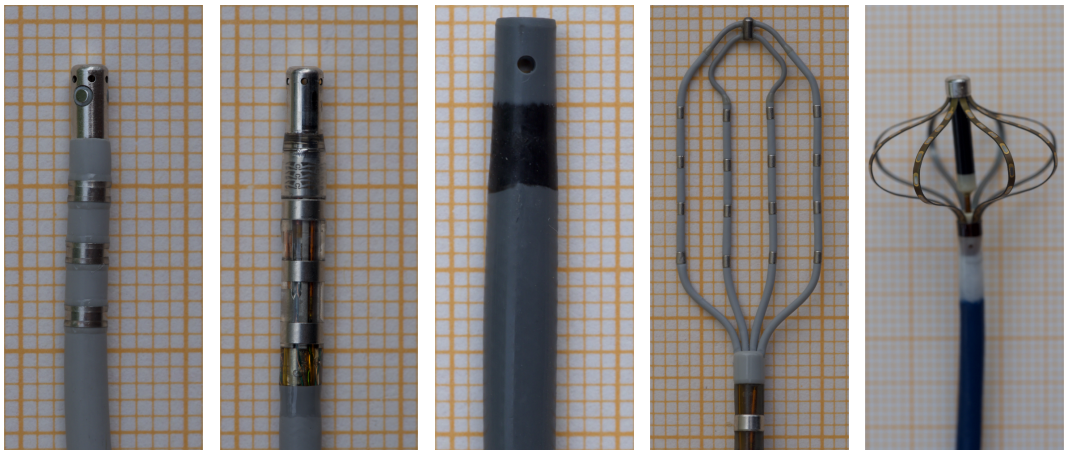

Figure 2.4: Photographs of various catheters and a transseptal sheath: (a) IntellaNav MiFi™ OI, (b) IntellaNav Stablepoint™, (c) Agilis NxT™ transseptal sheath, (d) Advisor™ HD Grid, (e) IntellaMap Orion™. Square grid of 1 mm edge length in the background.

potential difference between an intra-cardiac electrode and an approximation of the electrical ground potential, the bipolar EGM is calculated by subtraction of two adjacently recorded unipolar EGMs.

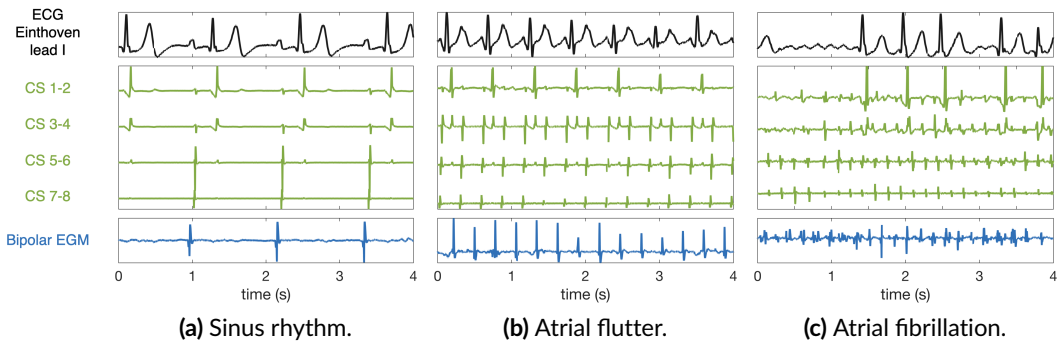

(a) Sinus rhythm. **(b)** Atrial flutter. **(c)** Atrial fibrillation.

Figure 2.5: Local bipolar EGMs, bipolar CS EGMs, and surface electrocardiograms (ECGs) during sinus rhythm (a), AFlut (b), and AFib (c).

Fig. 2.5 shows exemplary sets of intra-atrial EGMs and the corresponding surface electrocardiograms (ECGs) for sinus rhythm, AFlut, and AFib. During sinus rhythm, the CS is activated from the proximal to the distal electrodes with approximately one atrial and one subsequent ventricular activation per second as displayed in Fig. 2.5 (a). Fig. 2.5 (b) shows EGM traces recorded during AFlut with 2:1 atrio-ventricular conduction. The proximal to distal CS sequence and the local signal morphology are repetitive with each atrial beat. During AFib, the CS sequence as well as the local EGM morphology vary throughout all

channels with each excitation as displayed in Fig. 2.5 (c). Highly variable RR-intervals in the surface ECG are a typical indicator for ongoing AFib.

2.2.3.2 Local Activation Time and Voltage Mapping

For repetitive atrial rhythms, local activation time (LAT) mapping is a standard approach to comprehend excitation propagation. The LAT is typically calculated from the intra-atrial EGM as the time of steepest negative slope or maximum absolute amplitude. Projecting the LAT to the atrial endocardium visualizes the progressive propagation of an excitation wavefront across the atria. LAT maps can be compiled from both unipolar and bipolar EGMs. Fig. 2.6 depicts exemplary bipolar LAT maps recorded with the Rhythmia HDx EAMS in the respective left panels.

Equally established as LAT maps, voltage maps provide information on peak-to-peak EGM amplitude throughout the atria and allow to delineate scars and pathologically low EGM amplitudes. Voltage maps can be compiled both from unipolar and bipolar EGMs. Fig. 2.6 depicts exemplary bipolar voltage maps recorded with the Rhythmia HDx EAMS in the respective right panels.

2.2.3.3 Pulmonary Vein Isolation

Based on the insight that the PVs are prone to host focal triggers of AFib [9], pulmonary vein isolation (PVI) has become the first-line ablative approach for AFib treatment [8]. Point-by-point radio frequency energy is delivered to circumferentially isolate the PVs by ipsilateral circles. Alternatively, cryo balloons have emerged as single-shot devices to freeze and thus isolate vein by vein yielding outcomes comparable to radio frequency ablation [11] [12].

2.2.3.4 Local Impedance

The DirectSense™ technology [13] as a module of the Rhythmia HDx EAMS allows to assess radio frequency ablation delivery in real-time by measuring the change in local impedance (LI). Injecting an alternating current at a frequency of 14.5 kHz via two intra-cardiac electrodes creates a potential field that is altered depending on the conductive properties of the surroundings. Measuring the potential difference between two sample points, namely two intra-cardiac electrodes, gives insight into the underlying formation of the electrical field and the conductive properties of the surroundings. The so-called LI is calculated as the quotient of the measured potential difference $\Delta\hat{\Phi}$ and the injected current amplitude $\hat{I}$ and carries the physical unit Ω.

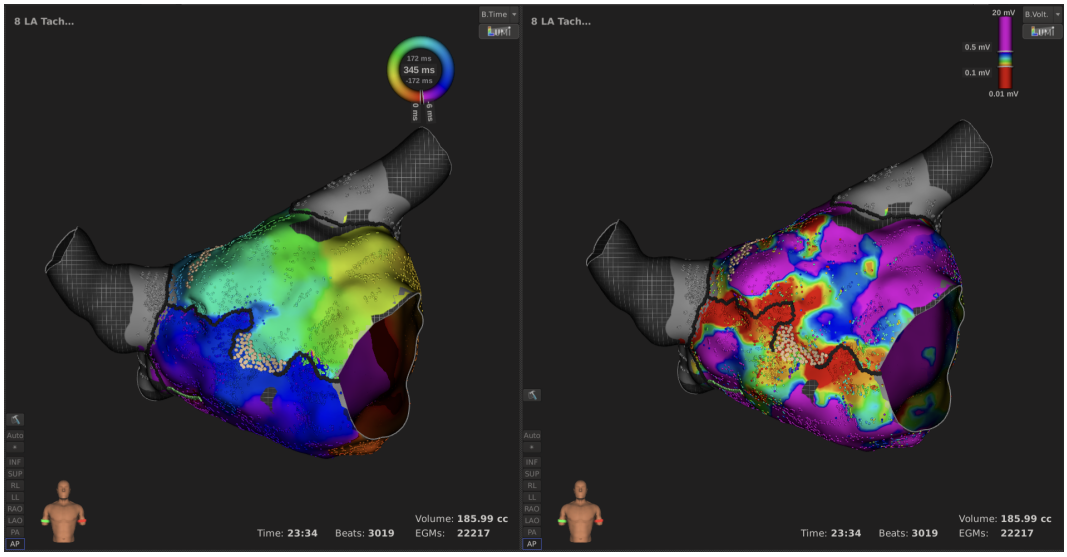

(a) LAT and voltage map in anterior-posterior perspective.

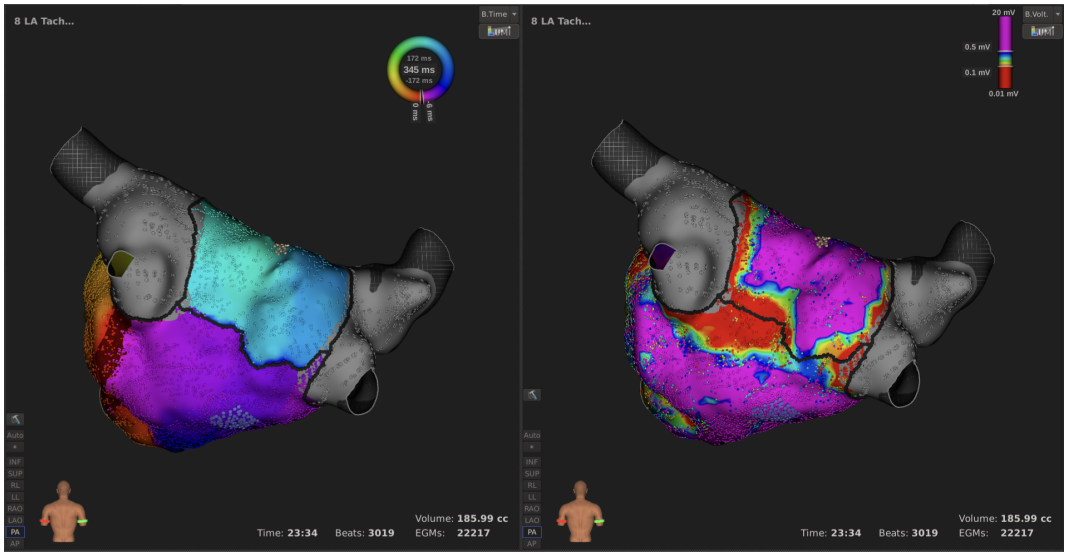

(b) LAT and voltage map in posterior-anterior perspective.

Figure 2.6: LAT and voltage maps during AFlut in the left and right panel, respectively, in anterior-posterior (a) and posterior-anterior (b) perspective recorded with the Rhythmia HDx EAMS. The excitation propagates counter-clockwise around the mitral valve passing through a gap in an anterior line with a CL of 345 ms. An intact roof line blocks excitation. All PVs are isolated. Lines of block are denoted by black dots. Orange dots in the gap of the anterior line denote slow conduction. The roof line and the anterior line are characterized by areas of low voltage.

The IntellaNav MiFi™ OI hosts a four-terminal circuit injecting an alternating current from the distal tip electrode to the proximal ring electrode. The voltage is measured between the distal ring electrode and each of the three mini electrodes. Reducing the three measurements to their maximum before LI calculation aims at picking the measurement in closest proximity to the tissue. The IntellaNav Stablepoint™ hosts a three-terminal circuit with the injecting

and measuring circuit sharing one of the electrodes. Current injection between the distal tip electrode and the proximal ring electrode is paired with voltage measurement between the distal tip electrode and the distal ring electrode. Fig. 2.7 schematically depicts the injection and measurement circuits for either catheter.

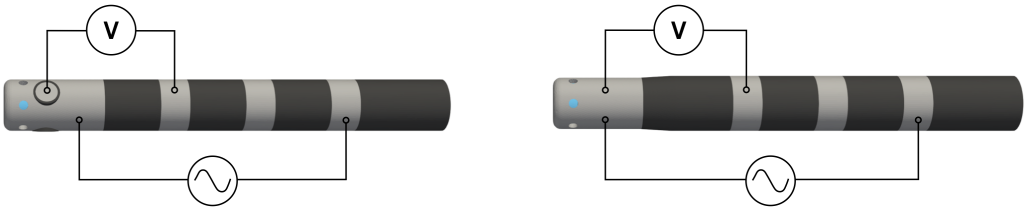

(a) Four-terminal DirectSense™ circuit in the IntellaNav MiFi™ OI.

(b) Three-terminal DirectSense™ circuit in the IntellaNav Stablepoint™.

Figure 2.7: DirectSense™ circuits in the IntellaNav MiFi™ OI (a) and the IntellaNav Stablepoint™ (b). Alternating current injection and voltage measurement in a three- and four-terminal circuit.

Chapter 3

Technical Fundamentals

3.1 Electrical Conductivity and Permittivity

The conductivity σ and the complex permittivity ε describe the characteristic response of a material to an applied electrical field $\boldsymbol{E}$. While σ and ε are tensors for anisotropic materials, they both reduce to constants for the simpler case of isotropic materials as assumed in the following. The conductivity σ characterizes the material's ability to conduct electrical charges and is typically measured in $\frac{\mathrm{S}}{\mathrm{m}}$ whereas the complex permittivity ε quantifies the polarizability and thus the ability to store electrical charges and carries the unit $\frac{\mathrm{F}}{\mathrm{m}}$ [14]. Typically, the permittivity of a linear material is given as the relative permittivity ε_r with

$$\varepsilon = \varepsilon_0 \cdot \varepsilon_\mathrm{r} \tag{3.1}$$

and ε_0 being the permittivity of free space. The relative permittivity connects the electrical field $\boldsymbol{E}$ to the electrical displacement field $\boldsymbol{D}$ as

$$\boldsymbol{D} = \varepsilon_0 \varepsilon_\mathrm{r} \boldsymbol{E} \tag{3.2}$$

and consists of a real part ε' and an imaginary part ε'' [15]

$$\varepsilon_\mathrm{r} = \varepsilon' - \mathrm{j}\varepsilon'' \tag{3.3}$$

with j being the unit imaginary number.

3.1.1 Conductivity of Aqueous Solutions

An aqueous solution is a solution composed of deionized water acting as solvent in which any kind of solute is dissolved. The solute may be composed of one or more solids, fluids, or

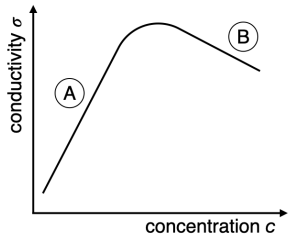

Figure 3.1: Conductivity σ of aqueous electrolyte solutions by electrolyte concentration c. A linear increase for low concentrations is followed by a decrease for high concentrations. Inspired by [16].

gases. In this work, particular attention is drawn to aqueous electrolyte solutions, specifically aqueous sodium chloride (NaCl) solutions.

Solutions are further specified by the concentration of the solute i in the solvent. The molar concentration c_i, also referred to as molarity, is defined as the quotient of the amount of substance n_i and the total volume of the solution V [16]:

$$c_i = \frac{n_i}{V} \tag{3.4}$$

and carries the unit $\frac{\text{mol}}{\text{m}^3}$ or more commonly $\frac{\text{mol}}{\text{l}}$. Alternatively, solutions are often characterized by the mass fraction w_i being defined as the quotient of the mass of the solute m_i and the total mass of the solution m [16]:

$$w_i = \frac{m_i}{m}. \tag{3.5}$$

The molecular weight M_i relates the mass m_i with the amount of substance n_i as [16]:

$$n_i = \frac{m_i}{M_i}. \tag{3.6}$$

Given the molecular weight of a solute i and the solvent as well as the respective densities ρ, mass fraction and molar concentration can be converted into each other.

The molecular weight of NaCl as the electrolyte in focus is given as $M_{\text{NaCl}} = 58.44\,\frac{\text{g}}{\text{mol}}$ [17].

Fig. 3.1 depicts the schematic dependency of the conductivity σ on the concentration c of aqueous electrolyte solutions. For low concentrations (label A in Fig. 3.1), the conductivity increases linearly with the concentration. For high concentrations (label B in Fig. 3.1), the trend reverses with decreasing conductivity for increasing concentration. The initial linear increase results from an increase in the number of available ions for current conduction. The decrease in conductivity for high electrolyte concentrations goes back to three effects [16]:

- the formation of ion clouds, i.e. the accumulation of ions of opposite charge around a central ion, shields the carriers of charge resulting in the availability of less ions for the transport of electrical current.

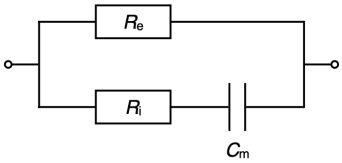

Figure 3.2: Equivalent circuit of biological tissue as proposed by Cole and Cole [20]. The extracellular medium is modeled by an extracellular resistance R_e. Cells are represented by a serial combination of intracellular resistance R_i and membrane capacitance C_m

- ion clouds are more inert than free ions resulting in inhibition of the transport of electrical current.
- in case of weak electrolytes, the degree of dissociation decreases for increasing concentrations resulting in the availability of less ions for the transport of electrical current.

All *in vitro* experiments in this work were conducted at concentrations with linearly increasing conductivity per increase in concentration (label A in Fig. 3.1).

Besides the concentration, temperature is a major determinant of an electrolyte solution's conductivity. Higher temperature increases ion mobility and thus the conductivity of the solution.

The frequency of the applied electrical field also has an influence on the conductivity of the solution as described by the Debye-Falkenhagen effect. Setting in at very high frequencies in the mid MHz range only [17] [18] [19], all considerations in this work assumed the Debye-Falkenhagen effect to be negligible for aqueous NaCl solutions with the frequency range of interest being in the kHz range.

3.1.2 Dielectric Properties of Biological Tissue

Biological tissues and fluids are mainly composed of extracellular fluid and cells causing a strong frequency dependency of the dielectric properties. Current can essentially take two different paths through biological tissue passing either through the extracellular space or through the cells. As proposed by Cole and Cole [20], an equivalent circuit as displayed in Fig. 3.2 can be set up by combining the extracellular impedance and the cellular impedance in parallel. The extracellular impedance is purely resistive modeled by a resistor R_e while the cellular impedance is represented by the serial combination of the intracellular resistance R_i and the capacitance of the cell membrane C_m.

The progressive increase of tissue conductivity with frequency is mostly attributed to Maxwell-Wagner [21] [22] effects, i.e. interfacial ionic polarization at the cell membranes [23]. For direct currents and low frequencies, cells are poorly conductive and the current path is restricted to the extracellular medium. For higher frequencies, cells become accessible to

the applied current due to capacitive properties of the cell membrane and cause an increase in conductivity [23] by opening up the intracellular current path. The resulting change in conductivity and permittivity is referred to as β-dispersion and occurs in the frequency range between 1 kHz and several MHz [15] [24].

3.2 Linear Regression

Linear regression models the dependency of N observations $\boldsymbol{y} = [y_1, y_2, \ldots, y_N]^\top$ on a set of inputs $\boldsymbol{X} = [\boldsymbol{x_1}, \boldsymbol{x_2}, \ldots, \boldsymbol{x_M}]$. Each input feature $\boldsymbol{x}_i, i \in \{1 \ldots M\}$ comprises N samples $\boldsymbol{x}_i = [x_{1i}, x_{2i}, \ldots x_{Ni}]^\top$. Assuming a linear relationship with a measurement error $\boldsymbol{\varepsilon}$, the data set can be modeled as

$$\boldsymbol{y} = \widetilde{\boldsymbol{X}} \cdot \boldsymbol{\alpha} + \varepsilon \qquad \text{with} \quad \widetilde{\boldsymbol{X}} = \begin{bmatrix} x_{11} & x_{12} & \ldots & x_{1M} & 1 \\ x_{21} & x_{22} & \ldots & x_{2M} & 1 \\ \vdots & \vdots & \ddots & \vdots & 1 \\ x_{N1} & x_{N2} & \ldots & x_{NM} & 1 \end{bmatrix}, \quad \boldsymbol{\alpha} = \begin{bmatrix} \alpha_0 \\ \alpha_1 \\ \vdots \\ \alpha_M \end{bmatrix}. \tag{3.7}$$

Minimizing the squared deviation of the observed from the predicted value yields a least square estimate of the $M+1$ coefficients

$$\hat{\boldsymbol{\alpha}} = \arg\min_{\boldsymbol{\alpha}} \left\| \widetilde{\boldsymbol{X}} \boldsymbol{\alpha} - \boldsymbol{y} \right\|_2^2. \tag{3.8}$$

Left multiplying the Moore-Penrose pseudoinverse in Eq. 3.7 yields the solution

$$\hat{\boldsymbol{\alpha}} = \left(\widetilde{\boldsymbol{X}}^\top \widetilde{\boldsymbol{X}} \right)^{-1} \widetilde{\boldsymbol{X}}^\top \boldsymbol{y}. \tag{3.9}$$

3.2.1 Coefficient of Determination

The coefficient of determination R^2 is a measure for the proportion of observed variance in $\boldsymbol{y}$ that is explainable by a linear relationship between $\boldsymbol{x}$ and $\boldsymbol{y}$ and is defined as the quotient of the sum of squared errors and variance:

$$R^2 = 1 - \frac{\sum_{i=1}^{N} (y_i - \hat{y}_i)^2}{\sum_{i=1}^{N} (y_i - \bar{y})^2} \tag{3.10}$$

with y_i being the i^{th} observed sample, $\hat{y}_i$ the value predicted by the linear model, and $\bar{y}$ being the mean of all observations $\boldsymbol{y}$. $R^2 = 0$ if the linear model cannot account for the variance in the observed data. $R^2 = 1$ if the linear model completely covers the variance in $\boldsymbol{y}$.

The adjusted coefficient of determination $\bar{R}^2$ eliminates the dependency of R^2 on the number of input features M:

$$\bar{R}^2 = 1 - \left(1 - R^2\right) \frac{N-1}{N-M-1}. \tag{3.11}$$

3.2.2 Regularization

Solving Eq. 3.9 becomes numerically challenging if $\widetilde{\boldsymbol{X}}^\top \widetilde{\boldsymbol{X}}$ is ill-conditioned. A regularization term enforcing prior knowledge to the solution helps to solve the system of equations. Adding a regularization term to Eq. 3.8 yields the following for minimization

$$\left\| \widetilde{\boldsymbol{X}} \boldsymbol{\alpha} - \boldsymbol{y} \right\|_2^2 + \lambda \left\| \boldsymbol{\Gamma} \boldsymbol{\alpha} \right\|_2^2 \tag{3.12}$$

with λ being the regularization parameter and $\boldsymbol{\Gamma}$ the regularization matrix. The regularization parameter λ balances minimization of the regularization term and minimization of the squared residual norm. The regularization matrix $\boldsymbol{\Gamma}$ defines the prior knowledge imposed on the solution. Choosing $\boldsymbol{\Gamma}$ to be the identity matrix is referred to as zero-order Tikhonov [25] regularization and minimizes the norm of the solution itself. Choosing $\boldsymbol{\Gamma}$ to be a Laplacian is referred to as second-order Tikhonov or Laplace regularization [25] and minimizes the second-order derivative of the solution. The least-square solution for the model coefficients $\boldsymbol{\alpha}$ is given by

$$\hat{\boldsymbol{\alpha}} = \left(\widetilde{\boldsymbol{X}}^\top \widetilde{\boldsymbol{X}} + \lambda \boldsymbol{\Gamma}^\top \boldsymbol{\Gamma} \right)^{-1} \widetilde{\boldsymbol{X}}^\top \boldsymbol{y}. \tag{3.13}$$

3.3 Electrical Impedance Tomography

Electrical impedance tomography (EIT) is a medical imaging modality to reconstruct the spatial distribution of dielectric properties in a subject of interest. Most popularly, EIT finds application in monitoring the ventilatory state of the lungs non-invasively by means of a chest belt. An alternating current at a frequency typically below 1 MHz is injected via a pair of electrodes while another pair of electrodes measures a sample potential difference of the potential field Φ imposed by the injected current. If measurement and injection electrodes are distinct electrode pairs, the circuit is referred to as a four-terminal circuit. Four-terminal circuits have the advantage that the contact impedance between electrode and subject does not take influence on the measurement. Propagating through a multitude of injecting and measuring pairs of electrodes builds up a picture of the dielectric properties of the medium that can be reconstructed with mathematical methods [26].

3.3.1 Forward Problem of Electrical Impedance Tomography

Calculating the potential field Φ for a given distribution of dielectric properties and known stimulation currents I is denoted the forward problem of EIT. The governing equation of EIT's forward problem can be derived from Maxwell's and Poisson's equation [26] [27]. To start with, the injected current causes an electrical field $\boldsymbol{E}(\boldsymbol{p})$ at positions $\boldsymbol{p}$ and a current density $\boldsymbol{J}(\boldsymbol{p})$ that are linked via the electrical conductivity $\sigma(\boldsymbol{p})$ and the permittivity $\varepsilon(\boldsymbol{p})$:

$$\boldsymbol{J}(\boldsymbol{p}) = (\sigma(\boldsymbol{p}) + \mathrm{j}\omega\varepsilon(\boldsymbol{p})) \cdot \boldsymbol{E}(\boldsymbol{p}) \tag{3.14}$$

Since there are no internal current sources in the frequency range of interest, the divergence of the current density is known to be zero [26]:

$$\nabla \cdot \boldsymbol{J}(\boldsymbol{p}) = 0 \tag{3.15}$$

Since magnetically induced currents are relatively small for frequencies below 1 MHz, the electrostatic case can be assumed allowing to neglect the temporal derivative of the magnetic field and to express the electrical field solely as the spatial gradient of the scalar potentials $\Phi(\boldsymbol{p})$ [26]:

$$\boldsymbol{E}(\boldsymbol{p}) = -\nabla\Phi(\boldsymbol{p}) \tag{3.16}$$

Combining Eq. 3.14, Eq. 3.15, and Eq. 3.16 results in the following Laplace equation:

$$\nabla \cdot [(\sigma(\boldsymbol{p}) + \mathrm{j}\omega\varepsilon(\boldsymbol{p})) \cdot \nabla\Phi(\boldsymbol{p})] = 0 \tag{3.17}$$

For typical EIT applications in the medical field, the complex component of the admittance is relatively small compared to the real component allowing for simplification of Eq. 3.17:

$$\nabla \cdot [\sigma(\boldsymbol{p}) \cdot \nabla\Phi(\boldsymbol{p})] = 0 \tag{3.18}$$

Current injection I provides the boundary condition for the current density $\boldsymbol{J}(\boldsymbol{p})$ at the location of the electrodes. Numerically solving Eq. 3.18 by means of the finite element method while accounting for the boundary conditions on the current density $\boldsymbol{J}(\boldsymbol{p})$ yields the scalar potential field $\Phi(\boldsymbol{p})$ [26].

In order to reduce the sensitivity to modeling errors, EIT in the medical field does not typically operate on absolute conductivities $\sigma(\boldsymbol{p})$ rather than on conductivity differences $\Delta\sigma(\boldsymbol{p})$. Two measurements with different conductivity distributions $\sigma(\boldsymbol{p})$ and $\sigma_B(\boldsymbol{p})$ can be provoked in practice by taking two measurements at different frequencies or by creating

two different conductivity distributions at two different points in time. The former is referred to as frequency-difference EIT while the latter is called time-difference EIT. One of the measurements is typically referred to as background with the underlying background conductivities $\sigma_B(\boldsymbol{p})$ and potential field $\Phi_B(\boldsymbol{p})$ [26].

Let $\boldsymbol{v} = [v_1, v_2, \ldots, v_M]$ be the measurement of M potential differences at M pairs of electrodes. Then a discrete forward operator $\mathscr{F}$ can be defined which maps the conductivity distribution $\sigma(\boldsymbol{p})$ and the current injection I to measured voltages $\boldsymbol{v}$.

Taylor expansion of $\mathscr{F}$ and considering only the first order term can significantly reduce the sensitivity to modeling errors and enhances the quality of the forward calculation [28]. The first order linear Taylor approximation of $\mathscr{F}$ is called Jacobian matrix $\mathscr{J}$:

$$\Delta v = \mathscr{J}\,\Delta\sigma(\boldsymbol{p}) \tag{3.19}$$

with $\Delta\boldsymbol{v} = \boldsymbol{v} - \boldsymbol{v_B}$ being the change in voltage with respect to the background measurement. $\mathscr{J}$ is of dimension $M \times K$ with M being the number of voltage measurements and K being the number of discrete positions $\boldsymbol{p}$, i.e. the number of elements in the geometrical model [26].

3.3.2 Inverse Problem of Electrical Impedance Tomography

In typical medical settings, the distribution of conductivities $\sigma(\boldsymbol{p})$ is the unknown to be determined. The given current injection I still provides the boundary condition. The scalar potential field $\Phi(\boldsymbol{p})$ can be sampled by measuring the potential difference between pairs of electrodes to then solve the inverse problem to reconstruct $\Delta\sigma(\boldsymbol{p})$:

$$\Delta\sigma(\boldsymbol{p}) = \mathscr{J}^{-1} \cdot \Delta\boldsymbol{v}. \tag{3.20}$$

An estimate of $\Delta\sigma(\boldsymbol{p})$ can be obtained by least-square minimization:

$$\Delta\hat{\sigma}(\boldsymbol{p}) = \underset{\Delta\sigma(\boldsymbol{p})}{\arg\min} \|\Delta\boldsymbol{v} - \mathscr{J} \cdot \Delta\sigma(\boldsymbol{p})\|_2^2. \tag{3.21}$$

Eq. 3.20 can be solved with the help of the Moore-Penrose pseudoinverse as described in Eq. 3.9. Typically a regularization term as described in Eq. 3.12 is needed.

PART II

ATRIAL ELECTROGRAM ANALYSIS

Chapter 4

Spatial Evolution of Electrogram Characteristics in Vicinity of Distinct Wave Propagation Phenomena[1]

4.1 Introduction

High-density electroanatomical mapping systems have revolutionized differential diagnosis of atypical left atrial flutter (AFlut) during electrophysiological studies within the past years. Multi-electrode catheters such as the IntellaMap Orion™ come with a large number of electrodes. In combination with an automatized ultra-high density mapping system such as Rhythmia HDx (Boston Scientific, Malborough, MA, USA), more than 10 000 electrograms (EGMs) can be acquired in less than 20 minutes. The detailed understanding of AFlut mechanisms deduced from abundant information has led to high success rates [7][29][30][31][32]. Acute arrhythmia termination is typically seen as the endpoint of clinical studies. However, acute termination of AFlut does not necessarily guarantee long-term success if secondary pathological areas that are not involved in the current tachycardia provoke and maintain secondary AFlut mechanisms. A diagnosis purely based on local activation time (LAT) mapping of the current AFlut mechanism should therefore be enhanced by EGM feature analysis that can potentially unravel silent areas of arrhythmogenic substrate. Since electrophysiologists cannot manually analyze each single EGM out of thousands, automatic feature extraction is a useful tool to attract attention to potentially arrhythmogenic areas.

[1]The project presented in the course of Chapter 4 was financially supported by and conducted in collaboration with Boston Scientific (Malborough, MA, USA).

4.2 Methods

4.2.1 Study Cohort

This study was conducted on a subset of the TrueHD database provided by Boston Scientific (Malborough, MA, USA). Any patient presenting in atrial tachycardia with one out of the following three unique driving mechanisms was included in the study:

- focal source
- macro-reentry with slow conducting isthmus
- micro-reentry.

The preliminary selection of cases on the basis of available metadata was manually reviewed by electrophysiologically trained individuals for matches with the above-mentioned inclusion criteria. Reasons for exclusion were:

- poor mapping quality
- non-unique driving mechanism
- mismatch of study cohort definition (e.g. macro-reentry without clear slow conducting isthmus).

The final study cohort consisted of 33 TrueHD cases recorded at 17 electrophysiology labs worldwide including 9 cases of focal atrial tachycardia, 5 cases of atrial micro-reentry, and 19 cases of atrial macro-reentry with slow conducting isthmus.

4.2.2 Preprocessing

With the help of a Rhythmia HDx workstation, each of the 33 cases was carefully annotated by an electrophysiological expert. The annotation included:

- a single tag at focal sources
- line of tags at each micro-reentrant channel
- a single tag at the entry of each micro-reentrant channel
- a single tag at the exit of each micro-reentrant channel
- line of tags at each slow conducting isthmus
- line of tags at each wavefront collision
- line of tags at each line of conduction block
- point cloud of tags covering an area of reference tissue.

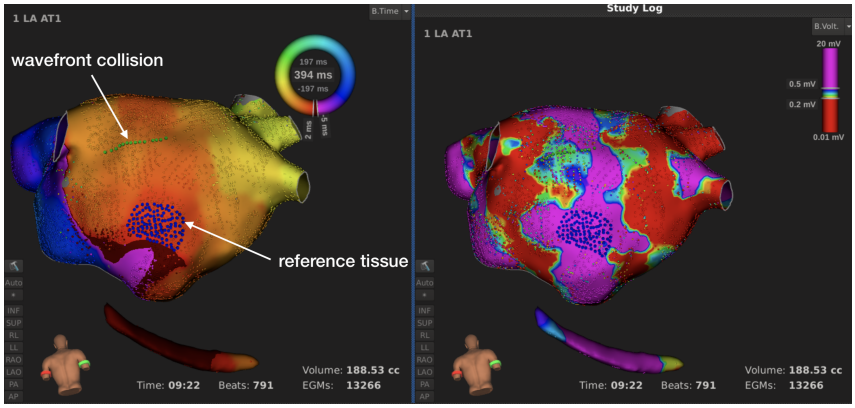

(a) Posterior view of the left atrium (LA).

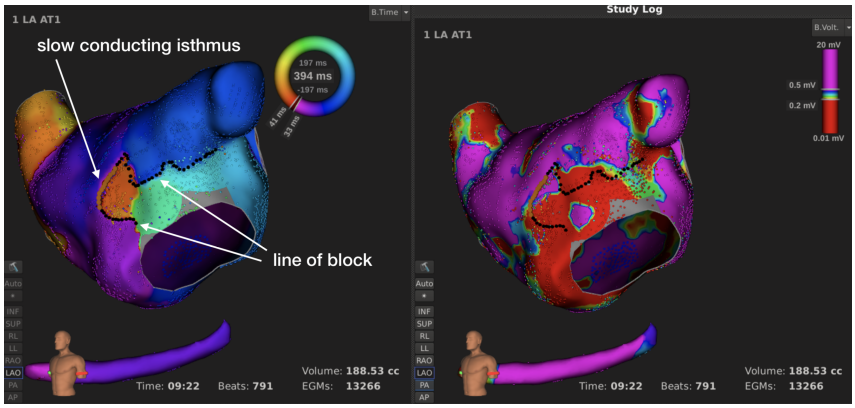

(b) Left anterior oblique view of the left atrium (LA).

Figure 4.1: Rhythmia HDx screenshots showing an exemplary case with annotations from posterior (a) and left anterior oblique (b) perspective. LAT maps are shown in the left panels. Bipolar voltage maps are depicted in the right panels. Black tags mark lines of block, green tags a wavefront collision, orange tags a zone of slow conduction, and blue tags a slab of reference tissue.

Reference tissue was required to exhibit bipolar voltage amplitudes larger than 0.5 mV and needed to be passed by a planar wavefront with high conduction velocity. Additionally, reference tissue was required to be located in a reasonable distance to any kind of irregular conduction phenomenon.

Lines and point clouds of tags were set with a tag density adjusted to the individual EGM density.

Fig. 4.1 shows annotations for an exemplary case. The map was recorded during a mitral valve dependant macro-reentrant atypical left AFlut. A planar wavefront passes the slab of reference tissue at the posterior wall from inferior to superior. A gap in an anterior line of block forms the slow conducting isthmus of the reentrant circuit.

Each acquired EGM came with the three-dimensional spatial coordinates of its acquisition site. The Euklidean distance from each annotation tag to each site of EGM acquisition was calculated. The distance of each acquisition site to the closest tag of one kind was

considered the distance of the EGM to the respective phenomenon. For the analysis of the spatial evolution of EGM features in the vicinity of a phenomenon of interest, EGMs from within 20 layers of 1 mm width around the corresponding tags were considered. EGMs from within the first layer were thus located in distances from 0 mm to 1 mm to the respectively closest tag of interest. The last layer contained EGMs with a distance of 19 mm to 20 mm to the closest tag of interest.

Given the EGMs of interest, a segment of 2 s duration was centered at the corresponding LAT provided by Rhythmia HDx. The segment was extracted from the datastream including the unipolar and bipolar LAT, the beginning and the end of the atrial cycle as used during the mapping process and the site of acquisition.

In a next step, active segments were labeled by thresholding the non linear energy operator [33] signal. The central active segment, i.e. the active segment overlapping with the extracted LAT, was considered the active segment corresponding to the respective acquisition. Additionally, QRS complexes were identified in lead I of the surface ECG [34]. If an active segment overlapped with a QRS complex, the active segment was excluded from further analysis.

For each of the valid, central active segments, features were computed as described in the following.

4.2.3 EGM Features

The following features were computed for each of the valid active segments. Some of the features considered the active segment only, whereas others also took into account a surrounding window covering the atrial cycle as exported from Rhythmia HDx.

Activity Duration

The activity duration was calculated as duration of the active segment.

Zero Crossing Rate

The number of zero crossings within the active segment was normalized by the duration of the active segment yielding the number of zero crossings per time unit.

Spectral Centroid

The center of mass of the power spectral density (PSD) of a signal is considered its spectral centroid. The spectral centroid was thus computed by weighting each frequency with the

corresponding amplitude in the PSD and subsequent division by the sum of the amplitudes.

$$SC = \frac{\sum_{n=1}^{N} f(n) \cdot PSD(n)}{\sum_{n=1}^{N} PSD(n)} \quad , \tag{4.1}$$

with SC being the spectral centroid, N being the number of samples in frequency domain, and f being the vector of frequencies. The extended segment covering the current atrial cycle was used for the calculation of the spectral centroid.

f 90 Frequency

The f 90 frequency is defined as the frequency in the PSD with 90 % of the power being located at frequencies lower than f 90. The extended segment covering the current atrial cycle was used for the calculation of the f 90 frequency.

Sample Entropy

The sample entropy quantifies the amount of information contained in a signal of length n by searching for repetitive patterns in the signal considering windows of length $m = 2$ and windows of $m_2 = m + 1$:

$$S_{\text{sample}}(m, r) = -\log \frac{A(m, r)}{B(m, r)} \quad ,$$

with A being the number of pairs of windows of length m_2 that are considered similar in terms of a distance lower than the threshold r. B, on the other hand, is the number of pairs of windows of length m that are considered similar. The threshold r was set at the 0.2-fold of the standard deviation of the analyzed segment. The extended segment covering the current atrial cycle was used for the calculation of the sample entropy [35].

Shannon Entropy

The Shannon entropy is another measure to quantify the information content of a signal and is calculated as

$$S_{\text{Shannon}} = -\sum_{i} p_i \cdot \log_2 p_i \quad , \tag{4.2}$$

with p_i being the probability of the occurrence of amplitude i in the active segment. Amplitudes were discretized into 20 bins. The extended segment covering the current atrial cycle was used for the calculation of the Shannon entropy [36].

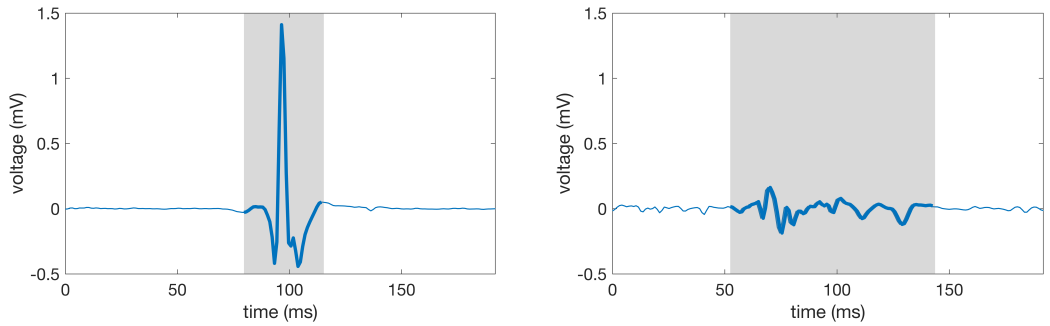

(a) Physiological EGM. **(b)** Fractionated EGM.

Figure 4.2: Excerpt of a physiological (a) and a fractionated (b) intra-atrial EGM. The active segment is shaded in gray.

Bipolar Voltage

The bipolar peak to peak voltage within each active segment was also considered as a feature.

Signal Power

The power P of the signal $s(n)$ of length N was defined as the sum of its squared amplitudes divided by its duration:

$$P = \frac{1}{N} \sum_{n=1}^{N} |s(n)|^2 \,. \tag{4.3}$$

Envelope Area

The envelope of the active segment was calculated as the amplitude of the analytic signal of the active segment with the help of the Hilbert transform. The area between the upper and the lower envelope of the active segment was considered the envelope area.

Figure 4.2 shows two exemplary EGM excerpts with the active segment shaded in gray. The physiological excerpt was recorded within the reference region while the fractionated excerpt originates from closest proximity to a micro-reentrant mechanism.

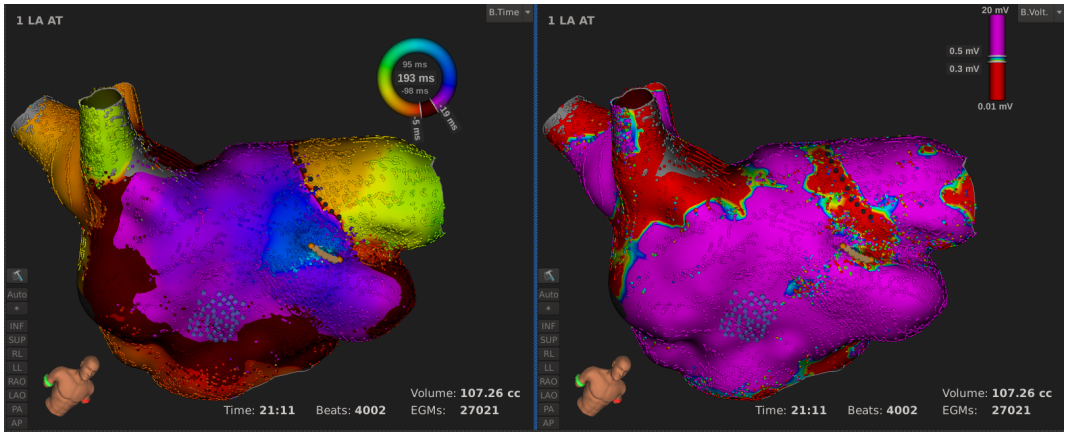

Figure 4.3: Rhythmia HDx screenshots displaying bipolar LAT and voltage map recorded during a micro-reentrant AFlut. Anterior superior oblique perspective. Reference tissue is tagged in blue, the micro-reentry in orange, and a line of block in black.

4.3 Results

4.3.1 Spatial Evolution of EGM Features for Selected Patients

The study cohort turned out to be diverse in EGM characteristics. Especially diseased atrial regions are hardly measurable by a common means. A set of exemplary cases will be presented in this section to demonstrate the risks and rewards of the proposed analysis methods.

To begin with, a micro-reentry embedded directly in healthy atrial tissue in combination with a very well mapped left atrium (LA) is presented in Fig. 4.3. Orange tags point out the site of the micro-reentrant mechanism.

Figure 4.4 assembles exemplary boxplots of a subset of the calculated EGM features. The activity duration and the sample entropy distinctly and abruptly decrease in a distance of 2 mm to the micro-reentry (compare Fig. 4.4 (a) and (b)). The Shannon entropy and the zero-crossing rate showed a more gradual transition starting at 2 mm and reaching the baseline level at about 7 mm (compare Fig. 4.4 (c) and (d)).

As a second example, a macro-reentry with slow conducting isthmus between the left inferior pulmonary vein and the mitral valve will be discussed. Figure 4.5 shows screenshots of both LAT map and bipolar voltage map. An extended area of low voltage surrounding the slow conducting isthmus manifests in the bipolar voltage map. In contrast, large parts of the LA maintain EGMs of high voltage.

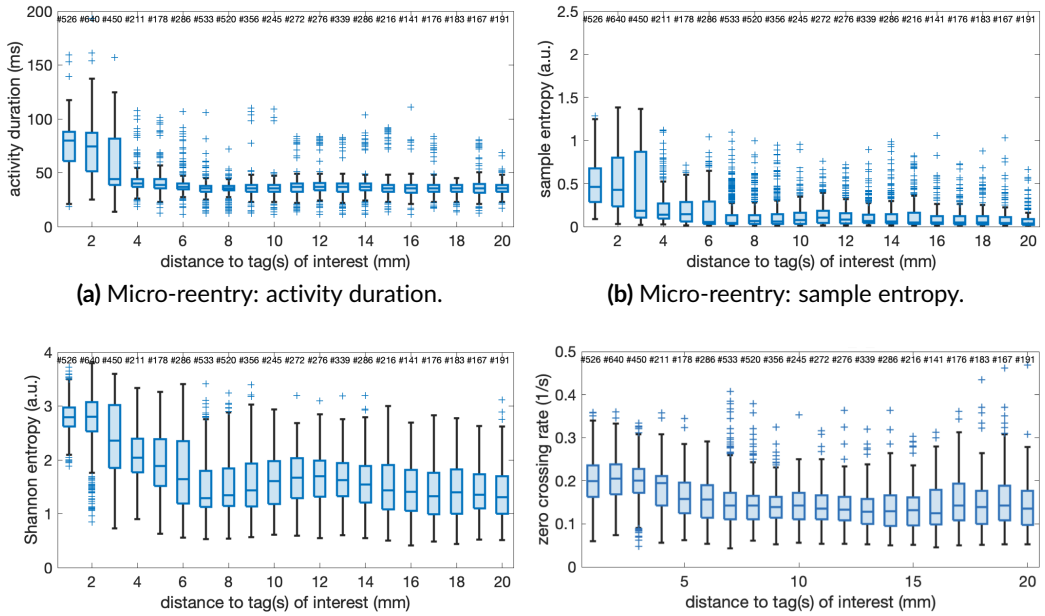

(a) Micro-reentry: activity duration.

(b) Micro-reentry: sample entropy.

(c) Micro-reentry: Shannon entropy.

(d) Micro-reentry: Zero crossing rate.

Figure 4.4: EGM features for layers of 1 mm width in vicinity to a micro-reentrant pattern. Numbers with a leading pound sign in the top row of the graph state the number of EGM segments contributing to the respective boxplot below.

Figure 4.6 (a) and (b) present the spatial evolution of selected EGM characteristics in vicinity of the slow conducting isthmus. As opposed to the previously discussed mico-reentry, the spatial dimension of elevated or reduced feature values is much broader and spans — depending on the feature — 7 mm to 13 mm. The smoothness of the transition and thus the width of the boundary zone also varies amongst the features.

A wavefront collision at the anterior wall of the same case was embedded in structurally presumably unaltered tissue. Figure 4.6 (c) and (d) show activity duration and bipolar voltage in vicinity of the wavefront collision. Activities lasted for less than 40 ms comparable to the activity duration within the reference tissue. Embedded in structurally unaltered tissue, the wavefront collision did not become apparent in either of the presented features. As a pure wave propagation phenomenon without significance for the derivation of pathological substrate, unaltered features were expected and support the use of EGM characteristics for substrate characterization.

4.3.2 Spatial Extent of Critical Regions

Visual inspection of the distance dependent boxplots showed that each dataset was individual. For the automatic calculation of the radial extent of critical sites of interest, the dataset was too diverse in terms of mapping quality, sampling density, degree of atrial disease, and

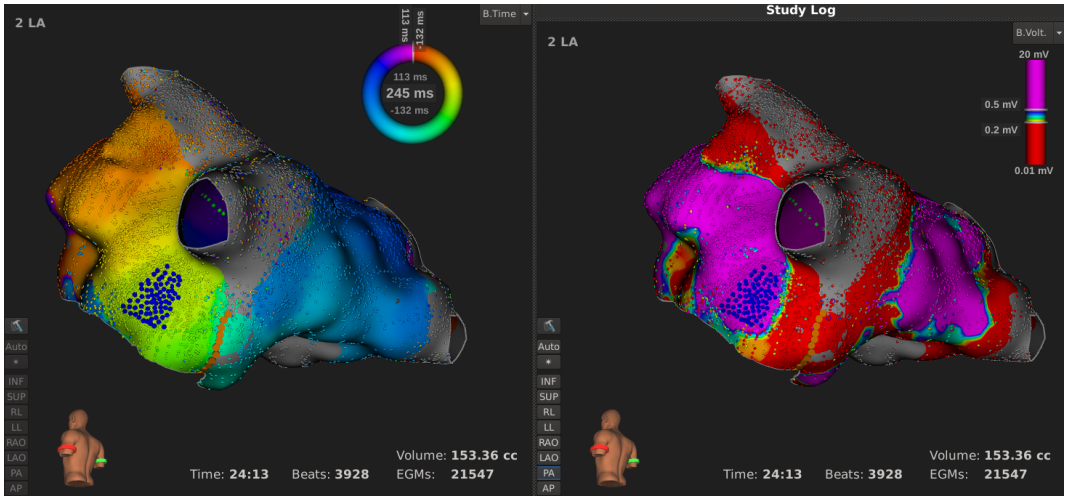

Figure 4.5: Rhythmia HDx screenshots displaying bipolar LAT and voltage map of a macro-reentrant left atrial AFlut. Reference tissue is tagged in blue, the slow conducting isthmus in orange.

combination of excitation propagation. In other words, for the automatic calculation of the radial extent of the critical site, a database of manifold cardinality would have been needed to cover the combination of differently altered substrate properties in different atrial regions for different wave propagation patterns.

The radial extent of each phenomenon was therefore reviewed manually for each EGM feature that showed a visible elevation or reduction of median values or quantiles. Medians and quantiles were compared to the reference value of the respective feature and the vicinity of the phenomenon of interest.

The minimum radial spatial dimensions measured 1 mm to 2 mm for clearly defined and well mapped lines of block and micro-reentries. Slow conducting isthmi varied from 2 mm to 13 mm in their spatial extent.

In summary, phenomena that were embedded in comparably healthy tissue showed clearer trends than phenomena within severely diseased tissue and low voltage areas. High density mapping facilitated the analysis due to the increased statistical power.

4.3.3 Inter-Patient Comparison of EGM Features

While the previous sections focused on individual cases and phenomena, an inter-patient analysis will condense the calculated features across the study cohort. Figure 4.7 shows the median value for each of the eight considered features grouped by the five phenomena of interest in addition to the reference tissue. The extracted feature values for recordings up to a distance of 2 mm to the phenomenon of interest were accumulated. For each case and each phenomenon, the median value of accumulated feature values is displayed in figure 4.7.

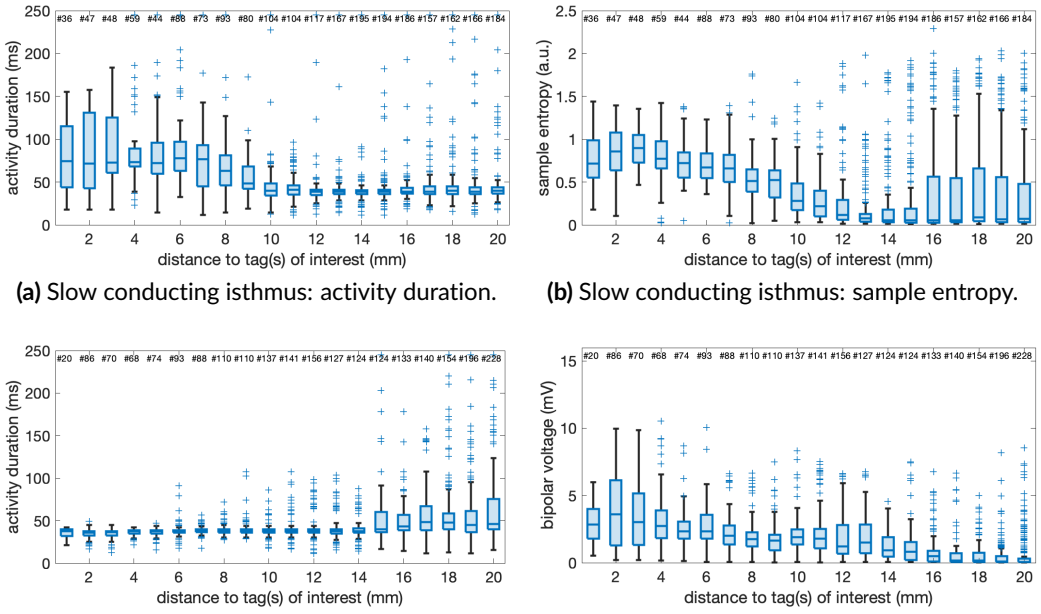

(a) Slow conducting isthmus: activity duration.

(b) Slow conducting isthmus: sample entropy.

(c) Wavefront collision: activity duration.

(d) Wavefront collision: bipolar voltage.

Figure 4.6: EGM features for layers of 1 mm width in vicinity to a slow conducting isthmus. Numbers with a leading pound sign in the top row of the graph state the number of EGM segments contributing to the respective boxplot below.

To start with, reference values for structurally healthy substrate and physiological excitation propagation were extracted. Especially the median activity duration in the reference region stood out as a well clustered accumulation ranging from 32.5 ms to 40.9 ms. Less but still condensed clusters were found for the reference entropies with the median sample entropy ranging from 0.0 a.u. to 0.2 a.u., and the median Shannon entropy ranging from 0.4 a.u. to 1.6 a.u. The median reference zero crossing rate ranged from 77 $\frac{1}{s}$ to 151 $\frac{1}{s}$. The signal power, the f 90 frequency, the spectral centroid, and the bipolar peak to peak voltage spread showed larger variance for reference tissue.

Feature values for colliding wavefronts were very similar to the reference values for all features. Considering that colliding wavefronts are only a result of the global excitation pattern and are unrelated to underlying tissue properties, this finding was in line with theoretical considerations. Only the entropy measures slightly exceed the reference values from a global point of view, which can be explained by two superimposed activations being less organized than excitation without interference. The signal power as well as the bipolar peak to peak amplitude decreased to a minimum for lines of block, micro-reentries, and slow conducting isthmi.

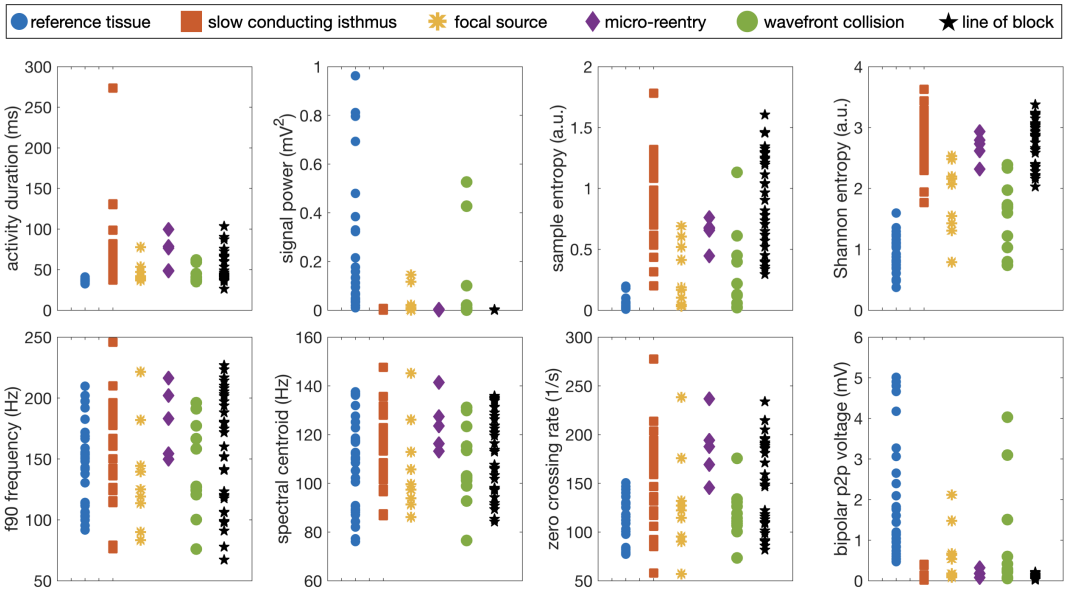

Figure 4.7: Median EGM feature values grouped by the phenomenona of interest.

4.4 Discussion

A variety of EGM characteristics was calculated for well annotated reference areas and pathological sites during atypical left AFlut. Especially activity duration and entropy exhibited narrow reference distributions. Feature distributions for pathological phenomena were broad and could not be narrowed down to exclusive sets. Activity duration, sample and Shannon entropy, as well as bipolar voltage were distinctly discriminative for reference areas. Micro-reentries stood out in frequency dependent features such as the zero crossing rate and the spectral centroid. Distinguishing between different pathologies purely based on EGM features was not possible for the given cohort due to an overlap of feature spectra and the restricted cardinality of the dataset. Atypical AFlut occurs in a multitude of different forms and combinations of excitation patterns and substrate pathologies that are difficult to handle by a common means. EGM features can help to highlight pathological areas that should be examined in further detail. In combination with LAT mapping and knowledge of the excitation pattern, the presented feature sets can enhance electrophysiological diagnosis especially by unravelling arrhythmogenic substrate currently not involved in the clinical AFlut mechanism.

Chapter 5

Noise Quantification and Noise Reduction in Unipolar and Bipolar Electrograms[1]

5.1 Introduction

The analysis of intracardiac electrograms (EGMs) is a cornerstone in deducing arrhythmia mechanisms during electrophysiological studies. Both visual review by experienced electrophysiologists and computation of EGM features are highly dependent on the signal quality. However, undesirable components such as high and low frequency noise, the ventricular far field, power line hum, and other parasitic frequencies overlay the EGM of interest. Various techniques have been proposed to eliminate disturbances among which the calculation of bipolar leads has evolved to be the clinical standard [38]. Far field noise occurring equally in both unipolar leads of a bipolar pair is automatically removed by subtraction. Combining two unipolar leads yet implicates loss of spatial accuracy and morphological features and introduces dependencies on the direction of excitation propagation [39][40]. Despite overcoming these disadvantages, unipolar EGMs are rarely used due to a lack of efficient noise removal methods. Opposed to bipolar EGMs, even the removal of far field noise is demanding since the components do not simply cancel out. The three-dimensional electroanatomical mapping system (EAMS) Rhythmia HDx™ claims to lower the bipolar noise level down to 0.01 mV [41] with the IntellaMap Orion™ catheter (Boston Scientific, Malborough, MA, USA) and thus to reveal low voltage EGM components which are of particular interest for a detailed diagnosis. Information on the noise level of an EAMS is crucial to understanding its strengths but also its limitations regarding the minimally resolvable voltage amplitude. In this study, we systematically quantified the noise level of both unipolar and bipolar EGMs recorded

[1] The content of Chapter 5 was previously published in [37] under the CC-BY license and is in large parts accounted word-for-word in this work. The work presented in Chapter 5 was supported by Boston Scientific.

with the IntellaMap Orion™ catheter in a multi-center study. In a second step, we further developed a method for removing distinct noise peaks in frequency domain and assessed the resulting reduction of noise levels.

5.2 Methods

5.2.1 Clinical study cohort

Patients with stable atrial tachycardia and unequivocal driving mechanism were extracted from the international, multi-center TrueHD database (Boston Scientific, Malborough, MA, USA) of ultra-high-density mapping gathered with the IntellaMap Orion™ catheter using the Rhythmia HDx™ EAMS. A total of 33 patients from 17 centers met the above-mentioned inclusion criteria. For each case, an area of reference tissue was annotated. Reference tissue was required to exhibit bipolar voltage amplitudes larger than the clinical standard of 0.5 mV and needed to be passed by a planar wavefront with physiological conduction velocity.

5.2.2 Quantification of Noise Levels

Distinguishing between noise and atrial activity is a non-trivial task for pathological EGMs of potentially low voltage amplitudes. However, for quantifying the noise level of an EGM segment, we needed to assure that the respective segment merely consisted of noise and was not exposed to possible other sources of EGM alteration. Using only EGMs that fulfilled the beat acceptance criteria of the EAMS and that were recorded within the annotated reference area assured reliable separability of active and inactive EGM segments since atrial activity complexes were expected to be narrow, sharp, and of high amplitude. Atrial activity was detected with the non-linear energy operator [42] in intervals of 2 s duration centered around each accepted beat. An EGM segment was considered active if the activity persisted for at least 10 ms and inactive in any other case. Post-processing merged active segments closer than 30 ms. Additionally, QRS complexes were detected in Einthoven lead I of the surface electrocardiogram (ECG) [43][34] and labelled as active for all EGM leads. For any remaining inactive segment, the baseline was removed using two different approaches: Fitting and subtracting a 5^{th} order polynomial or highpass filtering with a cutoff frequency of 30 Hz. Both approaches were independently applied to the database and compared in the end. The resulting signals were considered to contain noise only. In order to prevent boundary effects from distorting the results, the onset and the offset of the remaining segments were cropped by 5 ms each. The maximum absolute peak to peak voltage of the inactive segment quantified the noise level conservatively.

5.2.3 Removal of Distinct Noise Frequencies

The power spectral density (PSD) of recorded EGMs revealed distinct, narrow peaks exceeding their surrounding in amplitude, hence being considered noise. Atrial activity was also present in the recorded EGMs causing broader alterations in the PSD and thus not interfering with the noise peaks. Under the assumption that noise frequencies continuously overlaid the recordings during the entire intervention, the longest consecutive EGM recording was chosen for determining noise frequencies in order to achieve the highest possible resolution in frequency domain. For a recording of length T, the frequency resolution of the PSD is given by $\Delta f = \frac{1}{T}$. A sliding window of width w was shifted along the PSD [44]. For each window position f covering the interval $[f - \frac{w}{2}; f + \frac{w}{2})$, the maximum amplitude of the PSD within the sliding window was compared to the maximum amplitude within the consecutive intervals of width $20w$ to the left and the right of the central window. If the maximum spectral amplitude within the central sliding window exceeded the maximum amplitude within the consecutive windows by at least 6 dB, the frequency exhibiting the prominent peak was considered noise. For frequencies larger than or equal to 45 Hz, the peaks were removed with a notch filter of width w. The PSD of the filtered signal was recursively checked for peaks. The approach was then repeated for window widths w increasing from 10 samples in frequency domain to a maximum width of 0.3 Hz in steps of 10 samples. Assuming that noise equally affects all electrodes of the IntellaMap Orion™ catheter, peaks were determined for one unipolar lead only while notch filtering was applied to all leads. In order to distinguish between the power line hum and other noise frequencies, the peak between 45 Hz and 65 Hz with the highest amplitude was considered the power line frequency f_{PL} with corresponding harmonics if peaks were present at $n \cdot f_{\mathrm{PL}}, n \in \mathbb{N}$.

5.2.4 Filter settings

For unipolar EGMs, clinical standard filtering with a highpass and lowpass cutoff frequency at 1 Hz and 300 Hz removed high and low frequency noise from the acquired EGM. The clinical standard filter setting also included the application of Gaussian notch filters to the power line frequency and its harmonics. An extended filter setting consisted of additional notch filters for the remaining set of detected noise frequencies for unipolar EGMs. Bipolar EGMs were only subject to clinical standard filtering with a high- and lowpass cutoff frequency of 30 Hz and 300 Hz.

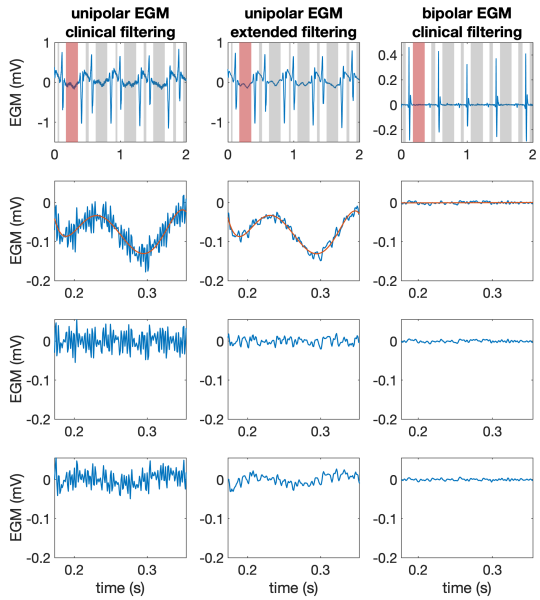

Figure 5.1: First row: EGM traces of 2 s length. Inactive segments are shaded in gray and red. Second row: Magnified representation of the inactive EGM segment shaded in red. The red curve depicts the polynomial baseline fit. Third row: Resulting inactive segment after polynomial baseline removal. Fourth row: Resulting inactive segment after baseline removal by highpass filtering. The three columns depict the clinically filtered unipolar EGM, the unipolar EGM after extended filtering, and the clinically filtered bipolar EGM, respectively. [37]

5.3 Results

5.3.1 Noise Frequencies in Unipolar EGMs

Figure 5.1 visualizes the workflow for the quantification of the noise level on an exemplary basis. The absolute peak to peak voltage of the processed inactive signal was used as a measure for the noise level of the EGM segment.

Figure 5.2 (a) shows the PSDs of the raw EGM recording, after clinical filtering, and after extended filtering. The power line frequency was detected at 60 Hz with corresponding harmonics. The clinical filter setting left the PSD with numerous distinct noise peaks that were removed by extended filtering to increase signal quality.

Figure 5.2 (b) depicts the clinical EGMs corresponding to the PSDs in Figure 5.2 (a). The raw clinical recording was distorted by several noise frequencies. After clinical filtering, i.e. high- and lowpass filtering and removal of the power line frequency and corresponding harmonics, the noise level decreased. The extended filter setting yielded a clear EGM consisting of sharp atrial activities alternating with broader deflections caused by the ventricular far field.

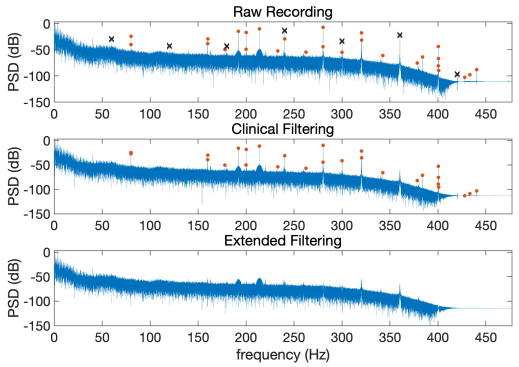

(a) PSDs of the raw unipolar EGM, after clinical filtering, and extended filtering.

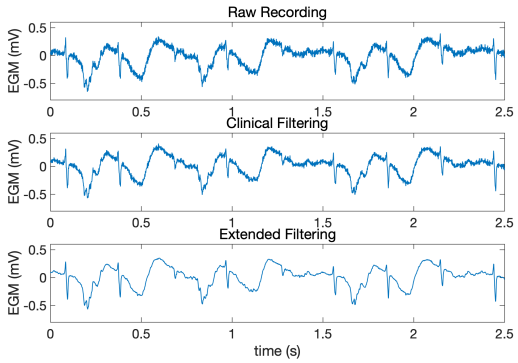

(b) Raw unipolar EGM recording, EGM after clinical filtering and EGM after extended filtering.

Figure 5.2: PSD of the raw unipolar EGM, after clinical filtering, and extended filtering (a). Black crosses mark the detected power line frequency and corresponding harmonics. Red dots label additional noise frequencies. Corresponding raw unipolar EGM recording, EGM after clinical filtering and EGM after extended filtering (b). [37]

In each of the 33 cases of the multi-center study cohort, we found distinct noise peaks at 80 Hz and the respective harmonics. Furthermore, noise was present at 120 Hz, 200 Hz, 360 Hz, and 440 Hz for all analyzed cases. A set of additional frequencies was repeatedly detected in the majority of the cohort. Other noise frequencies occurred only in single cases.

5.3.2 Noise Level of Rhythmia HDx™

From the whole cohort, 40 574 and 42 321 inactive segments were extracted from the unipolar and bipolar EGMs recorded within the reference area, respectively. Figure 5.3 shows the median noise level as well as the 25 % and 75 % quantile for clinical and extended filter settings applied to unipolar EGMs, and the clinically filtered bipolar EGMs. For the highpass filtering approach for baseline removal, the median noise level for clinical and extended filter settings for unipolar EGMs as well as for clinical filter settings for bipolar EGMs measured 0.110 mV, 0.076 mV, and 0.010 mV, respectively. For the polynomial baseline removal, the median noise level measured 0.105 mV, 0.062 mV, and 0.016 mV, respectively. Additional filtering reduced the noise level significantly ($p < 0.0001$) as compared to the clinical filter settings.

5.4 Discussion

Unipolar EGMs are distorted by a multitude of noise frequencies. For a possible transfer of unipolar EGMs to clinical practice, effective filtering that exceeds the current clinical standard of only removing the power line frequency is inevitable. The proposed method of

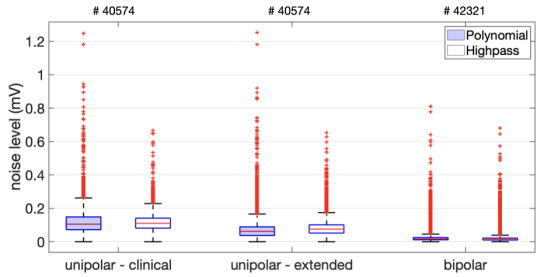

Figure 5.3: Noise levels of 40 574 segments for unipolar EGMs after clinical and extended filtering as well as for bipolar EGMs. The baseline was removed by subtraction of a polynomial fit or 30 Hz highpass filtering. The red line marks the median noise level. The blue box surrounds the 25 % and 75 % quantile. Red crosses depict outliers beyond the 5 % and 95 % quantile as indicated by black bars. [37]

pinpointing distinct noise peaks in the PSD and subsequent removal from the EGMs proved to be effective.

Both postprocessing approaches for baseline removal yielded similar noise levels. The filtering approach was more robust with little number of outliers but remnant low-frequency oscillations, which caused the unipolar noise level to slightly exceed the results of the polynomial approach. The polynomial approach, on the other hand, decreased the remnant oscillations on the cost of an increasing number of outliers.

Deeper analysis revealed that, opposed to the assumptions made above, there are systematic inter-electrode differences in the PSDs. In particular, the proximal electrodes 7 and 8 on each spline of the IntellaMap Orion™ were susceptible to additional noise frequencies. However, this work did not further investigate inter-electrode variations of the PSD but applied the same filter settings to all leads. Electrode specific filtering will need to be investigated in a follow-up study. We also saw time dependent occurrences of certain noise frequencies. In order to account for the temporal dynamics of noise, the spectral analysis needs to involve a temporally resolved component. Instead of using a set of fixed window widths w for peak detection in the PSD, the advantages determining the actual peak width from the PSD need further investigation. Center specific noise frequencies resulting from the individual setup of the electrophysiology laboratory could be quantified and used as background knowledge for the individual EAMS setup. Noise levels determined in this study were a conservative estimate of the actual noise level of the system. The presented workflow is expected to slightly overestimate the noise level since suboptimal baseline removal in the inactive segment, e.g., elevates the result. Therefore, the resulting noise levels can be considered an upper limit of expected additive noise amplitudes.

To conclude, we quantified the noise level for unipolar and bipolar EGMs recorded with the Rhythmia HDx™ EAMS and the IntellaMap Orion™ catheter and thus gave insight into the minimally resolvable voltage amplitudes during an electrophysiological study. The measured bipolar noise level of 0.010 mV met the Rhythmia HDx™ system specification [41]. A low noise floor allows to further discriminate regions of low voltage to specify diagnosis.

Furthermore we showed that carefully chosen extended filtering significantly improves the signal quality and should be applied to unipolar EGMs in clinical practice. Despite the lower noise level in bipolar leads, this study enhances potential use of unipolar leads and encourages electrophysiologists to leverage morphological and spatially resolved features that exceed the information content of bipolar EGMs.

PART III

LOCAL ELECTRICAL IMPEDANCE MEASUREMENTS IN THE ATRIA

Chapter 6

Morphological Analysis of Local Impedance Drops during Radio Frequency Ablation

6.1 Introduction

The creation of transmural and durable lesions is core to sustainable ablative treatment of cardiac arrhythmia. Commonly drawn atrial ablation lines such as anterior or roof lines but also ipsilateral encircling of the pulmonary veins (PVs) are prone to developing gaps if radio frequency energy was delivered inefficiently. Throughout the years, electroanatomical mapping systems (EAMSs) have come up with a diverse set of surrogate measures for real-time assessment of lesion formation. The force-time integral [45] and the ablation index [46] are two popular examples commonly aiming at estimating the amount of energy deposited in the atrial tissue. Generator impedance has also become an established tool to assess catheter-tissue coupling by measuring the impedance of the energy delivery pathway. However, the bulk impedance of the torso limits local resolution. The recently developed DirectSense™ technology [13] provides a more local picture by comprising both the injection and measurement circuit within the intra-cardiac catheter. The so-called local impedance (LI) reflects resistive tissue heating and is thus indicative for effective lesion formation [47] [13]. The LOCALIZE [47] and the CHARISMA [48] trial have shown that the absolute LI drop during ablation delivery predicts lesion durability [47] [48]. While most early-stage studies [49] [50] [51] focused on the assessment and investigation of initial LI upon the start of ablation and LI drops in comparison to the respective generator impedance parameters, this work draws detailed attention to absolute values and morphology of the LI drop upon radio frequency energy delivery. Particularly, features of LI traces are compared by procedural timing, anatomical region, and applied power.

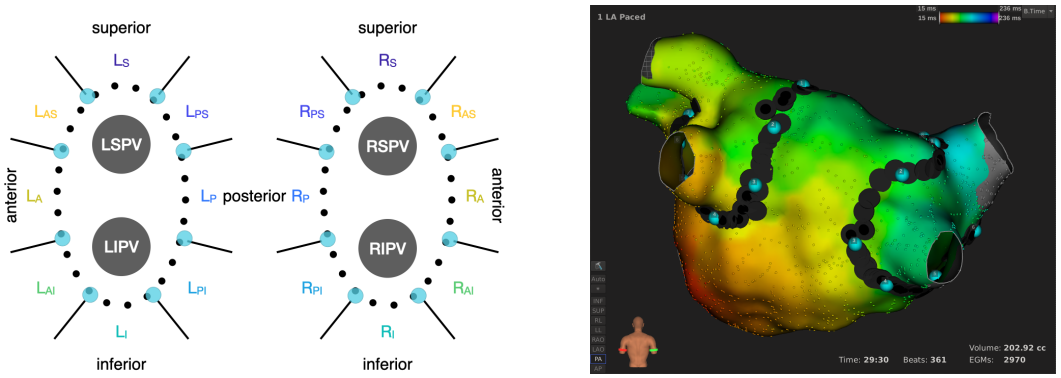

(a) Schematic subdivision of PVI circles.

(b) Clinical subdivision of PVI circles.

Figure 6.1: Subdivision of left and right ipsilateral PVI circles into eight sections. Black dots represent the ablation line, light blue dots the boundaries of the sections. Schematic view (a) and clinical example (b) posterior-anterior view. The underlying local activation time (LAT) map was recorded during pacing from the coronary sinus (CS). L_S: left superior, L_{PS}: left posterior/superior; L_P: left posterior; L_{PI}: left posterior/inferior; L_I: left inferior; L_{AI}: left anterior/inferior; L_A: left anterior; L_{AS}: left anterior/superior; R_S: right superior, R_{PS}: right posterior/superior; R_P: right posterior; R_{PI}: right posterior/inferior; R_I: right inferior; R_{AI}: right anterior/inferior; R_A: right anterior; R_{AS}: right anterior/superior. Inspired by [47].

6.2 Methods

6.2.1 Study Design

This was a retrospective, single-center study which was conducted in accordance with the Declaration of Helsinki. The study was approved by the local ethics committee.

All patients undergoing a de-novo pulmonary vein isolation (PVI) procedure with the RhythmiaHDx (Boston Scientific, Malborough, MA, USA) EAMS and the IntellaNav MiFi™ OI (Boston Scientific, Malborough, MA, USA) were included into the study cohort if both ipsilateral circles proved successful first-pass isolation at the end of the procedure.

The study protocol included a full-chamber left atrial map in a rhythm of the physician's choice. Subsequently, point-by-point PVI was performed with the IntellaNav MiFi™ OI starting either with the isolation of the left PVs and proceeding with the right or vice versa. Each ablation delivery was marked by a manual or automatic tag annotation. At the end of the procedure, successful isolation of all PVs was confirmed.

After completion of the study, the geometry, catheter location, ablation tags, LI data, and information on radio frequency energy generator settings were exported from the system for retrospective analysis. Both ipsilateral PVI circles were subdivided into eight sections as schematically depicted in Fig. 6.1 [47]. Each ablation delivery was assigned to a section by the minimum geodesic distance.

6.2.2 Feature Calculation

For each ablation delivery, the LI trace was extracted from the onset to the offset of radio frequency energy delivery. Following the clinical EAMS, a moving average filter with a window length of 1.5 s was applied to the raw LI trace to handle oscillations. If not otherwise mentioned, LI refers to the post processed signal in the following. Average LI traces were determined by calculating the mean over all LI values for each time instance aligned by the start of ablation. Since the duration of ablation delivery differed between ablations, early time steps comprised more samples for averaging than later time steps. The steepness of the LI drop was estimated by the difference quotient of the mean LI trace. A step width of 1 s aimed at preventing noise and artefacts from flawing the result.

The following features characterized the morphology of the LI drop:

- **initial LI** upon the start of ablation
- total **LI drop ΔLI** calculated as the difference between the initial LI and the minimally observed LI.
- **maximum (absolute) steepness**.
- **time of maximum steepness** in respect of the onset of ablation.
- **time** passing **until an LI drop of 12 Ω** was first reached. An LI drop of 12 Ω had previously been found to be the optimal cut-off value for posterior and inferior segments [47].
- **time** passing **until an LI drop of 16 Ω** was first reached. An LI drop of 16 Ω had previously been found to be the optimal cut-off value for anterior and roof segments [47].
- **mean LI oscillation amplitude** calculated as the mean deviation between the raw impedance recording and its moving average.

6.2.3 Statistical Analysis

Distributions are reported by their mean $\pm$ standard deviation or median and interquartile range (IQR) as appropriate. Non-normal distributions with unpaired samples were compared with the Mann-Whitney U-test and a significance level of 1 %. The central line of all boxplots describes the median while the boxes range from the 25^{th} to the 75^{th} percent quantile. The whiskers extend to the outermost data points that were not considered outliers. The linear dependency of two variables was analyzed by means of linear regression.

Table 6.1: Features extracted from LI drops during radio frequency ablation delivery with the IntellaNav MiFi™ OI.

Feature	Median	IQR
Initial LI (Ω)	106.01	19.38
LI drop (Ω)	18.83	11.46
Maximum steepness ($\frac{\Omega}{s}$)	−3.63	3.37
Time (s) of maximum steepness	1.40	3.45
Time (s) to $\Delta LI = 12\,\Omega$	5.85	6.90
Time (s) to $\Delta LI = 16\,\Omega$	7.60	8.85
Mean oscillation amplitude (Ω)	3.17	1.79

6.3 Results

A total of 54 patients (31 male) diagnosed with paroxysmal or persistent atrial fibrillation (AFib) were included in the study. A mean age of 64 ± 10 years and a mean left atrial volume of 166 ml ± 43 ml characterized the patient cohort. On average, 78 ± 16 ablations with a mean duration of 24.1 s ± 12.7 s were delivered during PVI, summing up to a total of 4186 analyzed ablation deliveries. 20 % of all ablations were delivered at a maximum power of 30 W, 40 % at 35 W, and 36 % at 50 W. The remaining 4 % were performed at differing power. For 47 patients, left PVI preceded right PVI. In the remaining 7 cases, the procedure started with right PVI. Bloodpool LI was measured for 30 patients resulting in a mean of $98.2\,\Omega \pm 8.7\,\Omega$.

6.3.1 Anatomical Location and Procedural Time

Table 6.1 summarized median and IQR of LI drop characteristics across all ablation deliveries. The previously found optimal cut-off values [47] of 12 Ω and 16 Ω were reached after a median ablation time of 5.85 s and 7.60 s, respectively. The median ablation delivery reached a maximum steepness of $-3.63\,\frac{\Omega}{s}$ approximately 1.40 s after the start of ablation.

Fig. 6.2 visualizes the distributions of LI drop characteristics divided by eight left PVI and eight right PVI segments. As indicated by Fig. 6.2 (a), left PVI typically started in the anterior superior region and proceeded in clockwise direction towards the posterior wall and continued with the right PVI starting from the anterior superior region in clockwise direction towards the anterior wall. Fig. 6.2 (b) to (d) visualize the distributions of initial LI, LI drop, and oscillatory amplitude. Distributions were significantly different comparing all pairs of anatomical segments. Initial LI was highest for early ablation deliveries and decreased for segments ablated later on, particularly distinctive for the left PVI. Analogously, LI drops were larger for early applications compared to later applications, comparably distinctive for the left and right PVI. The mean oscillatory amplitude followed the same trend. The remaining features including the maximum steepness, the time of maximum steepness, and the times

to LI drops of 12 Ω and 16 Ω did not differ significantly for the majority of anatomical segments.

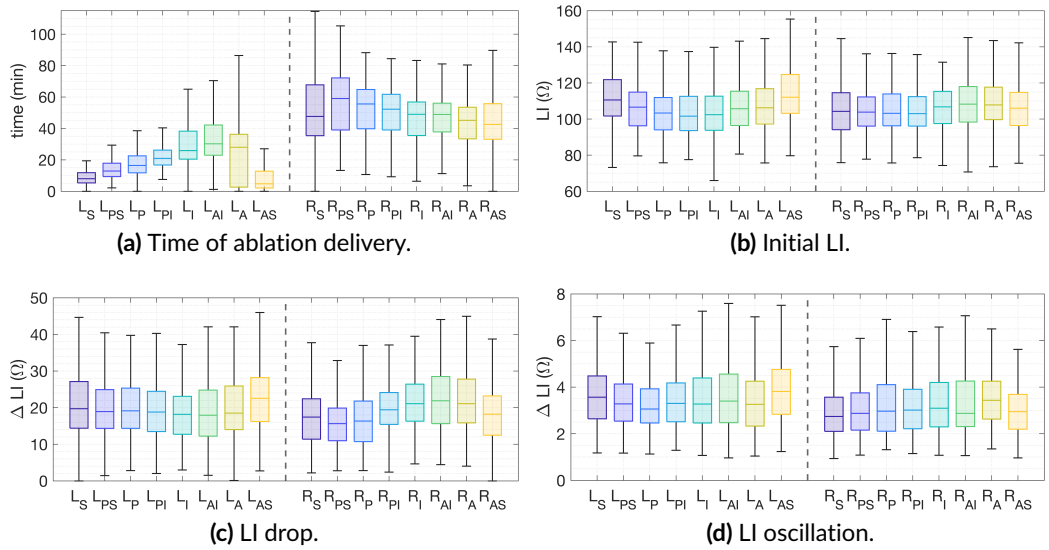

(a) Time of ablation delivery. **(b)** Initial LI. **(c)** LI drop. **(d)** LI oscillation.

Figure 6.2: Distribution of various LI drop parameters by PVI segment across all patients. All distributions are statistically significantly different. Segment labels on the horizontal axis as introduced in Fig. 6.1.

Fig. 6.3 further illuminates the dependency of the initial LI upon the start of ablation delivery on the progress of the overall procedure time. Linear regression suggested that the initial LI at the start of an ablation delivery decreased by 7.3 Ω per hour after the first ablation delivery.

Fig. 6.4 (a) and (b) display mean traces of LI drop for the left and right PVI segments. The traces are of similar morphology but shifted along the vertical axis. Early traces in terms of procedural time tend to exceed later traces. However, not every detail can be explained by

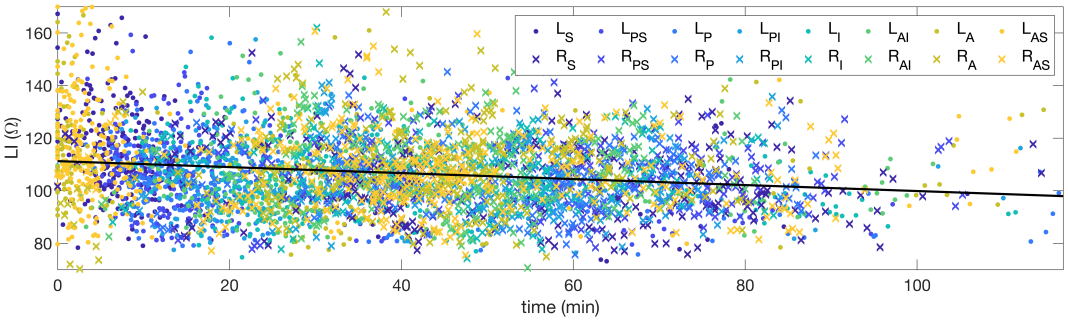

Figure 6.3: LI at the beginning of radio frequency energy delivery over procedural time. Dots mark left PVI ablations; crosses mark right PVI ablations. Colors label segments as introduced in Fig. 6.1. A linear regression is superimposed in black.

procedural timing. The left anterior / inferior segment, for example, was the one handled last (compare Fig. 6.2 (a)) but does not show the lowest trace in Fig. 6.4 (a). Since procedural time was directly correlated with anatomical segments for the majority of cases, a control group with inverted order of the PVI procedure was analyzed separately. Fig. 6.4 (c) and (d) display the respective mean traces. The mean trace of all left PVI deliveries exceeded the right if the procedure started with left PVI. If, on the contrary, the procedure started with right PVI, the mean trace of right PVI exceeded the left indicating a more dominant correlation to the procedural time as compared to anatomical location.

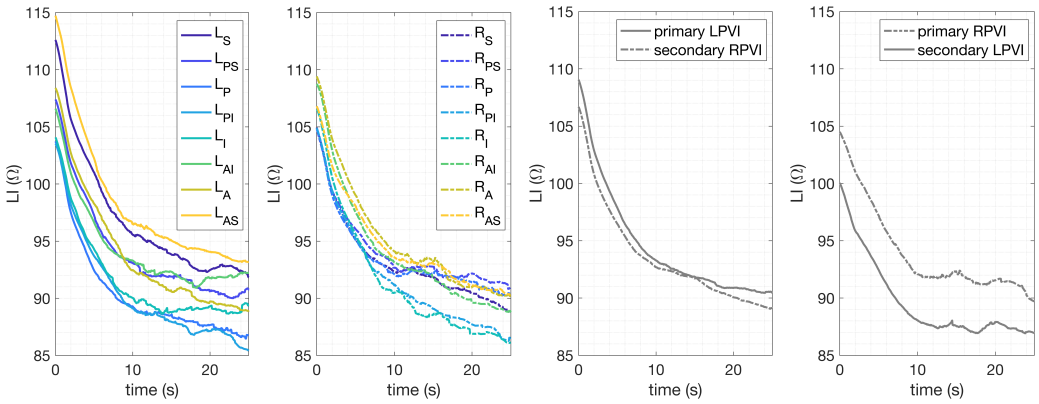

(a) Left PVI segments. **(b)** Right PVI segments. **(c)** Left PVI preceding right PVI. **(d)** Right PVI preceding left PVI.

Figure 6.4: Mean traces of LI drop during radio frequency energy delivery by anatomical sections and procedural timing.

6.3.2 Radio Frequency Power

Fig. 6.5 describes the dependency of maximum steepness, time of maximum steepness, time to an LI drop of 12 Ω, and time to an LI drop of 16 Ω. While the distributions did not differ between a power of 30 W and a power of 35 W, the distribution for a power of 50 W differed significantly both from 30 W and 35 W for the mentioned features. The traces were found to be steeper, to reach the maximum steepness earlier and to take less time until LI drops of 12 Ω and 16 Ω compared to applications at lower power of 30 W and 35 W.

Fig. 6.6 (a) and (b) visualize the difference caused by distinct power settings by means of the mean LI trace and the mean difference quotient.

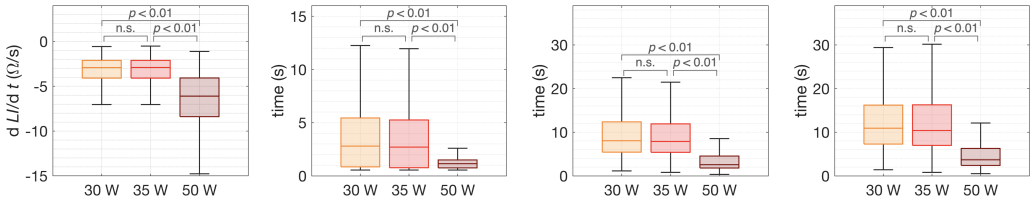

(a) Maximum steepness. **(b)** Time of maximum steepness. **(c)** Time to Δ LI = 12 Ω. **(d)** Time to Δ LI = 16 Ω.

Figure 6.5: LI drop features by radio frequency ablation power of 30 W, 35 W, and 50 W. Significance is denoted above the boxplots (n.s.: not significant).

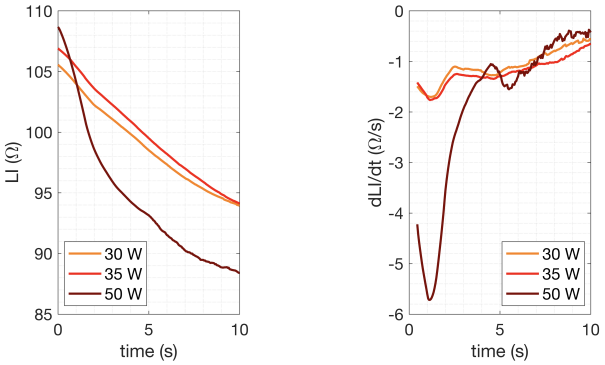

(a) Mean LI trace. **(b)** Difference quotient.

Figure 6.6: Mean LI trace over all ablation deliveries (a) and corresponding difference quotient calculated with a window of 1 s duration (b).

6.4 Discussion

Analyses demonstrated that the initial LI at the start of ablation and the total LI drop are dependent on the procedural time while features related to the steepness of the curve showed strong dependency on the radio frequency power.

The progressive decrease of the LI at the start of ablation deliveries over the course of the procedure could be attributed to multiple factors. With the increasing number of delivered ablations, atrial tissue is progressively damaged and forms edema that potentially alter the baseline LI. Additionally, the volume of physiological sodium chloride (NaCl) solution entering the circulatory system as a result of catheter irrigation increases cumulatively, especially due to an increased flow rate during ablation delivery. Since the baseline LI of physiological NaCl solution measures only half of the average bloodpool LI, [17] [52], the progressive decrease in LI with procedure time could be related [53]. Additionally, different anatomical regions are reached with different complexity of catheter maneuvers resulting in varying contact force and thus tissue coupling. The presented results suggest that the

variation in initial LI is mainly attributed to procedural time and additionally depends on the anatomical location of ablation delivery.

The dependency of slope related features on the radio frequency power support the basic assumption that the amount of deposited energy in the tissue is reflected by the LI drop. With power being energy over time, equal amounts of energy deposition are reached in shorter time for higher power — assuming comparable catheter-tissue coupling.

The steepness of the ablation drop exhibited a maximum approximately 1.4 s after the onset of ablation indicating an initial booting phase. The latter could potentially be related to delays in establishing maximum flush and up-regulating power or to progressive tissue heating before full destructive efficacy.

Mean LI drop traces tended to become more noisy for later points in time reflecting longer ablation times. This effect is attributed to the fact that ablation times differed. While all deliveries lasted for the first few seconds after their respective onset, the amount of deliveries dropping out for later points in time increased due to earlier ablation offset. Therefore, the lower number of samples for later points in time resulted less smoothing and higher degree of noise.

Despite availability, the LI was not referenced to a patient specific bloodpool LI in order to support direct comparability to clinical traces. The large amount of patients helped to statistically outnumber variations in individual bloodpool LI. Still, the variance of observed absolute feature values described in this work remains partially attributed to baseline variations in bloodpool LI.

In summary, this study shed light on the morphology and on absolute values of LI drops during radio frequency energy delivery in de-novo PVI with first-pass isolation. Reference values were provided for a set of characteristic drop features. Dependencies on the power settings as well as on anatomical location and procedural time were outlined to further enhance the comprehension of clinically observed traces in the future.

Chapter 7

In Silico Study of Local Electrical Impedance Measurements in the Atria - Towards Understanding and Quantifying Dependencies *in Human*[1]

7.1 Introduction

Electrical impedance measurements have a long history in the medical and biomedical field. Historical studies have shown that different kinds of biological tissues are characterized by different conductivity spectra [55] attributed to the microscopic composition of the materials [56]. Besides the composition of the material and the measurement frequency, electrode arrangement and temperature are major determinants of the measured impedance.

During invasive cardiac electrophysiological studies, generator impedance measurements have been an established method to monitor the delivery of radio frequency energy during ablation since decades [57][51]. The transthoracic impedance of the radio frequency energy delivery pathway between an intracardiac and a cutaneous dispersive electrode assists differentiation of tissue contact during ablation. However, the bulk impedance of the torso blurs measurements [58][59] and impedes detailed assessment of tissue characteristics in the region of interest next to the catheter. Recently, two novel catheters have been introduced to the market that aim at a more locally focused impedance assessment in the vicinity of the catheter with all injecting and measuring electrodes being built into the intracardiac catheter itself [51]. The radio frequency ablation catheters IntellaNav MiFi™ OI [13] and

[1]The content of Chapter 7 was previously published in [54] under the CC-BY license. © 2022 IEEE. Reprinted, with permission, from [54].

IntellaNav Stablepoint™ [60] (Boston Scientific, Malborough, MA, USA) come with a four-electrode and a three-electrode impedance measurement circuit implemented within the catheter, respectively. During ablation, the so-called DirectSense™ technology measures the magnitude of the local impedance (LI). An LI drop resulting from a combination of resistive tissue heating and subsequent myocardial destruction and lesion formation is used as a surrogate for lesion quality and durability [13][47]. Compared to the transthoracic generator impedance, the LI emphasizes local changes in impedance while being less susceptible to far field artifacts [47][48][49][50]. Despite an increased influence of the local surroundings on the measurement compared to the generator impedance, the LI is still sensitive to the three-dimensional arrangement of materials and their properties surrounding the catheter [61]. LI may therefore not be mistaken for lumped impedance measurements, which condense all influencing properties to an infinitesimal element. Besides the monitoring of ablation lesion formation, LI has also shown potential to characterize cardiac tissue and differentiate between healthy myocardium and fibrotic or scar tissue [50][49][48]. Atrial fibrillation as the most common sustained cardiac arrhythmia poses a major burden for both patients and global health care systems. Since current treatment approaches result in unsatisfactory success rates, novel methods of tissue characterization such as the LI need further exploration.

A major challenge in the expansion of the diagnostic value of intracardiac LI measurements are confounding factors. Not only different tissue compositions but also the distance and angle between the catheter and the tissue, the surrounding tissue geometry, an overlap of catheter and transseptal sheath, and sodium chloride (NaCl) solution irrigation influence the measurement, amongst others. Many of these effects can be observed in *in human* studies but lack quantification due to the superposition of multiple effects and an unknown ground truth. Therefore, the differentiation between the target measure and confounding factors has remained uncertain. *In vitro* and *ex vivo* experiments can help to shed light on different scenarios but are costly and depending on the experimental setup, the underlying ground truth still remains under-determined.

In this work, we present for the first time a highly detailed *in silico* framework that models the IntellaNav MiFi™ OI catheter and the IntellaNav Stablepoint™ catheter in combination with different clinically relevant surroundings. After validation of the framework by *in vitro* measurements in standardized setups, clinically relevant scenarios such as the effect of the distance and angle between catheter and tissue, scar tissue, the insertion of the catheter into a pulmonary vein (PV) or a transseptal sheath, and NaCl solution irrigation were investigated and compared to *in vitro* and *in human* measurements.

With a highly detailed comparison between different catheter geometries and the investigation of isolated scenarios to quantify various clinically relevant effects, this work paves the way for an inexpensive enhancement of the understanding of intracardiac LI measurements and future catheter development.

7.2 Methods

7.2.1 *In Silico* — Geometrical Setup

Both clinically available LI-enabled radio frequency ablation catheters were modeled in high detail as depicted in Fig. 7.1 (a) to (d). Measures were taken from product specification sheets [62][63] as well as calibrated photographs yielding a resolution below 100 µm.

The IntellaNav MiFi™ OI comes with a 4.5 mm tip electrode, three ring electrodes of 1.3 mm width and 2.5 mm spacing, three evenly distributed mini electrodes of 0.8 mm diameter embedded in the tip electrode, six irrigation holes, and a cooling chamber filled with NaCl solution. The interior of the catheter is electrically isolated from the electrodes and accommodates thin electrical and mechanical steering wires. While neglecting the latter, the interior of the catheter shaft was filled with insulating material in the model.

The IntellaNav Stablepoint™ is similarly composed of a 4 mm tip electrode, three ring electrodes of 1.3 mm width and 4.0 mm | 2.5 mm | 2.5 mm spacing, six irrigation holes, and a cooling chamber filled with NaCl solution. The tip does not embed any mini electrodes. Proximal to the tip, the diameter expands conically to the shaft diameter. The existence of the force sensing spring between the tip electrode and the distal ring electrode in the interior of the catheter [60] was assumed to be negligible with respect to the spread of the electrical field outside the catheter. Therefore, the interior of the catheter shaft was filled with insulating material as well.

A transseptal sheath was implemented on the model of the 8.5 F Agilis™ NxT steerable introducer (Abbott, Chicago, IL, USA) as depicted in Fig. 7.1 (e).

Detailed measures of the implemented catheter and sheath geometries are shown in Fig. 7.1.

The respective catheter was embedded in a 140 mm × 140 mm × 140 mm box filled with either blood or NaCl solution as displayed in Fig. 7.2 (a) for all simulation setups. Geometry definition and tetrahedral meshing was done with Gmsh (version 4.5.6) [64]. Mesh resolution was adapted to the size of local structures being the highest at the IntellaNav MiFi™ OI mini electrodes and the lowest at the outer boundary of the surrounding box. The meshes were comprised of 2.5 million to 5 million tetrahedral elements.

Standardized NaCl Solutions

Either catheter was placed in the surrounding box filled with NaCl solution of eight different molar concentrations starting from 0.02 $\frac{\text{mol}}{\text{l}}$ in steps of 0.01 $\frac{\text{mol}}{\text{l}}$ up to 0.09 $\frac{\text{mol}}{\text{l}}$.

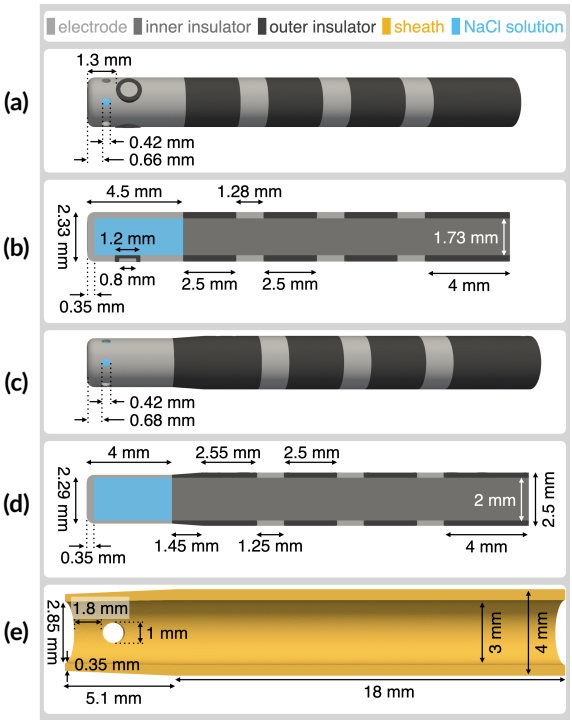

Figure 7.1: Geometrical models of LI-enabled radio frequency ablation catheters and a transseptal sheath. (a) 3D model of the IntellaNav MiFi™ OI. (b) Cross-section of the IntellaNav MiFi™ OI. (c) 3D model of the IntellaNav Stablepoint™. (d) Cross-section of the IntellaNav Stablepoint™. (e) Cross-section of a transseptal sheath including one out of two irrigation holes. Reprinted with permission from [54].

Transseptal Steerable Sheath

Within a surrounding box filled with blood, either catheter was withdrawn into the transseptal sheath model with the distance d_{Sh} describing the distance between the catheter tip and the distal edge of the sheath (compare Fig. 7.2 (d)). Negative distances describe the withdrawal of the catheter into the sheath. d_{Sh} was varied from −2 mm in steps of 0.5 mm up to 19.5 mm.

Tissue Setups

Either catheter was placed in the surrounding box filled with blood. A square patch of tissue measuring 110 mm × 110 mm × 2.5 mm was placed below the catheter resembling a piece of atrial myocardial tissue of typical wall thickness [65] (compare Fig. 7.2 (a)). The distance d_{T} between the catheter and the tissue was varied from −2 mm to 10 mm in steps of 0.5 mm (compare Fig. 7.2 (b)). Negative distances represented an immersion of the catheter into the tissue. Mechanical interaction was not modeled. Instead, the catheter simply displaced the tissue.

In a second step, the angle α_T between the catheter and the tissue was varied from 0° to 180° in steps of 15°. For $90° < \alpha_T \leq 180°$, one of the mini electrodes pointed directly towards the tissue. For $0° \leq \alpha_T < 90°$, the two remaining electrodes were pointed towards — but not directly towards — the tissue (compare Fig. 7.2 (b)). The pivot was located at the intersection of the catheter's distal plane and the outer wall of the catheter shaft at the left and the right, respectively. The experiment was conducted for five different distances between catheter and tissue $d_T \in \{0.0\,\text{mm}, 0.5\,\text{mm}, 1.0\,\text{mm}, 2.0\,\text{mm}, 4.0\,\text{mm}\}$.

Transmural Lesion

The general tissue setup as described above was complemented by a central line of scar tissue of width $w_{Sc} \in \{3\,\text{mm}, 6\,\text{mm}\}$ (compare Fig. 7.2 (a)) representing ablated tissue from a previous procedure or natively developed myocardial scar. For two different distances between catheter and tissue ($d_T = 0\,\text{mm}$ and $d_T = 1\,\text{mm}$), either catheter was moved perpendicularly to the line of scar starting at a distance to the center of the line of scar of $d_{Sc} = -10\,\text{mm}$, crossing the line of scar for $d_{Sc} = 0\,\text{mm}$ up to a distance of $d_{Sc} = 10\,\text{mm}$ at a default step size of 1 mm and a decreased step size of 0.5 mm for $|d_{Sc}| < 2\,\text{mm}$.

Pulmonary Vein

The insertion of either catheter into a PV was simulated by extending the general tissue setup by a perpendicular tube filled with blood (compare Fig. 7.2 (c)). For a PV wall thickness $th_{PV} = 2\,\text{mm}$, four different inner PV radii $r_{PV} \in \{2\,\text{mm}, 3\,\text{mm}, 4\,\text{mm}, 6\,\text{mm}\}$ were implemented. For $r_{PV} = 6\,\text{mm}$, additional PV wall thicknesses of $th_{PV} \in \{1\,\text{mm}, 3\,\text{mm}, 4\,\text{mm}\}$ were modeled. Either catheter was inserted into the PV quantified by the distance d_T to the surface of the tissue. Negative distances represent states with the respective catheter being inside the PV while positive distances represent states of catheter elevation above the tissue. d_T was varied from −20 mm (full immersion) to 10 mm (full extraction) in steps of 1 mm.

Irrigation

Catheter irrigation was modeled by placing a sphere of physiological NaCl solution at each center of the irrigation holes displacing all encircled blood elements (compare Fig. 7.2 (e)). The radius r_{NaCl} of the NaCl spheres was varied from 0 mm to 2 mm in steps of 0.05 mm.

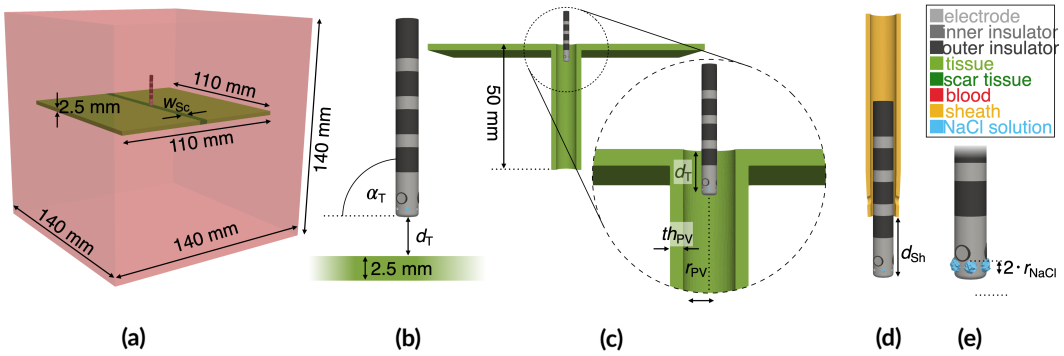

Figure 7.2: Simulation setups. All setups are depicted at the example of the IntellaNav MiFi™ OI and were equally conducted with the IntellaNav Stablepoint™. (a) Tissue patch with line of scar within the surrounding blood box. (b) Variation of distance and angle between catheter and tissue. (c) Insertion of the catheter into the PV. (d) Insertion of the catheter into the transseptal sheath. (e) Irrigation with NaCl solution. Reprinted with permission from [54].

7.2.2 *In Silico* — Material Properties

The tetrahedral elements of the geometrical meshes were assigned conductivity values characteristic for the respective material at 14.5 kHz as summarized in Table 7.1. Due to the significant dependency of conductivities on the temperature, the latter had to be regarded for.

The *in vitro* setups with NaCl solutions of different concentrations were conducted at different temperatures and compared to *in silico* experiments based on conductivities published by Gabriel et al. [55], which lack an explicit statement about temperature. Comparing to the conductivity of 0.5 % NaCl solution given for 20 °C [17] suggests that Gabriel et al. measured at a slightly higher temperature T_{Gab} (compare Table 7.1). With a temperature coefficient of approximately $2.1\,\frac{\%}{\mathrm{C}}$ [66] and the reference values from [17], Gabriel et al. most likely measured NaCl solutions significantly below body temperature as opposed to their measurements of biological tissue. Since the data set [55] was consistent in itself, the exact temperature was deemed insignificant for the validation setups with NaCl solutions of different concentrations.

All other *in silico* experiments were parameterized with conductivities given for blood, myocardial tissue, and scar tissue at body temperature as well as physiological 0.9 % NaCl solution for catheter irrigation at an approximate lab temperature of 20 °C as listed in Table 7.1. Due to the lack of an explicit reference for the conductivity of physiological 0.9 % NaCl solution, the latter was linearly interpolated from the conductivities of 0.5 % and 1 % NaCl solution at 20 °C [17] as listed in Table 7.1.

Table 7.1: Conductivities of relevant materials at 14.5 kHz. BT: body temperature; T_{Gab}: measurement temperature in Gabriel et al. [55]. Reprinted with permission from [54].

Material	Conductivity σ (S/m)	Temperature (°C)	Reference
metallic electrode	$400,000$		[67]
insulator	10^{-7}		
sheath	10^{-7}		
blood	0.700	BT	[52][68]
myocardial tissue	0.164	BT	[52][68]
connective tissue (scar)	0.387	BT	[52][68]
NaCl 0.020 $\frac{\text{mol}}{\text{l}}$ (0.12 %)	0.220	T_{Gab}	[55]
NaCl 0.030 $\frac{\text{mol}}{\text{l}}$ (0.18 %)	0.330	T_{Gab}	[55]
NaCl 0.040 $\frac{\text{mol}}{\text{l}}$ (0.23 %)	0.430	T_{Gab}	[55]
NaCl 0.050 $\frac{\text{mol}}{\text{l}}$ (0.29 %)	0.530	T_{Gab}	[55]
NaCl 0.060 $\frac{\text{mol}}{\text{l}}$ (0.35 %)	0.620	T_{Gab}	[55]
NaCl 0.070 $\frac{\text{mol}}{\text{l}}$ (0.41 %)	0.720	T_{Gab}	[55]
NaCl 0.080 $\frac{\text{mol}}{\text{l}}$ (0.47 %)	0.800	T_{Gab}	[55]
NaCl 0.086 $\frac{\text{mol}}{\text{l}}$ (0.50 %)	0.820	20	[17]
NaCl 0.090 $\frac{\text{mol}}{\text{l}}$ (0.53 %)	0.880	T_{Gab}	[55]
NaCl 0.154 $\frac{\text{mol}}{\text{l}}$ (0.90 %)	1.444	20	
NaCl 0.171 $\frac{\text{mol}}{\text{l}}$ (1.00 %)	1.600	20	[17]

7.2.3 *In Silico* — Impedance Forward Simulation

The spread of the electrical field was simulated with the software EIDORS v3.10 [69] and MATLAB R2021a (The MathWorks, Inc., Natick, MA, USA). In short, EIDORS solves the Poisson equation with a finite element model F. The injection currents are given as boundary conditions. The current density and the potential field are the solution. The voltage v between two electrodes is extracted as the potential difference and is dependent on the given conductivities $\boldsymbol{\sigma}$ at the elements of the model and the stimulation pattern $\boldsymbol{q}$ of the electrode model with $v = F(\boldsymbol{\sigma}, \boldsymbol{q})$ [69].

Stimulation and measurement circuits were defined according to the clinical system: A four-terminal circuit with current injection between the distal tip electrode and the proximal ring electrode was combined with measurements between the mini electrodes and the distal ring electrode for the IntellaNav MiFi™ OI [13]. The three voltage measurements resulting from either mini electrode to the distal ring electrode were reduced to their maximum value following the clinical system. The IntellaNav Stablepoint™ was set up as a three-terminal circuit with current injection between the distal tip electrode and the proximal ring electrode and voltage measurement between the distal tip electrode and the distal ring electrode.

An alternating current of $5\,\mu$A peak-to-peak amplitude at 14.5 kHz was modeled. The complete electrode model was used [70]. The resulting voltage amplitude $|v|$ was then divided by the amplitude of the injected current to obtain LI as the magnitude of the impedance.

7.2.4 *In Vitro* Setup

All measurements were conducted with the Rhythmia HDx system (Boston Scientific, Malborough, MA, USA), the IntellaNav MiFi™ OI, and the IntellaNav Stablepoint™. To validate the simulation framework, NaCl solutions of different concentrations and known conductivity σ were prepared. The molar mass as given in [55] starting from 0.02 $\frac{\text{mol}}{\text{l}}$ up to 0.09 $\frac{\text{mol}}{\text{l}}$ in steps of 0.01 $\frac{\text{mol}}{\text{l}}$ was converted to weight percentages. The respective amount of NaCl was weighed out with a scale of 10^{-3} g resolution and 10^{-3} g precision and dissolved in 250 ml of de-ionized water. For all concentrations, the NaCl dissolved completely and formed an aqueous solution. A thermometer of 0.1 °C resolution was used to keep track of the solution's temperature. The LI was measured with both catheters in each solution at 7 to 13 different temperatures between 18.2 °C and 38.8 °C. For comparability, the LI at three different temperatures — namely 21 °C, 25 °C, and 36 °C — was interpolated and compared to the simulated results for the respective NaCl solutions.

Additionally, the behavior of LI with tissue contact was measured *in vitro*. A tissue phantom composed of 100 ml de-ionized water, 3 g agar-agar, and 0.0499 g NaCl [71] was prepared. The expected conductivity of 0.16 $\frac{\text{S}}{\text{m}}$ at 25 °C matched the conductivity of cardiac tissue at 14.5 kHz well. Since *in vitro* measurements were taken at 20.5 °C in this work, the actual conductivity might have deviated slightly due to the difference in temperature. Typical temperature coefficients reported for similar materials justified to neglect deviations caused by the described change in temperature [66][72]. Additionally, a piece of smooth left atrial porcine tissue was used. The tissue phantom and the tissue sample were mounted at an elevated ring in order not to disturb measurements by the mount in 0.35 % NaCl solution. Either catheter was positioned at the tissue phantom and the tissue sample in orthogonal and parallel orientation.

The effect of catheter irrigation with physiological NaCl solution on LI was investigated by increasing the flow rate of the HAT 500® irrigation pump (Osypka AG, Rheinfelden, Germany) from 0 $\frac{\text{ml}}{\text{min}}$ to 2 $\frac{\text{ml}}{\text{min}}$ and 17 $\frac{\text{ml}}{\text{min}}$ in a 250 ml bath of 0.35 % NaCl solution. A flow rate of 2 $\frac{\text{ml}}{\text{min}}$ is clinically applied in standby mode while the flow rate is typically adjusted to 17 $\frac{\text{ml}}{\text{min}}$ during ablation. The bath model did not include circulation.

7.2.5 *In Human* Setup

Clinical measurements complemented the *in silico* analysis of catheter sheath interaction and its effect on the LI. Either catheter was located in the left atrium passing the inter-atrial septum via the transseptal sheath, namely the Agilis™ NxT steerable introducer. An X-ray scan verified that the proximal ring electrode was outside of the sheath. Starting from a central position in the left atrial bloodpool without endocardial contact, the catheter was gradually pulled back into the sheath at constant speed while recording the LI. Clinical LI was

represented by its moving average calculated with a sliding window of 1.5 s width as provided by the electroanatomical mapping system. All *in human* measurements were approved by the local ethics committee and were conducted in accordance with the Declaration of Helsinki. Written informed consent was obtained from all patients.

7.3 Results

7.3.1 Aqueous NaCl Solutions

Fig. 7.3 presents LI values measured *in vitro* in aqueous NaCl solutions prepared according to Table 7.1 at 21 °C, 25 °C, and 36 °C along with simulated LI values for *in silico* setups of the corresponding molar concentrations. Higher temperatures yielded lower LI values for constant NaCl concentration. *In vitro* and *in silico* experiments followed the same hyperbolic-like trend with decreasing LI values for increasing conductivity.

Simulated LI values predominantly fell between the corresponding *in vitro* measurements at 21 °C and 25 °C for both catheters with a median deviation of −2.7 Ω and −2.8 Ω from the measurements at 21 °C for the IntellaNav MiFi™ OI and the IntellaNav Stablepoint™, respectively. A negative deviation is in line with the assumption of $20\,^{\circ}\mathrm{C} < T_{\mathrm{Gab}} \ll 36\,^{\circ}\mathrm{C}$ as stated in Section 7.2.4. With the *in silico* and *in vitro* traces matching both in morphology and absolute values, the simulation environment was considered valid to a high degree of detail across the relevant range of conductivities for further experiments.

NaCl concentrations of $c_{\mathrm{NaCl}} = 0.06\,\frac{\mathrm{mol}}{\mathrm{l}}$ and $c_{\mathrm{NaCl}} = 0.07\,\frac{\mathrm{mol}}{\mathrm{l}}$ equaling mass concentrations of 0.35 % and 0.41 % were found to yield an LI comparable to human blood. For a concentration of $c_{\mathrm{NaCl}} = 0.06\,\frac{\mathrm{mol}}{\mathrm{l}}$, the *in silico* setups yielded an LI of 98.3 Ω and 154.5 Ω compared to *in vitro* measurements at 21 °C of 101.9 Ω and 156.2 Ω for the IntellaNav MiFi™ OI and IntellaNav Stablepoint™, respectively, which compared well to the clinically observed ranges of bloodpool LI.

The simulated bloodpool LI for a blood conductivity $\sigma = 0.7\,\frac{\mathrm{S}}{\mathrm{m}}$ [68] as given in Table 7.1 and later on used in all other *in silico* setups was at the lower bound of clinically observed values with 87.1 Ω for the IntellaNav MiFi™ OI and 138.9 Ω for the IntellaNav Stablepoint™.

Linear regression of LI measurements with both catheters deduced a perfect linear relationship ($R^2 < 10^{-4}$) between LI values measured with the IntellaNav MiFi™ OI (LI_{MiFi}) and the IntellaNav Stablepoint™ (LI_{StPt}) for *in silico* and *in vitro* experiments. Measurements in an extended set of 25 NaCl solutions of concentrations between 0.15 % and 2.00 % yielded the following linear relationship:

$$LI_{\mathrm{StPt}} = 1.42 \cdot LI_{\mathrm{MiFi}} + 8.7\,\Omega \tag{7.1}$$

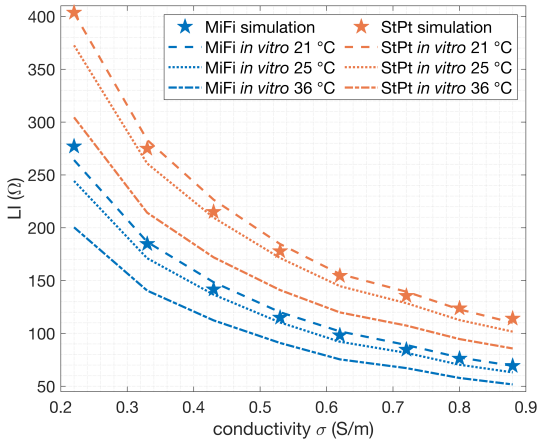

Figure 7.3: *In vitro* LI measurements of several NaCl molar solutions compared with simulated LI values. Broken lines correspond to measurements at 21 °C, 25 °C, and 36 °C, whereas star marks refer to simulations. IntellaNav MiFi™ OI and IntellaNav Stablepoint™ values are shown in blue and orange, respectively. Reprinted with permission from [54].

7.3.2 Transseptal Steerable Sheath

Fig. 7.4 presents simulated and exemplary clinical LI traces characteristic for the withdrawal of the IntellaNav MiFi™ OI (a) and the IntellaNav Stablepoint™ (b) into the transseptal sheath.

Starting at a simulated bloodpool of 87 Ω and 139 Ω, the *in silico* LI measured with the IntellaNav MiFi™ OI and the IntellaNav Stablepoint™ first increased by more than 2 Ω for the distal edge of the sheath being located between the proximal and the 2nd to proximal ring electrode. The steep increase of LI began upon the coverage of the distal ring electrode by the sheath. For full sheath coverage, the LI increased up to 1353 Ω and 2200 Ω for the IntellaNav MiFi™ OI and the IntellaNav Stablepoint™, respectively. For the distal edge of the sheath being located between the distal ring electrode and the tip electrode, an interim decrease in steepness formed a plateau especially pronounced for the IntellaNav Stablepoint™.

Both simulated traces compared well with the clinically measured traces.

7.3.3 Catheter Tissue Interaction

Catheter Distance and Orientation

Again starting from a bloodpool LI of 87 Ω and 139 Ω for the IntellaNav MiFi™ OI and the IntellaNav Stablepoint™, respectively, the LI increased with decreasing distance to the tissue surface for perpendicular catheter positions ($\alpha_T = 90°$) as shown in Fig. 7.5. At a distance

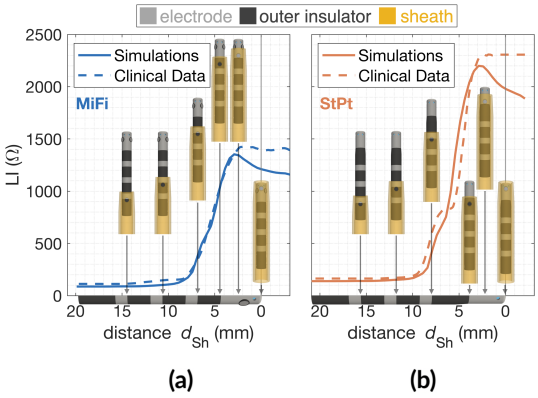

Figure 7.4: Withdrawal of (a) IntellaNav MiFi™ OI and (b) IntellaNav Stablepoint™ into a transseptal sheath. *In silico* LI is represented by solid lines while clinical LI is represented by dashed lines. Sheath positions are indicated on the horizontal axes. Reprinted with permission from [54].

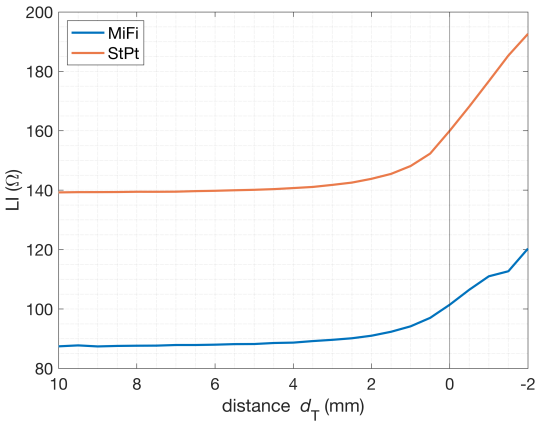

Figure 7.5: Dependency of the LI on the distance to myocardial tissue for IntellaNav MiFi™ OI in blue and IntellaNav Stablepoint™ in orange. Reprinted with permission from [54].

$d_T = 3.5\,\text{mm}$ and $d_T = 2.5\,\text{mm}$, the LI exceeded the bloodpool LI by more than 2 % for the IntellaNav MiFi™ OI and IntellaNav Stablepoint™, respectively. At a distance $d_T = 0\,\text{mm}$, the LI exceeded the bloodpool LI by 16.0 % and 14.9 % for the IntellaNav MiFi™ OI and IntellaNav Stablepoint™, respectively. The closer the catheter approached the tissue, the steeper the LI increased. For negative distances d_T, i.e. the catheter entering the tissue, the increase in LI per distance was approximately constant. For the IntellaNav MiFi™ OI, a small plateau in LI formed between $d_T = -1.0\,\text{mm}$ and $d_T = -1.5\,\text{mm}$.

Fig. 7.6 presents the simulated LI values for changing angles α_T between the catheter and the tissue for selected distances. For both catheters and all distances, the traces were w-shaped. Starting from a perpendicular position and approaching a parallel position, LI first dropped and then increased again. The LI for parallel catheter orientation at a distance $d_T = 0\,\text{mm}$ exceeded the LI for perpendicular catheter positions by $14.0\,\Omega$ ($\alpha_T = 0°$) and $12.9\,\Omega$ ($\alpha_T = 180°$) for the IntellaNav MiFi™ OI and by $9.4\,\Omega$ for the IntellaNav Stablepoint™.

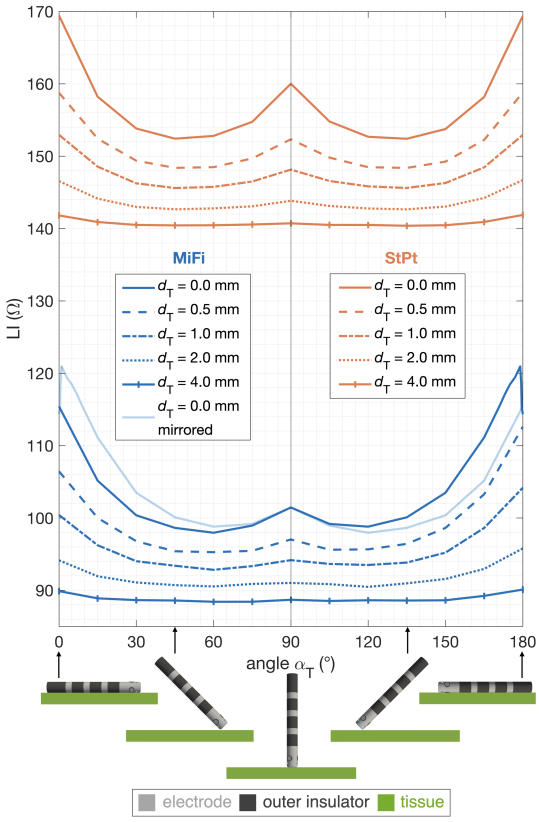

Figure 7.6: Dependency of the LI on the angle α_T between catheter and myocardial tissue for IntellaNav MiFi™ OI in blue and IntellaNav Stablepoint™ in orange for different distances d_T between catheter and tissue. Reprinted with permission from [54].

While the traces were symmetric to $\alpha_T = 90°$ for the IntellaNav Stablepoint™, the LI depended on the orientation of the mini electrodes for the IntellaNav MiFi™ OI as indicated by the mirrored trace in Fig. 7.6. Catheter orientations with one of the measuring mini electrodes being directed to the tissue ($(90° < \alpha_T \leq 180°)$) exceeded those LI values of the same distance and angle for which none of the mini electrodes pointed directly towards the tissue ($0° \leq \alpha_T < 90°$).

In vitro measurements with the respective catheter touching a tissue phantom or a tissue sample perpendicularly and in parallel yielded comparable differences between the parallel and orthogonal position. The LI for the parallel position exceeded the LI of the perpendicular position by approximately 11 Ω and 10 Ω for the IntellaNav MiFi™ OI and IntellaNav Stablepoint™, respectively.

Transmural Lesion

Due to the higher conductivity of connective tissue compared to healthy myocardium, the LI typically drops in the vicinity of myocardial lesions. In these setups, the dependency of the

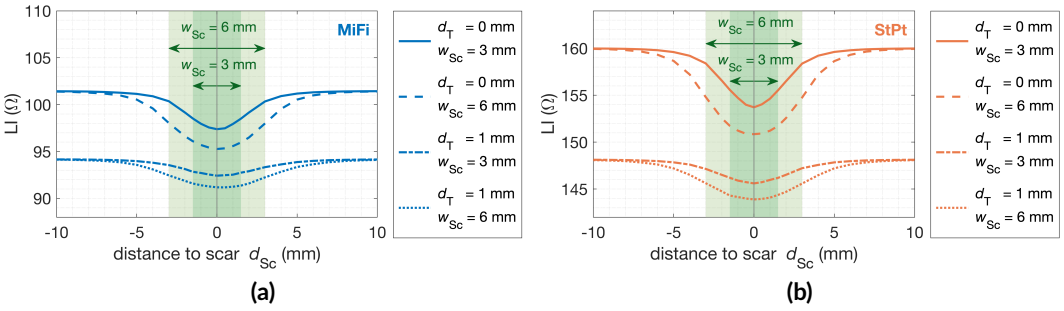

Figure 7.7: Dependency of the LI on the horizontal distance d_{Sc} to a linear scar embedded in a patch of tissue for the IntellaNav MiFi™ OI in (a) and the IntellaNav Stablepoint™ in (b). Each catheter hovered the tissue at two vertical distances $d_T = 0\,\text{mm}$ and $d_T = 1\,\text{mm}$ for two different scar widths $w_{Sc} = 3\,\text{mm}$ and $w_{Sc} = 6\,\text{mm}$. Reprinted with permission from [54].

LI on the extent of the scar and the relative position of the catheter was investigated. Fig. 7.7 shows LI traces for the virtual catheter passing linear lesions of 3 mm and 6 mm width. For direct tissue contact ($d_T = 0\,\text{mm}$), the absolute drop was larger for the IntellaNav Stablepoint™ due to the higher baseline LI for either lesion width. The percentage drop based on the LI at maximum distance to the lesion, however, was similar with 3.8 % and 6.0 % for lesion widths of 3 mm and 6 mm for the IntellaNav MiFi™ OI and a percentage drop of 3.9 % and 5.7 % for the IntellaNav Stablepoint™. Increasing the vertical distance d_T between the catheter and the myocardial tissue by 1 mm caused a larger drop in the baseline LI than either of the scars for both catheters.

Fig. 7.8 shows the potential field (a) and the current density (b) for the setup with a scar width $w_{Sc} = 3\,\text{mm}$ and direct tissue contact. With a similarity to an electrical dipole field, the current spreads between the injecting electrodes. The current density in Fig. 7.8 (b) adumbrates the edges of the tissue directly underneath the distal tip electrode. Higher current densities in the central line of scar compared to the surrounding tissue were caused by the higher conductivity of scar tissue.

7.3.4 Insertion into a Pulmonary Vein

Fig. 7.9 shows characteristic LI traces for progressive introduction of an ablation catheter into the PV. Fig. 7.9 (a) displays simulated LI values for the IntellaNav MiFi™ OI. The LI increased from 87 Ω in the simulated bloodpool up to peak values between 93 Ω and 176 Ω depending on the radius r_{PV} and the thickness th_{PV} of the PV. According LI traces for the IntellaNav Stablepoint™ are presented in Fig. 7.9 (b). Starting from a simulated bloodpool LI of 139 Ω, the LI increased up to 145 Ω to 240 Ω depending on r_{PV} and th_{PV}.

The radius r_{PV} was found to be a strong determinant of the maximum LI reached upon insertion of the catheter into the PV. While the narrowest simulated PV with $r_{PV} = 2\,\text{mm}$

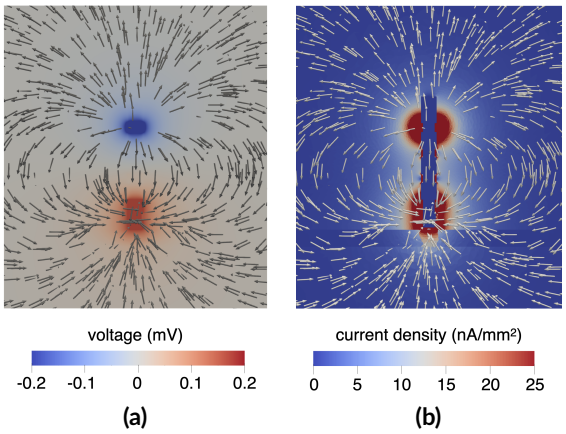

Figure 7.8: Cross section of a setup with a scar of 3 mm width embedded in a patch of myocardial tissue surrounded by blood. The potential field (a) and current density (b) characterize the electrical field. Arrows mark the direction of current flow. Reprinted with permission from [54].

yielded a maximum LI of 176 Ω with the IntellaNav MiFi™ OI and 240 Ω with the IntellaNav Stablepoint™, an increase of the radius by 1 mm resulted in a maximum LI of only 127 Ω and 186 Ω, respectively.

Peak values for all parameterizations of the PV corresponded with the insertion of the tip of the ablation catheter into the PV in the *in silico* experiments. The slight decrease for deeper insertions was related to the passing of the surrounding tissue plate that additionally elevated the LI at its maximum.

The thickness of the vein tissue took additional influence on the absolute LI value, as shown for a vein radius $r_{PV} = 6\,\text{mm}$ in Fig. 7.9.

7.3.5 NaCl Solution Irrigation

Fig. 7.10 displays simulated LI values for flushing of the catheters with physiological NaCl solution exiting the cooling lumen at the irrigation holes. Varying the bubble radius r_{NaCl} from 0 to 2 mm mimicked changing the irrigation flow rate. The LI remained indifferent to NaCl bubbles up to a radius $r_{NaCl} = 0.7\,\text{mm}$ and $r_{NaCl} = 0.55\,\text{mm}$ with less than 1 % change compared to the *in silico* measurement in plain bloodpool of 87 Ω and 139 Ω for the IntellaNav MiFi™ OI and the the IntellaNav Stablepoint™, respectively. For the IntellaNav MiFi™ OI, the LI then slightly increased reaching a maximum elevation of 1.4 Ω above the bloodpool for $r_{NaCl} = 0.8\,\text{mm}$ when the NaCl bubbles barely reached the mini electrodes' distal edges. Afterwards, LI values decreased with increasing r_{NaCl} down to 76.4 Ω for $r_{NaCl} = 2\,\text{mm}$. The LI decreased monotonously for the IntellaNav Stablepoint™ down to 116.6 Ω for $r_{NaCl} = 2\,\text{mm}$.

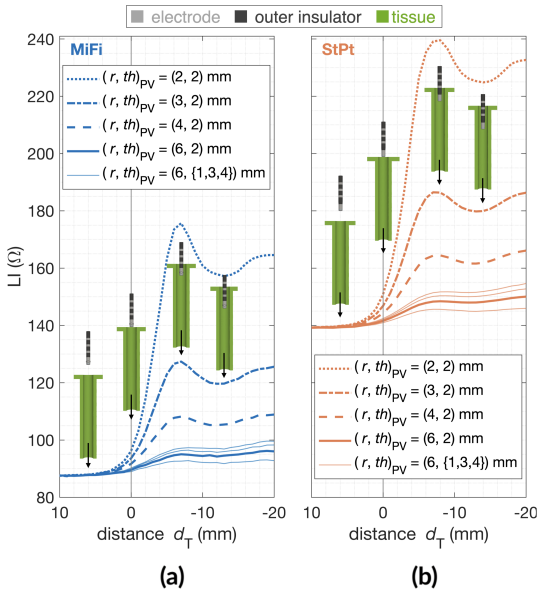

Figure 7.9: LI traces upon progressive introduction of (a) IntellaNav MiFi™ OI in blue and (b) IntellaNav Stablepoint™ in orange into a PV. The horizontal axis annotates the distance between the tip of the ablation catheter and the edge of the tissue. Negative distances correspond to positions inside the PV. Reprinted with permission from [54].

Fig. 7.10 (a) and (b) display *in vitro* traces of LI for onset and offset of irrigation at different flow rates. *In vitro* measurements at a flow rate of 2 $\frac{\text{ml}}{\text{min}}$ revealed an instantaneous drop of 0.6 Ω and 1 Ω and oscillations in LI of 0.6 Ω and 1 Ω peak-to-peak amplitude tracing back to the cylinders of the irrigation wheel compressing the irrigation tube for the IntellaNav MiFi™ OI and the IntellaNav Stablepoint™, respectively. For the IntellaNav Stablepoint™, LI dropped abruptly by 2.5 Ω upon the onset of irrigation at 17 $\frac{\text{ml}}{\text{min}}$. The gradual decrease of LI is the result of a small bath volume mixing with the irrigation fluid of higher conductivity.

7.4 Discussion

In summary, we presented an *in silico* environment that resembled *in human* and *in vitro* LI measurements to a high degree of detail and allowed for quantification of distinct influences on the measurement with known ground truth.

7.4.1 Aqueous NaCl Solutions

Model validation with standardized aqueous NaCl solutions of known conductivity was successful and proved the suitability of the simulation environment. NaCl solutions can be

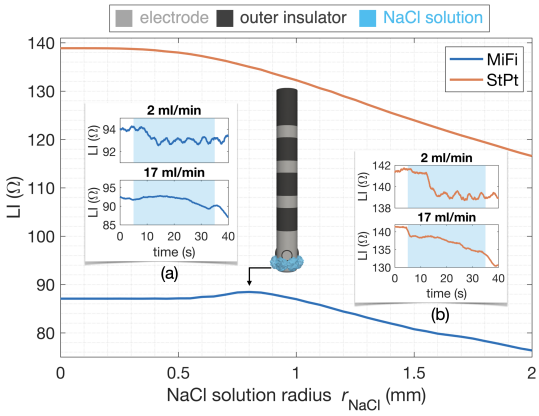

Figure 7.10: *In silico* LI for different irrigation radii of NaCl solution for the IntellaNav MiFi™ OI in blue and the IntellaNav Stablepoint™ in orange. Subpanels (a) and (b) report *in vitro* measurements for the onset of irrigation flow rates of 2 $\frac{\text{ml}}{\text{min}}$ and 17 $\frac{\text{ml}}{\text{min}}$. Irrigation times are shaded in blue. Reprinted with permission from [54].

assumed to be of mostly resistive character at a measurement frequency of 14.5 kHz. Thus, the hyperbolic-like relationship between conductivity and LI can be explained as impedance reduces to resistance in this setup and resistance is reciprocally related to conductivity.

For *in vitro* experiments, aqueous NaCl solutions at 0.35 % to 0.4 % mass concentration at 21 °C were shown to serve well as dielectric equivalent of human blood at body temperature for a measurement frequency of 14.5 kHz.

A perfectly linear relationship between LI measurements with the IntellaNav MiFi™ OI and the IntellaNav Stablepoint™ as described by Eq. 7.1 is of great clinical value. Translation of findings and reference values between both catheters can extrapolate clinical trials to the respective other device and reduce efforts. Measurements with different instances of the catheters resulted in minor deviations of the linear coefficients and could potentially be caused by slight manufacturing differences or by the fact that all *in vitro* catheters had been used for radio frequency ablation before.

7.4.2 Transseptal Steerable Sheath

In silico experiments revealed that LI started to increase notably as soon as the sheath passed the proximal ring electrode. LI measurements for both, substrate and lesion characterization in clinical practice, should therefore always assure full withdrawal of the catheter out of the sheath in order to prevent confounding influences on the measured LI.

7.4.3 Catheter Tissue Interaction

The elevation of LI in tissue contact above the bloodpool LI ranged from 14 Ω for 0 mm distance to the tissue, i.e. 0 g so-called "contact force", to 33 Ω for −2 mm distance to the tissue and compared well to clinically observed mean ranges between 16 Ω and 20 Ω [73] for the IntellaNav MiFi™ OI. The simulated upper bound for an immersion depth of 2 mm thus likely overestimates the LI for clinical mean contact force applications due to the disregard of realistic tissue deformation.

Sulkin et al. had performed detailed *in vitro* experiments on catheter tissue interaction with the IntellaNav MiFi™ OI and found a nonlinear monotonic increase of LI as the catheter approximated the tissue at an angle of 90° [13]. The *in silico* results generated in this work matched the shape of the curve very well but yielded scaled absolute values and slopes presumably due to differences in the underlying conductivity of tissue and blood. The right ventricular tissue used by Sulkin et al. was presumably thicker than the atrial tissue modeled with a thickness of only 2.5 mm in this work and could explain the higher absolute values and slopes in their study. Additionally, the natural variability of the conductivity of tissue samples causes a spread of measured LIs [13] that could account for the scaled results. The specific conductivities chosen in this work are only one sample of the natural spread of human myocardial conductivity.

Changing the angle between catheter and tissue resulted in higher LIs for more parallel compared to orthogonal catheter orientation for distances $d_T > -2$ mm both in the work by Sulkin et al. and the *in silico* experiments in this work. Garrott et al. [60] observed a mean LI difference of 13 Ω between perpendicular and parallel catheter orientation of the IntellaNav StPt™, which is well in line with the *in silico* experiments presented here.

In silico experiments with the IntellaNav MiFi™ OI presented a small plateau for an immersion into atrial tissue by 1.0 mm to 1.5 mm as well as an abrupt decrease in LI for an angle $\alpha_T = 180\,^\circ$ that were not in line with the trend of the respective adjacent distances and angles. Presumably, the close interaction between the measuring mini electrode and the tissue caused both observations.

Clinical studies report different ranges of LI values for healthy and scar tissue, e.g. 109 Ω ± 15 Ω and 104 Ω ± 12 Ω [48], 111 Ω ± 14 Ω and 92 Ω ± 16 Ω [49], and 132 Ω ± 12 Ω [50], respectively, for the IntellaNav MiFi™ OI. The variability in range may be explained by different operators and differences in typically applied contact force which remains uncontrolled for the IntellaNav MiFi™ OI. In line with previously published clinical observations, scar tissue presented lower LI compared to healthy myocardium due to the increase in extracellular space and the resulting increase in conductivity in the *in silico* model as well. Slightly lower values for both healthy and scar tissue in the *in silico* study as depicted in Fig. 7.7 in comparison with the clinical observations [48][49][50] could either be caused by the choice of conductivies in the *in silico* model or from a lower contact force. While the *in silico* model operates at an equivalent of 0 g so-called "contact force" for the experiments on

scar tissue, typical clinical values range from 5 g to 20 g. The larger the lesion area within the footprint of the catheter, the lower the LI dropped. The results presented in Fig. 7.7 emphasize the importance of direct tissue contact and controlled contact force for quantitative applications of LI measurements. Drops in baseline LI caused by only 1 mm distance to the endocardial surface exceeded LI drops caused by transmural lesions. Since the exact values depend on the scar and tissue conductivity provided to the model and scar conductivity was approximated by the conductivity of connective tissue, a validation of the conductivity of atrial scar tissue would strengthen the finding but was out of the scope of this work.

Myocardial tissue was modeled as homogeneous, isotropic block. The effect of fiber direction and three-dimensional atrial structures remains unlit within the scope of this work. Future studies will have to shed light on more detailed models of the myocardium.

7.4.4 Insertion into a Pulmonary Vein

In silico experiments demonstrated the strong dependency of the LI measured inside a PV on the radius of the vein. Vein tissue was modeled indifferently from myocardial tissue for simplicity although the substrates clearly differ histologically and can be assumed to further alter the LI measured in human PVs.

7.4.5 NaCl Solution Irrigation

Both IntellaNav MiFi™ OI and IntellaNav Stablepoint™ come with an open irrigated tip with the purpose of cooling the electrode during ablation delivery. Typically, catheters are flushed with 0.9 % so-called physiological NaCl solution at lab temperature. However, 0.9 % NaCl solution deviates by a factor of approximately 2 from human blood in terms of conductivity (compare Table 7.1). Earlier studies have shown that the irrigation fluid during radio frequency ablation delivery takes influence on lesion formation. Highly conductive irrigation fluids such as physiological NaCl solution attract current flow and thus reduce the current flowing through the target tissue resulting in reduced energy deposition and smaller lesions compared to irrigation with less conductive fluids such as 0.45 % NaCl solution or dextrose water [53][74][75][76]. Similarly, awareness should be drawn to irrigation fluids for LI measurements during ablation delivery and substrate characterization. In particular, two cases have to be distinguished: the effect of constant irrigation flow rates $> 0 \frac{\text{ml}}{\text{min}}$ and the effect of changing flow rates. Constant flow rates mainly relate to the application of LI substrate mapping while a change of flow rate alludes to the use case of radio frequency ablation delivery. In either case, clinical LI is mostly interpreted in differential manner comparing to the bloodpool reference or the LI at the start of the ablation as opposed to absolute values.

With the typical increase of the irrigation flow rate from a default flow of 2 $\frac{\text{ml}}{\text{min}}$ to 17 $\frac{\text{ml}}{\text{min}}$ or 30 $\frac{\text{ml}}{\text{min}}$ during radio frequency power delivery, the amount of irrigation fluid surrounding the catheter tip presumably increases and causes an LI drop by default that is not related to tissue heating as commonly attributed to LI drops during ablation. With the results presented in Fig. 7.10 and the assumption that the irrigation fluid is quickly flushed by circulatory blood flow, the LI drop caused by changes of the irrigation flow rate seem to be mostly negligible seen in the context of typically required minimum LI drops of 12 Ω to 16 Ω during radio frequency power delivery with the IntellaNav MiFi™ OI [47].

For the use case of LI substrate mapping, LI differences of few ohms become of importance. However, a constantly low flow rate of 2 $\frac{\text{ml}}{\text{min}}$ limits the potential for flawing the measurement. Interpreting LI only in differential manner, irrigation will impact the result if the distribution of NaCl close to the catheter tip changes, e.g. due to blood flow. Additionally, the higher conductivity of NaCl solution compared to tissue and blood causes less current to flow through the target of interest.

The *in silico* investigations in this work are clearly limited to the oversimplified spherical geometries of NaCl irrigation fluid at the catheter tip as well as the lack of a clear correlation between spherical radius in the model and clinical irrigation flow rates. Similarly, the *in vitro* setup lacks a model of circulatory blood flow. Including a fluid dynamics model could bring more detailed insights into the influence of irrigation and irrigation changes on the measured LI.

7.4.6 Sensitivity

Slight variations in the catheter dimensions resulted in notable changes of LI especially for the respective measuring electrodes. For quantitative analyses, a detailed geometrical model of the catheter under investigation is therefore of high importance.

In silico experiments in this work demonstrated that selected phenomena of interest such as the presence of scar tissue result in minute changes in LI while recording conditions such as the loss of optimal wall contact cause changes in the same or even higher order of magnitude. In a clinical environment under the presence of measurement noise, the detectable range of changes in LI will further decrease, which emphasizes the necessity of establishing ideal wall contact, amongst other recording conditions under control of the operator.

In clinical setups, the inflation and deflation of the lungs is an additional confounding factor with evident impact on the LI measurement [73] due to the close proximity of the lungs to selected parts of the cardiac chambers. While the conductivity of inflated lungs is reported to be 0.0954 $\frac{\text{S}}{\text{m}}$ at 14.5 kHz, the conductivity increases to 0.247 $\frac{\text{S}}{\text{m}}$ in deflated state [52]. Since the respiratory state of the patient is a known parameter, respiratory oscillations in LI traces could be compensated for.

An estimate of the relative contribution of sample volumes in vicinity to the catheter to the measured LI would be of high interest in order to assess the suitability of catheters and electrode arrangements for impedance measurements. The close proximity of the catheter will take significantly more influence on the measured impedance for LI measurements as compared to generator impedance measurements. Specific examples such as varying the distance between catheter and tissue, scar, and sheath as well as varying the volume of NaCl irrigation fluid were presented in this work. However, a systematic analysis does not only require the variation of the sample volume position but also of its size and conductivity. Future studies should systematically shed light on this aspect in order to further optimize catheter and electrode arrangement for LI measurements.

7.4.7 Conclusion

With this work, we introduced and validated an *in silico* model including highly detailed catheter and sheath geometries in combination with a simplified myocardial geometry to study local electrical impedance measurements with intra-atrial catheters. Clinically relevant scenarios such as catheter-tissue interaction in terms of angle, distance, and substrate, the insertion of the catheter into a PV, the withdrawal into the transseptal sheath, and catheter irrigation were reflected in the model. Forward simulations of the electrical field gave insights in the quantitative effects of isolated and combined changes in parameters on the LI. The presented environment proved to be a highly valuable tool that provides deeper insight into the clinical interpretation of LI and has the potential to support future catheter development.

Chapter 8

Local Electrical Impedance Mapping of the Atria: Conclusions on Substrate Properties and Confounding Factors [1]

8.1 Introduction

Electrical impedance measurements have a long history in medical diagnosis and treatment [77] [56]. Measuring the complex resistive behavior of different tissues provides insight into the tissue characteristics [55]. In clinical electrophysiology, cardiac arrhythmias are treated by ablating the triggering or promoting cells with radiofrequency energy and monitoring the impedance during energy delivery. The generator impedance is typically measured with a two-electrode setup consisting of the intracardiac ablation electrode and a cutaneous dispersive electrode. The transthoracic impedance of the radiofrequency energy delivery pathway serves as a measure for lesion assessment. Although the generator impedance is capable of sensing impedance differences between bloodpool and tissue contact, the local resolution is very limited and flawed by the bulk impedance of the torso [59]. The DirectSense™ technology (Boston Scientific, Marlborough, MA) has recently been introduced to overcome this problem. Novel local impedance (LI) measurement capabilities on ablation catheters with all measuring and injecting electrodes at the catheter itself allow to precisely assess catheter–tissue coupling and are more predictive of lesion formation [13] [47]. The technology takes advantage of acute changes in tissue impedance provoked by radiofrequency ablation [47].

[1] The content of Chapter 8 was published in [73] under the CC-BY license and is in large parts accounted word-for-word in this work. Reprinted, with permission, from [73].

Besides ablation monitoring, impedance measurements can also characterize different types of tissue that differ in their baseline impedance. Experimental analyses of electrical tissue impedance go back to 1996 with extensive characterization of electrical tissue impedance for a wide range of injection frequencies and a diverse set of human tissue samples and other materials [55]. Based on that effect, the DirectSense™ technology can be used as an investigational tool to characterize cardiac tissue by its electrical impedance [50] [49]. Acquiring point-by-point intracardiac impedance data allows for compilation of full-chamber impedance maps. However, tissue characteristics are not the only factor influencing the measurement. Catheter-tissue contact, irrigation fluids, catheter motion, blood flow dynamics, and the proximity to other intracardiac devices have to be taken into account. This study analyzes first experiences with the compilation of meaningful atrial full-chamber LI maps while throwing light on both tissue characteristics as well as confounding factors of LI measurements in the atria.

8.2 Methods

8.2.1 Study Design

This is a retrospective, single-center study which was conducted in accordance with the Declaration of Helsinki. The study was approved by the local ethics committee and all patients provided written informed consent. Patients who received an electrophysiological study and catheter ablation due to atrial fibrillation (AFib) using the RHYTHMIA HDx™ electroanatomical mapping system (Boston Scientific, Malborough, MA, USA) were included into the study. The left atrium (LA) was fully mapped using the IntellaNav MiFi™ OI (Boston Scientific, Malborough, MA, USA) ablation catheter. Magnetic catheter tracking enhanced localization accuracy. After completion of the study, the geometry, mapping data including local activation time (LAT) and bipolar voltage maps, electrograms (EGMs), and impedance data were exported from the system for retrospective analysis. Preprocessing steps for both impedance and EGM recordings were followed by detailed analyses of the impedance data.

8.2.2 Electrogram Processing

QRS Intervals

The timing of all R peaks was extracted from the surface electrocardiogram (ECG). The precordial leads V3 and V4 showed less susceptibility to pacing artifacts from the coronary sinus (CS) catheter than others and were thus selected for R peak detection with the open-

source software *ECGdeli* [34]. RR intervals were determined as the time difference between two subsequent R peaks.

Pacing

The bipolar EGMs recorded in the CS catheter served as a source for the detection of pacing events emerging from the CS catheter. Peaks in the bipolar EGM exceeding an amplitude of 200 mV defined pacing events.

8.2.3 Local Impedance Measurements

The DirectSense™ technology allowed for intra-atrial LI recordings with the IntellaNav MiFi™ OI catheter. An alternating current is injected at 14.5 kHz between the distal tip electrode and the proximal ring electrode to create a local electrical field. The electrical properties of the immediate surroundings impact the formation of the electrical field. The potential difference $\Delta\Phi$ between each of the three mini-electrodes and the distal ring electrode represents a sample measurement of this electrical field that allows to deduce the electrical properties of the immediately surrounding material. The DirectSense™ technology provides the quotient of the potential difference $\Delta\Phi$ in the numerator and the injected current amplitude in the denominator [13] which will be termed LI in the following and carries the physical unit Ω. The LI is recorded with a sampling frequency of 20 Hz.

The raw LI recording LI_{raw} is subject to significant oscillations. Hence, two different approaches for postprocessing were chosen which resulted in the moving average LI_{movAvg} and the upper envelope LI_{upEn}.

Moving Average

Following the clinical data acquisition, a window of 1.5 s duration was centered at each point in time to calculate the moving average LI_{movAvg} [13] [47] in order to smooth out the oscillations in LI_{raw}. The moving average was motivated by the assumption that it is a clinically established and potentially robust representation of the underlying impedance.

Upper Envelope

As a second approach, the upper envelope of LI_{raw} was obtained by determining the local maxima and subsequent interpolation. Expecting the tissue impedance to be higher than the bloodpool impedance led to the assumption that tissue impedance is reflected best by the maximum values. Local maxima were characterized by a minimum peak prominence of

4 Ω and a minimum peak-to-peak distance equaling half of the mean RR interval to account for LI oscillations caused by ventricular contraction. Local maxima were then temporally interpolated by minimizing the change in slope; therefore, the second derivative as calculated with the discrete Laplacian operator was minimized with the least squares approach. The derived signal will be termed LI_{upEn} in the following.

8.2.4 Bloodpool Impedance

The LI of the bloodpool ($LI_{bloodpool}$) is typically seen as a patient specific reference value and defined as the LI value measured in the left atrial bloodpool without tissue contact. Since $LI_{bloodpool}$ varies among patients, it was individually determined by extracting LI sequences according to the following criteria:

- The distance between any IntellaNav MiFi™ OI electrode and the endocardial shell is at least d.
- The oscillatory amplitude in LI_{raw} is smaller than the median oscillatory amplitude of the patient. For simplicity, the oscillatory amplitude was defined as the difference between the maximum and minimum LI_{raw} within a centered moving window of 1 s duration in this context.
- LI_{movAvg} or LI_{upEn}, respectively, $< 180\,\Omega$ in order to exclude sheath artifacts.
- LI_{movAvg} or LI_{upEn}, respectively, does not change by more than 5 Ω/s in order to exclude artifacts.

To account for different atrial sizes, the minimal distance d between any IntellaNav MiFi™ OI electrode and the endocardial shell was decreased starting from 15 mm in steps of 1 mm until a total of at least 10 s of bloodpool acquisitions accumulated.

The 25 % quartile of all extracted measurements defined the reference value $LI_{bloodpool}$. A bloodpool measure was calculated from both LI_{movAvg} and LI_{upEn} resulting in two values per patient.

8.2.5 Exclusion of Artifacts

As opposed to LAT and voltage mapping, LI mapping is not restricted to one acquisition per atrial cycle since the LI as target property is independent from atrial excitation in the first place [78]. Therefore, any acquired LI sample can theoretically be taken into account. However, many confounding factors impede the revelation of tissue characteristics from LI measurements. Measures have to be taken to minimize the impact of undesirable influences on the LI. In particular, LI measurements were excluded from any subsequent analysis if they met one or more of the following conditions:

- **Sheath artifacts**: An overlap of the steerable sheath with electrodes of the IntellaNav MiFi™ OI catheter causes an artificial increase of LI. Since little sheath coverage of the proximal ring may result in slightly elevated LI values similar to acquisitions within the pulmonary veins (PVs), optimal sheath detection is a non-trivial task. The combination of two criteria determined the presence of sheath overlaps: (i) LI_{raw} exceeding $LI_{bloodpool} + 200\,\Omega$; (ii) changes in LI_{raw} exceeding $400\,\frac{\Omega}{s}$. In case of (i), the excluded segment was extended in both directions until LI_{raw} first fell below $LI_{bloodpool} + 50\,\Omega$ again. Each invalid segment was extended by a safety margin of 1 s in both directions. Remaining valid segments shorter than 0.5 s were excluded as well.
- **Loss of wall contact**: Any LI acquisition taken in distances larger than 7 mm to the endocardium was excluded from further processing.
- **Catheter movement**: Fast catheter movements change the influence of irrigation and blood flow on the LI and result in ambiguous assignments to endocardial locations. The moving average of the velocity within windows of 350 ms quantified catheter movement. Average movements faster than $2\,\frac{mm}{s}$ were excluded from further processing to focus on stable catheter positions. Each invalid segment was extended by a safety margin of 1 s in both directions. Remaining valid segments shorter than 0.5 s were excluded as well.
- **Proximity to Orion**: For some patients, the impedance map was recorded while the IntellaMap Orion™ catheter was inside the LA. Metal and insulator components of other catheters such as the Orion can strongly influence the LI recording. Therefore, any LI acquisition taken in less than 5 mm distance to the Orion catheter was excluded from further processing. Each invalid segment was extended by a safety margin of 1 s in both directions. Remaining valid segments shorter than 0.5 s were excluded as well.

In summary, three out of four exclusion criteria were based on catheter positioning while one criterion was based on the LI trace itself.

8.2.6 Quantification of LI Oscillations

Oscillations in LI_{raw} occurred for various reasons. The most dominant oscillation frequency correlated with the ventricular and atrial contraction rate. Therefore, RR intervals served as windows to determine the LI oscillation (LI_{osci}) as the difference between the maximum and the minimum value of LI_{raw} in the respective RR interval. Only RR intervals with full coverage of valid LI measurements were attributed with an LI_{osci}. The median of all attributed LI_{osci} characterized a patient.

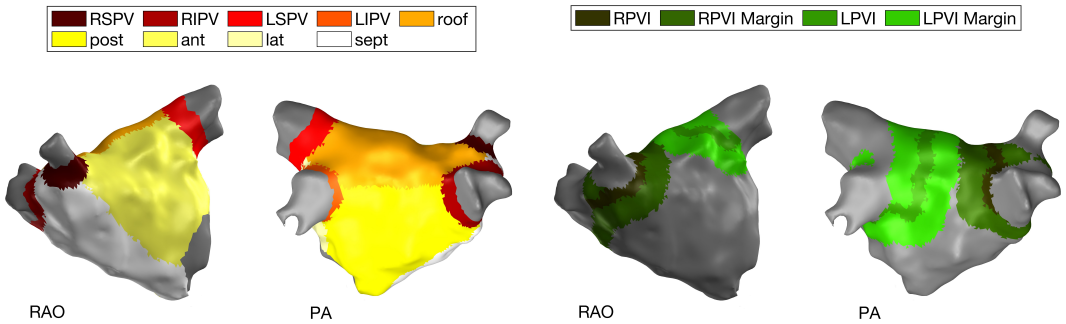

(a) Partitioning by anatomical region.

(b) Partitioning by pulmonary vein isolation (PVI) lesions and margin.

Figure 8.1: Partitioning of the LA by anatomical region (a) and by structural region based on the location of PVI lesions (b). Right-anterior-oblique (RAO) and posterior-anterior (PA) perspective. Reproduced from [73].

8.2.7 Partitioning of the Left Atrium

Anatomical Partitioning

Each LA geometry was clinically annotated with cutouts for the mitral valve and all PVs. The remaining LA was individually subdivided into the septal wall, the lateral wall, the anterior wall, the posterior wall, the inferior wall, and the PV ostia as color-coded in Fig. 8.1 (a) for an exemplary patient. The full set of the aforementioned regions will be referred to as mapping region. The inner parts of the PVs as removed by cutouts during the electrophysiological study were combined with the PV ostia for the regional comparison of LI recordings. The resulting set of vertices will be termed extended mapping region and includes the entire endocardial shell with the exception of the mitral valve. The mapping region and the extended mapping region underwent the same interpolation process as described below for the purpose of impedance mapping.

Structural Partitioning according to Ipsilateral Pulmonary Vein Isolation

In cases with a history of a previous pulmonary vein isolation (PVI), the spatial position of ipsilateral PVI circles were labeled to assess the capability of LI to distinguish between physiological and pathological or preablated tissue. The location was defined based on the voltage map of the current procedure and — if available — by rigid transformation of the ablation points from the previous procedure into the current coordinate system. For each ipsilateral circle, both the ablation core and a surrounding margin were annotated. The total width of the ablation core was varied from 1 mm to 10 mm in steps of 1 mm during analysis. Each side of the surrounding margin was varied from 1 mm to 20 mm in width. In order

to prevent anatomical influences on the analysis of structural LI changes as expected for recording positions within the PVs, any overlap with an inner PV or a PV ostium as defined in the anatomical partitioning was removed from the structurally partitioned regions. Fig. 8.1 (b) displays an exemplary LA with structural labels for ablation cores and surrounding margins. Comparison to the anatomical labels in Fig. 8.1 (a) shows that the PV ostia and the inner PVs are left without label in the structural partitioning.

Patients presenting for de-novo PVI served as control group. Even though the impedance map was recorded before the patients received PVI, the PVI lines were retrospectively annotated according to the location of the ensuing PVI. Extension of the PVI line to the PVI region as well as the definition of the PVI margins was carried out accordingly.

8.2.8 Impedance Mapping

Any valid impedance acquisition was assigned to the closest vertex of the endocardial surface mesh within the mapping area. If one vertex accumulated more than one LI measurement, the set was represented by the 75% quartile. Subsequent nearest neighbor interpolation with a maximum interpolation distance of 5 mm provided LI values for unassigned vertices. Impedance maps were calculated with both $\mathrm{LI}_{\mathrm{movAvg}}$ and $\mathrm{LI}_{\mathrm{upEn}}$ as input. The extended mapping area was considered for the regional comparison of LI acquisitions including the PVs while impedance mapping itself was carried out for the mapping area only.

8.2.9 Statistical Analysis

Distributions were tested for normality with the Anderson-Darling test. Non-normal distributions were assumed if the test rejected the null-hypothesis of a normal distribution at a 1 % significance level. Non-normal distributions with unpaired samples were compared with the Mann-Whitney U-test. Normally distributed paired data sets were tested with the paired samples t-test. The significance level was set to 1 %. Medians and inter-quartile ranges are reported to describe distributions. The central line of all boxplots describes the median while the boxes range from the 25^{th} to the 75^{th} percent quantile. The whiskers extend to the outermost data points that were not considered outliers. The underlying distributions of adjacent boxplots were compared by statistical significance testing as appropriate. Asterisks denote that the null-hypothesis of equal underlying distributions was rejected. The coefficient of determination R^2 was used to describe the relation between two dependent variables.

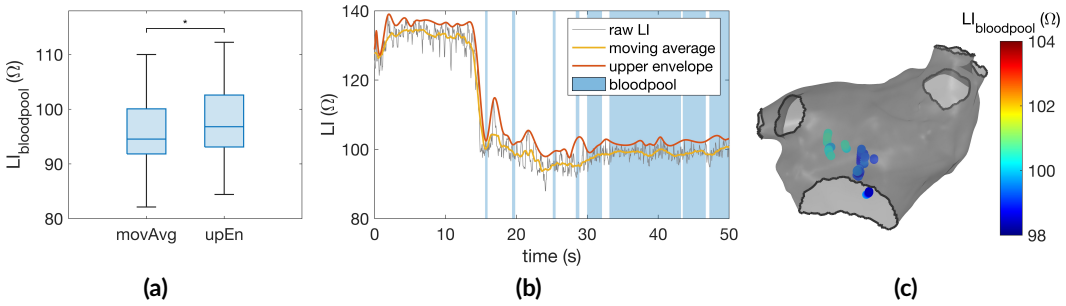

Figure 8.2: Bloodpool reference impedance. (a) Distribution of $LI_{bloodpool}$ retrieved from LI_{movAvg} and LI_{upEn} for all 14 patients. The asterisk (*) denotes statistically significant difference between the distributions. (b) Exemplary trace of LI_{raw} with corresponding LI_{movAvg} and LI_{upEn}. Samples with valid bloodpool acquisitions are marked in blue. (c) LA endocardial shell with spatial location of valid bloodpool acquisitions. Reproduced from [73].

8.3 Results

8.3.1 Patient Demographics

The study comprised 14 patients (female n = 5). The subjects' age ranged from 41 to 71 years with a mean age of 64 years. Twelve subjects were diagnosed with paroxysmal AFib, two subjects with persistent AFib. Eleven subjects underwent redo PVI while the remaining ones presented for de-novo PVI. During impedance mapping, five patients were in sinus rhythm, four patients in paced rhythm, two patients in AFib, and three patients in alternating rhythm including sinus and paced rhythm, AFib, and atrial flutter.

8.3.2 Bloodpool Impedance

Only a slight shift distinguished the reference $LI_{bloodpool}$ depending on whether LI_{movAvg} or LI_{upEn} was provided as the input LI. With a median of 96.8 Ω (inter-quartile range 9.5 Ω) amongst all patients, $LI_{bloodpool}$ retrieved from LI_{upEn} exceeded the median of $LI_{bloodpool}$ retrieved from LI_{movAvg} at 94.6 Ω (inter-quartile range 8.3 Ω). Statistical testing evaluated the distributions as different $\left(p = 2 \cdot 10^{-9}\right)$. Fig. 8.2 (a) displays the distribution of both $LI_{bloodpool}$ measures for all patients. Any value was within clinically observed ranges and in line with manually noted $LI_{bloodpool}$ values for the individual patients. The deviation between $LI_{bloodpool}$ automatically retrieved from LI_{movAvg} and $LI_{bloodpool}$ retrieved from LI_{upEn} for individual patients ranged from 1.2 Ω to 4.1 Ω with a median of 2.4 Ω.

Fig. 8.2 (b) shows an exemplary excerpt of an LI_{raw} trace overlaid by the corresponding LI_{movAvg} in yellow and LI_{upEn} in orange. Being the upper envelope of LI_{raw}, LI_{upEn} exceeds

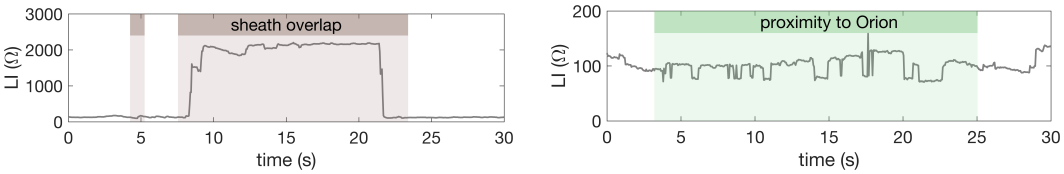

(a) Sheath overlap. **(b)** Proximity to IntellaMap™ Orion.

Figure 8.3: LI_{raw} artifacts attributed to an overlap with the steerable sheath in (a) as well as attributed to the proximity to the IntellaMap Orion™ catheter in (b). Brown background marks samples that were excluded due to a suspected overlap with the steerable sheath. Green background marks samples that were excluded due to proximity to the IntellaMap Orion™. Reproduced from [73].

LI_{movAvg}. Samples that were taken into account for determining $LI_{bloodpool}$ are marked in blue. LI_{raw} significantly drops at 14 s when the catheter looses endocardial contact. Fig. 8.2 (c) visualizes the locations of acquisition for all $LI_{bloodpool}$ samples with an LI between the 10 % and 90 % quantile color-coded by the respective LI_{movAvg}. All acquisitions are located centrally in the LA cavity.

8.3.3 Exclusion of Artifacts

Table 8.1: Exclusion of LI measurements. Minimum, median, and maximum percentage of all patients. Reproduced from [73].

	Min	Median	Max
Sheath overlap	1.0 %	8.5 %	32.8 %
Catheter movement	5.0 %	12.2 %	20.0 %
Proximity to Orion	0.0 %	0.0 %	8.1 %
Distance to wall	9.2 %	20.2 %	46.1 %

Due to the availability of many measurement points independent from the atrial rhythm in combination with a high probability for artifacts in the LI trace, exclusion criteria were set conservatively. Table 8.1 gives an overview of timely percentages per exclusion reason. Since an IntellaMap Orion™ catheter was present in less than half of the patients during map acquisition with the IntellaNav MiFi™ OI catheter, both the minimum and median exclusion percentage counted 0.0 %. An increased distance to the endocardium was the most prominent reason for the exclusion of LI samples. The spectrum of percentages with the possibility of an overlapping sheath spread from 1.0 % to 32.8 %. The high maximum percentage was associated with cases for which data acquisition continued after completion of mapping when the IntellaNav MiFi™ OI had already been drawn back into the sheath.

Fig. 8.3 presents exemplary traces of characteristic LI traces for artifacts attributed to an overlap with the steerable sheath in panel (a) and attributed to the proximity to the IntellaMap Orion™ in (b). Fig. 8.3 (a) displays the characteristic LI trace for complete sheath coverage. LI_{raw} increases to unphysiological values above 1000 Ω due to full retraction of the IntellaNav MiFi™ OI into the sheath made from electrically highly resistive material. Other examples with partial coverage of the IntellaNav MiFi™ OI by the sheath were also detected successfully. As opposed to the electrically highly resistive sheath material, other catheters such as the IntellaMap Orion™ are partially composed of metallic materials of low electrical resistance resulting in unphysiologically abrupt drops in LI_{raw} down to 71.0 Ω as depicted in Fig. 8.3 (b).

8.3.4 Impedance Mapping

LI by Distance to Endocardium

In order to assess a possible causal relationship between the LI measurements and the distance to the endocardial wall, all valid LI acquisitions of all patients were referenced to their individual $LI_{bloodpool}$ by subtraction. A linear regression showed that the LI tends to drop by 1.14 Ω per additional mm distance to the endocardium. However, a low regression coefficient of determination $R^2 = 1$ % indicated that the distance to the endocardial wall is only a minor determinant of LI and is joined by a series of other influencing factors that in sum result in the measured LI.

LI by Anatomical Region

Within individual patients, the distributions of LI measurements at times differed significantly between the anterior, posterior, inferior, septal, and lateral wall. However, a clear trend did not become apparent amongst patients. Referencing all LI acquisitions of all patients to the corresponding reference $LI_{bloodpool}$ allowed for inter-patient statistics as depicted in Fig. 8.4. The impedance ranges measured for the distinct atrial walls were very similar, with a median LI_{upEn} elevation above $LI_{bloodpool}$ between 15.7 Ω and 19.9 Ω and inter-quartile ranges between 19.0 Ω and 24.8 Ω. Both median and inter-quartile range were highest for the posterior wall. The distributions for all four PVs significantly differed from the atrial walls with median LI_{upEn} elevations above $LI_{bloodpool}$ of 29.2 Ω to 45.9 Ω and inter-quartile ranges between 30.8 Ω and 54.8 Ω. The LI within the inferior PVs exceeded the LI within the superior PVs. The Mann-Whitney U-test for unpaired samples and a significance level of 1 % yielded that the distribution for any anatomical region was statistically significantly different from any other region with the exception of the lateral and the inferior wall. The p-values amongst pairs of the atrial walls were found to exceed the p-values of pairs combining any atrial wall with any PV by several decades.

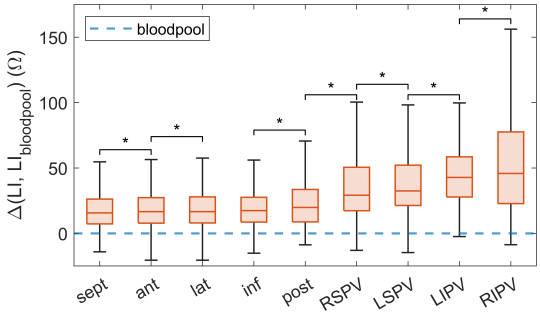

Figure 8.4: Difference between LI_{upEn} as mapped to the endocardium within the extended mapping region and $LI_{bloodpool}$ combined by anatomical region for all patients. Arranged by ascending median. The virtual $LI_{bloodpool}$ corresponds to 0 Ω. Adjacent distributions which were statistically significantly different are marked with a *. Reproduced from [73].

LI on and adjacent to previous PVI Lesion

PVI lesions from previous procedures served as regions of known atrial substrate to assess the capabilities of LI to conclude on substrate properties. In a first step, the distribution of LI_{upEn} along a line perpendicular to the PVI lesion from a previous procedure was analyzed. Fig. 8.5 (a) and (b) show the bipolar voltage map and the LI_{upEn} map for an exemplary patient that had undergone previous PVI. Ablation points from the previous procedure were mapped to the current geometry and are displayed as black dots in Fig. 8.5. The ablation points were found to match the step in the voltage map in Fig. 8.5 (a) indicating the position of the PVI lesion. Any LI acquisition originating from within a tube of 7 mm radius centered on the grey line perpendicular to the PVI lesion in Fig. 8.5 (b) was projected to the grey line and assigned a geodesic distance to the PVI line along the endocardial mesh. Fig. 8.5 (b) summarizes the distribution of LI_{upEn} along the grey line in the lower panel. While LI_{upEn} drops below 100 Ω close to the lesion, it rises above 110 Ω with increasing distance to the previous PVI in both directions (LA roof and left superior PV). Both the variance and the absolute value were higher towards the left superior PV compared to the LA roof.

Fig. 8.6 (a) shows the extension of the analysis to an entire PVI lesion of an exemplary patient for an assumed PVI width of 5 mm and a margin of 10 mm width. For both right PVI (RPVI) and left PVI (LPVI), LI_{upEn} within the margin significantly exceeded LI_{upEn} within the PVI region. In contrast, the distributions of LI_{upEn} did not differ significantly for an exemplary control patient as shown in Fig. 8.6 (b). Varying the width of the PVI region and the margin and averaging over all patients with previous PVI confirmed the observation. As reflected by positive values of ΔLI in Fig. 8.6 (c), the PVI margin exceeded the PVI region in LI across all patients. Small PVI widths in combination with small margin widths did not show significant differences presumably because both the PVI region and the margin were embedded in the actual lesion. Larger widths consistently resulted in significant differences. In contrast, this trend did not appear for the average control patient as presented in Fig. 8.6 (d). For all combinations of PVI widths and margin widths, ΔLI of the PVI group

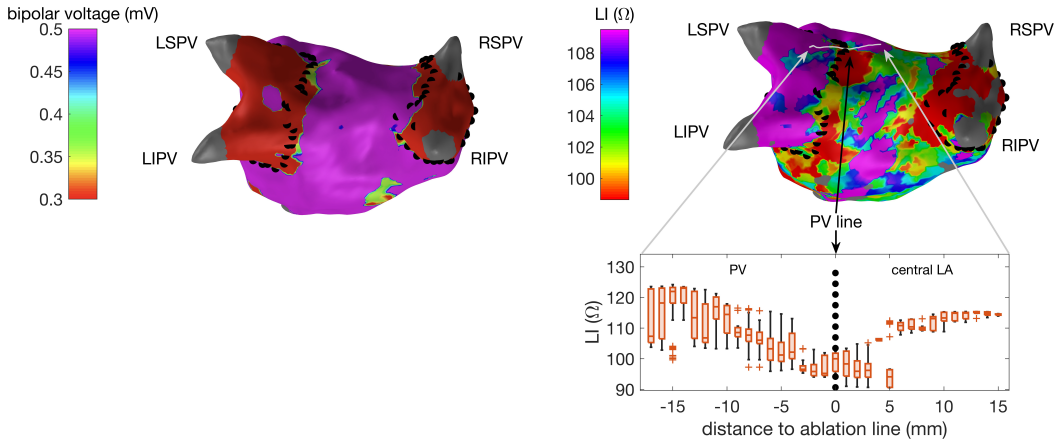

(a) Bipolar voltage map. **(b)** LI map.

Figure 8.5: LA in posterior-anterior perspective with color-coded bipolar voltage map (a) and LI map (b). Left superior, left inferior, right superior, and right inferior PVs are labelled as LSPV, LIPV, RSPV, and RIPV. PVI ablation points from a previous intervention are marked by black dots. The LI map in panel (b) includes a light grey line indicating a path perpendicular to and approximately centered on the previous PVI lesion next to the LSPV. The distribution of LI measurements along this path shows a drop at the previous PVI lesion (b). Adjacent distributions were not tested for statistical significance. Reproduced and adapted from [73].

exceeded ΔLI of the control group by 5.1 Ω on average. When considering only PVI widths greater than or equal to 5 mm as well as margin widths greater than or equal to 10 mm, the ΔLI within the PVI group exceeded ΔLI within the control group by 7.7 Ω on average.

LI in Regions of Native Pathological Substrate

Besides unraveling previously ablated substrate, LI mapping was tested for its capabilities in distinguishing natively developed pathological substrate from healthy tissue. Since the ground truth of the pathological status of tissue was not available, an exemplary native scar at the anterior wall of the LA was deduced from thorough bipolar voltage mapping as displayed in Fig. 8.7. The LI within the mapped scar area measured 115 Ω as compared to 133 Ω in the adjacent high voltage region. Fig. 8.7 (a) and (b) present screenshots of the respective measurements taken during the procedure with the LI trace in yellow and the the LI value in light blue.

8.3.5 LI Oscillations

LI_{raw} significantly oscillated predominantly with the atrial and ventricular rhythm as well as with the respiratory rate. Fig. 8.9 depicts six exemplary LI traces in combination with Einthoven lead I and four bipolar CS EGMs. Based on the exemplary traces, the morphology,

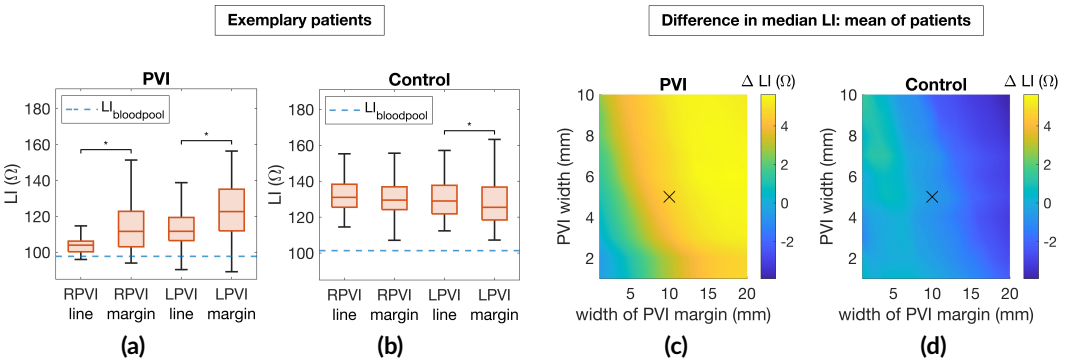

Figure 8.6: Distribution of LI_{upEn} for an exemplary patient with previous PVI (a) and an exemplary control patient (b) for the RPVI and LPVI region of 5 mm width as well as the respective margins of 10 mm width. The difference in median LI_{upEn} between the RPVI region and the RPVI margin as well as the LPVI region and the LPVI margin is summarized for all PVI patients (c) and all control patients (d) for different widths of the PVI regions and the margins in the lower panels. Colors indicate the elevation of LI_{upEn} within the margin compared to the PVI line with negative or small elevations in blue and large elevations in yellow. The black crosses mark the widths of 5 mm and 10 mm for PVI region and PVI margin as chosen for the exemplary distributions in (a) and (b). Asterisks (*) denote statistically significant difference between distributions. Reproduced and adapted from [73].

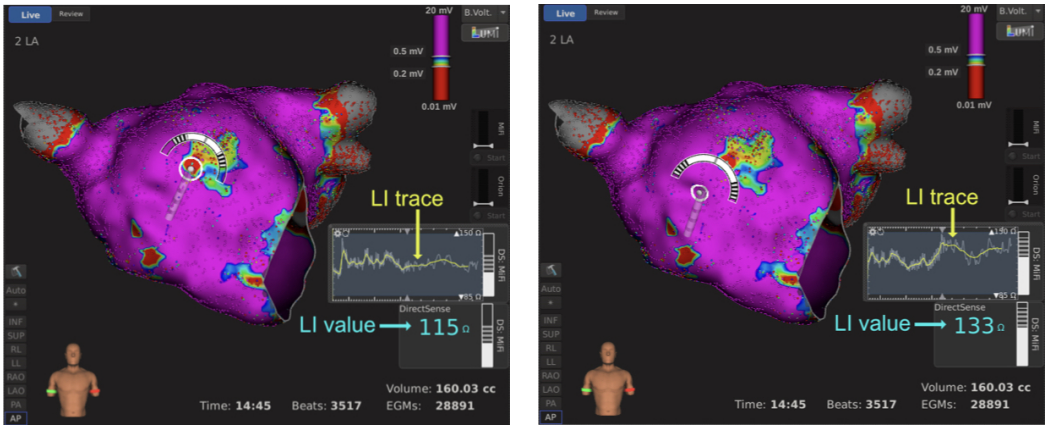

(a) LI in pathological region.

(b) LI in high voltage region.

Figure 8.7: Bipolar voltage map of the LA in anterior view. Bipolar voltages below 0.2 mV are colored in red, above 0.5 mV in purple and between 0.2 mV and 0.5 mV in rainbow colors. The anterior wall presents centrally with a native pathological substrate of lowered bipolar EGM amplitude. LI trace presented as an overlap of LI_{raw} (grey) and LI_{movAvg} (yellow) and LI value (light blue) within the pathological region (a) and the adjacent high voltage region (b). Reproduced from [73].

amplitude, and origin of oscillations in LI_{raw} were analyzed. Panels (a) and (b) in Fig. 8.9 show acquisitions during sinus rhythm with moderate oscillatory amplitudes between 15 Ω and 20 Ω. While the trace in Fig. 8.9 (a) comes with one distinctive maximum shortly after the ventricular contraction followed by a gradual decline in LI_{raw}, the oscillatory morphology in Fig. 8.9 (b) is m-shaped and presents two maxima. Recorded in sinus rhythm,

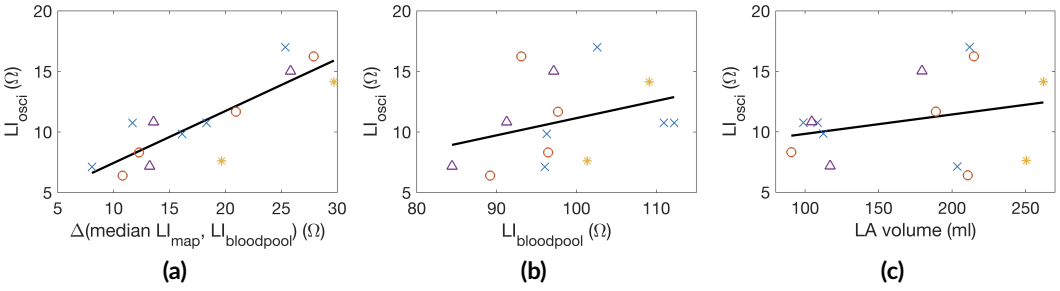

Figure 8.8: Dependency of the median LI oscillation on the elevation of the median LI_{upEn} of the LI map above $LI_{bloodpool}$ (a), on $LI_{bloodpool}$ (b), and on the LA volume (c). Markers indicate the cardiac rhythm during map acquisition. The linear regression is displayed as black line. Reproduced and adapted from [73].

the oscillations could originate from the atrial contraction, the ventricular contraction or a superposition of both. Fig. 8.9 (c) displays a recording during AFib with comparable oscillatory amplitude. In view of the highly irregular atrial rhythm, the oscillations clearly relate to the ventricular contraction in this case with one oscillatory cycle per RR interval. The examples in Fig. 8.9 (d), (e), and (f) were recorded during fixed rate pacing from the CS. Fig. 8.9 (d) covers an extended time window of 15 s and contains 3.5 respiratory cycles resulting in a superposition of cardiac and respiratory oscillations in LI_{raw}. Fig. 8.9 (e) and F demonstrate the influence of atrial activation on the oscillatory components in LI_{raw}. Physiologically, captured atrial stimuli are characterized by a proximal to distal CS sequence and a constant stimulus to CS interval. The third, sixth, and eighth stimulus in Fig. 8.9 (e) are preceded by a spontaneous atrial activation, indicated by the distal to proximal CS sequence followed by a loss of capture of the following stimulus. The difference in LI oscillation of the third, sixth, and eighth beat compared to the other beats suggests a dependency on the atrial activation sequence and the atrial-ventricular timing. A similar conclusion was drawn from the trace in Fig. 8.9 (f). One of the atrial activations is not followed by a ventricular contraction. However, the oscillatory morphology in LI_{raw} is very similar to the other atrial beats that are followed by a ventricular activation being suggestive of an oscillatory origin in the atria.

Fig. 8.8 visualizes possible dependencies of the median oscillatory amplitude. The differences in the median oscillatory amplitude could not be explained by $LI_{bloodpool}$ or the LA volume as indicated in Fig. 8.8 (b) and (c) as well as coefficients of determination $R^2 = 10.9\,\%$ and $R^2 = 7.6\,\%$, respectively. The median LI oscillation amplitude correlated well with the elevation of the median LI_{upEn} above $LI_{bloodpool}$ within the mapping region as displayed in Fig. 8.8 (a) and emphasized by a coefficient of determination $R^2 = 72.1\,\%$. The median oscillatory amplitude was not dependent on the cardiac rhythm during map acquisition.

Causal relationships were neither found between the morphology of the oscillation and the anatomical region nor between the oscillation amplitude and the anatomical region.

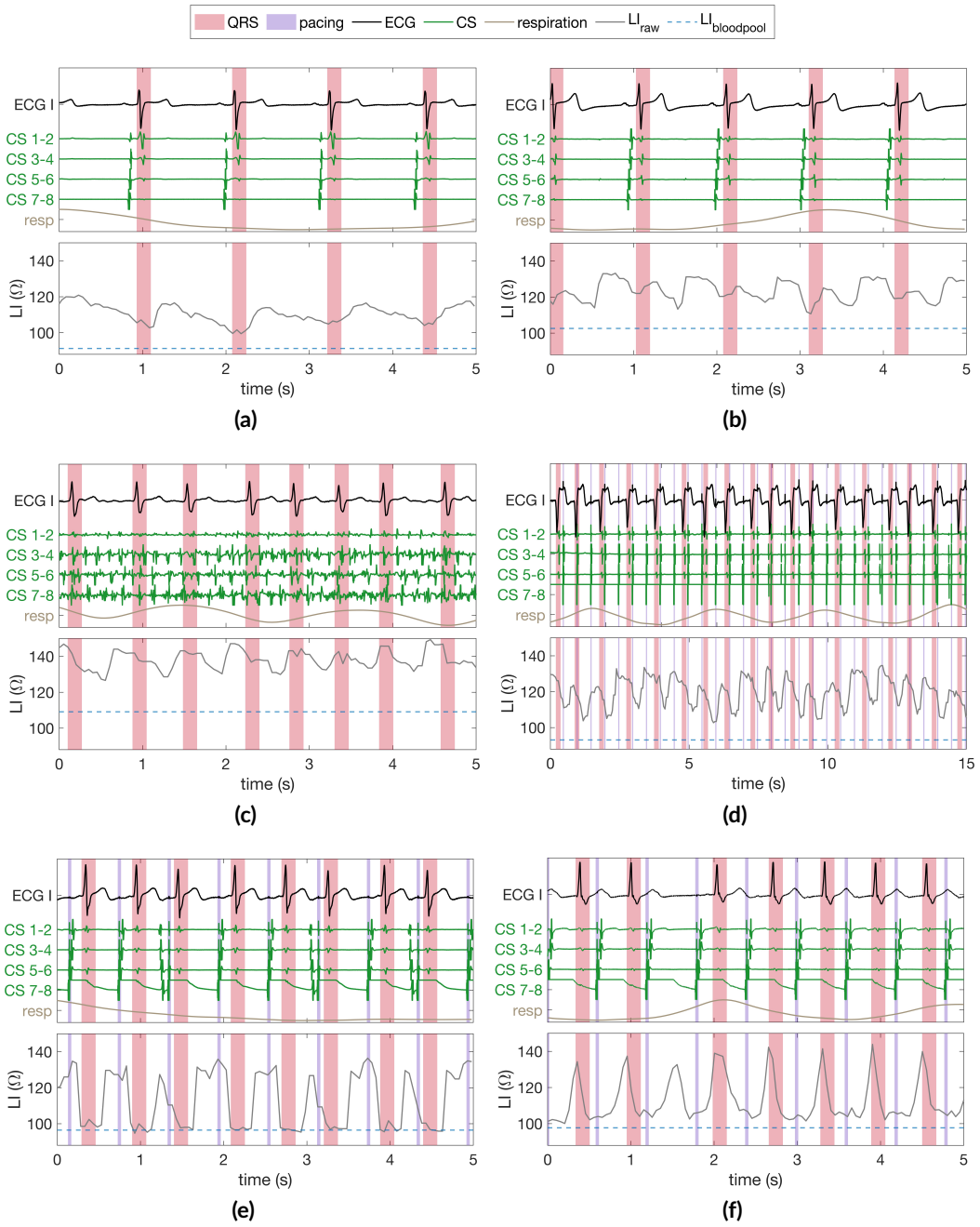

Figure 8.9: Panels (a) to (f) show different examples of oscillatory amplitudes, morphologies, and dependencies in LI_{raw}. Traces of LI_{raw} in the respective lower panel in grey along with the corresponding bipolar CS EGMs in green, Einthoven lead I in black, and the respiratory phase in brown in the respective upper panel. $LI_{bloodpool}$ is given as a broken blue line in the lower panel. QRS complexes are shaded in red. Pacing events are shaded in violet. Reproduced from [73].

8.4 Discussion

In summary, this study provided novel insights into the potential of LI mapping for substrate characterization. With the automatic determination of the bloodpool reference LI, the proposal of adequate preprocessing steps, and the assessment of LI as a surrogate for substrate characteristics, we integrally shed light on a previously unexplored field.

With the identification of native fibrotic and preablated scar tissue in previous PVI lesion areas by LI, substrate mapping by means of LI was proven possible and fosters confidence for the future of propagation independent substrate mapping. Fig. 8.5 clearly shows the difference in information of voltage maps and LI maps: An area behind a closed ablation line does not show any voltage, but still the LI can be measured and used for substrate characterization. Despite the proof of concept presented in this work, the capabilities of LI-based substrate mapping are not yet fully exploited. Many confounding factors such as the distance to the endocardial wall, oscillations in LI_{raw} due to the cyclic loss of wall contact, varying contact force between catheter and endocardium, the orientation of the catheter, and partial coverage of the catheter by the sheath hinder the LI measurement. The distance to the endocardial wall, for example, was calculated based on the dynamic catheter position and the static endocardial shell. Cardiac movements caused by cardiac contractions and respiration introduce uncertainties in the distance that can only partially be accounted for. On average, the dependency of LI on the distance to the endocardium showed the same trend as previously observed in a controlled environment [13]. The dependency is also in accord with the previously found correlation between LI and EGM amplitude [50]. If several LI measurements mapped to the same surface vertex, choosing the upper quartile meant to decide for those measurements with better endocardial contact in this work. However, the IntellaNav MiFi™ OI comes without contact force sensor resulting in LI measurements at uncontrolled endocardial contact. A more accurate distance or contact measure has the potential to improve the accuracy of LI mapping in the future. The introduction of a contact force sensor within the IntellaNav Stablepoint™ (Boston Scientific, Malborough, MA, USA) has been a recent step towards this direction. Many of the previously mentioned confounding factors could potentially also be resolved in the future by complementing the currently available measurements by multi-electrode injection and measurement circuits or by current injections at different frequencies.

LI mapping of 14 patients gave rise to the conclusion that the anatomical location of acquisition outside the PVs does not significantly bias the meaning of LI to conclude on substrate properties. The anterior, posterior, inferior, and septal wall showed similar but statistically different distributions of LI. Solely the posterior wall stood slightly out in absolute numbers with an increased LI, which could potentially be caused by the difference in catheter positioning. Depending on the location of the transseptal puncture, the catheter might reach the posterior wall with a by default increased contact force [79] resulting in a deeper immersion of the catheter tip into the atrial tissue compared to the remaining atrium.

In contrast, the LI inside the PVs exceeded the LI in the remaining atrium presumably due to the smaller lumen and different substrate of the PVs as previously shown in impedance studies with generator impedance setups [80]. With the inferior PVs usually being smaller in diameter than the superior PVs [81], the smaller lumen could also explain higher LI values in the inferior PVs compared to the superior PVs.

The range of the automatically determined reference $LI_{bloodpool}$ with a median slightly below $100\,\Omega$ compared well with other studies [50] [49].

Considering that standard treatments such as stand-alone PVI remain unsuccessful for a non-negligible subgroup of AFib patients [82], substrate mapping has generally gained attention in recent years. While the most accurate picture of the substrate could be obtained from histological analysis, in-human histology is not possible to the required extent and one has to fall back upon rather indirect measures reflecting the composition and pathology of the substrate. Electrogram-based substrate mapping approaches such as voltage or fractionation mapping have led to ambiguous outcomes in various studies [83] [84] [85]. To a certain extent, acpEGM indirectly reflect the state of the cardiac tissue by means of its effect on excitation propagation. However, it has to be taken into account that the direction of the propagation mechanism during mapping takes strong influence on EGM morphology and amplitude. Impedance mapping, on the contrary, is mostly independent from the current mechanism of excitation. While histology cannot be performed, impedance mapping may bridge the gap by complementing existing EGM-based substrate mapping approaches. Information on the resistivity of the tissue is not equivalent to histological analysis but can partially untangle the unknown composition of the underlying substrate. In combination with EGM-based information on how the substrate supports and influences the spread of excitation, pathological areas can be explored from two different perspectives to build up an extensive picture of the atrial substrate. A thorough analysis of the complementarity of EGM-based substrate mapping approaches and LI maps in a large patient population was out of the scope of this work but will need to bring further insights in future studies.

Many electroanatomical mapping systems are capable of measuring transthoracic generator impedance but do not yet incorporate high-frequency current injection and voltage measurement in an intra-cardiac catheter without including a cutaneous reference patch in the injection circuit. Local current injection and voltage measurement bears the advantage of pronouncing local influences on the spread of the electrical field with a decreased sensitivity to distant changes in conductivity caused by the respiratory cycle, e.g.. While LI measurements are theoretically possible with any multi-electrode catheter, the Rhythmia HDx system with the IntellaNav MiFi™ OI and the IntellaNav StablePoint™ catheter are currently the only clinically available systems providing the hardware, software, and visualization tools to conduct in-human LI measurements. Therefore, the suggested pipeline for LI mapping can so far only be applied to Rhythmia HDx recordings with either the IntellaNav MiFi™ OI or the IntellaNav Stablepoint™ catheter.

The high correlation between the oscillatory amplitude and the elevation of the median mapping LI above $LI_{bloodpool}$ within the mapping region strongly suggests that the common

origin of oscillations in LI_{raw} is the establishment and the loss of endocardial contact. Since patients present with a wide variety of $LI_{bloodpool}$ and presumably also a variety in the LI of the atrial tissue, the elevation of the median mapping LI above $LI_{bloodpool}$ is a patient-specific determinant of the oscillatory amplitude.

Within an individual patient, the raw LI recording oscillated with different amplitudes, morphologies, and phases. Evidence was provided that the interaction of three oscillatory components — namely the atrial, the ventricular, and the respiratory component — led to the overall oscillation pattern observed in LI_{raw}. The complex dynamics of the beating heart inside the breathing thorax suggests that the overall oscillation pattern is additionally dependent on a multifactorial chain of dependencies. The mechanical positioning of the catheter within the LA may play a significant role. With the sheath passing the atrial septum, the catheter will move with the septum to a certain extent. Furthermore, the curvature of the catheter within the LA can influence the actual catheter movement and stability. Additionally, different anatomical regions may move more during the atrial and ventricular beat than others. The complex interplay of the atrial movement with aforementioned mechanical factors could explain that no direct dependency was evident between the anatomical region and the oscillation amplitude within individual patients. While the atrial, the ventricular, and the respiratory component of LI oscillations were unraveled in this study, available measurements did not allow to conclude on the origin of additional oscillatory morphology and amplitude components, possibly due to unknown factors such as the curvature of the catheter and the complex dynamics of cardiac mechanics.

With the moving average and the upper envelope, two different methods were described to tackle the oscillations in LI_{raw} with a high potential to flaw the meaning of LI maps. Coming from the insight that oscillations originate from the establishment and loss of wall contact, the summits of one oscillatory cycle were assumed to best resemble the LI of the underlying tissue. While the moving average takes into account any value during an oscillatory cycle, the upper envelope focuses on the interpolation of the maxima and therefore maximizes the elevation above the baseline $LI_{bloodpool}$. Therefore, most analyses in this work favored LI_{upEn} over LI_{movAvg} despite the current implementation of the moving average in the clinical system. A potential drawback of LI_{upEn} compared to LI_{movAvg} is the increased impact of high amplitude artifacts. However, conservative exclusion criteria led to the conclusion that the advantages of LI_{upEn} prevail.

8.4.1 Limitations

While this study showed that LI mapping bears great potential, the limitations as discussed in the previous paragraphs will be summarized in the following: Despite the proposal of adequate preprocessing steps, confounding factors remain and hinder LI mapping. Above all, the lack of a wall contact or contact force sensor results in uncertainties that should be addressed in future work. Since this study focused on the exploration of LI mapping itself, a

thorough comparison to other substrate mapping approaches based on EGMs was out of the scope of this work. The complementarity of different substrate mapping approaches remains to be quantified in future analyses. Finally, the described LI mapping methods are so far only applicable to the IntellaNav MiFi™ OI and the IntellaNav Stablepoint™ being the only clinically available catheters equipped with LI measurement circuits.

8.4.2 Conclusion

To conclude, this study demonstrated that LI mapping shows great potential to complement EGM-based substrate mapping. Both previously ablated and native scar areas were identified irrespective of local excitation in LI recordings. Oscillations pose a major challenge to adequate preprocessing. The upper envelope of the raw LI measurement should be preferred to the moving average in order to suppress oscillation artifacts while maximizing the elevation above the baseline LI of the surrounding bloodpool.

Chapter 9

Inverse Reconstruction of Atrial Tissue Conductivity

9.1 Introduction

Electrical impedance has a long history in medical diagnosis and imaging. Since Gabriel et al. [55] studied the dielectric properties of different kinds of tissue, electrical impedance tomography (EIT) of the lungs has become one of the most popular applications in the medical field. A chest belt equipped with electrodes injects an alternating current non-invasively and measures the resulting potential distribution to conclude on the ventilatory status of the lungs taking advantage of the low conductivity of air compared to body tissue and fluids. Impedance measurements have also become an established tool in cardiac electrophysiology to monitor catheter-tissue coupling during radio frequency energy ablation by measuring the impedance of the energy delivery pathway. However, the bulk impedance of the torso strongly limits local resolution. Instead of falling back on the unipolar impedance measured by the radio frequency generator, efforts have been made to monitor thermal changes during radio frequency ablation with an EIT system combining a cutaneous grid of chest electrodes with an intra-cardiac catheter [86] to reconstruct tissue heating during radio frequency energy delivery with a multi-electrode tomographic approach. However, impedance related noise such as respiratory ventilation and myocardial perfusion as well as movement related sources of noise have been identified as challenges. *In vitro* experiments showed that a combination of external and intra-cardiac coronary sinus (CS) and ablation catheter electrodes was capable of reconstructing lesion boundary and depth [87] [88].

The recently introduced DirectSense™ technology returns to point-by-point measurements instead of the previously described tomographic approach but comprises both injection and measurement circuit within the intra-cardiac catheter. The so-called local impedance (LI) is clinically intended to monitor ablation lesion formation [47] [13] and predict lesion durability. Pilot studies have shown that LI also distinguishes physiological substrate of high impedance from pathologically altered substrate of lower impedance [49] [50] including the compilation

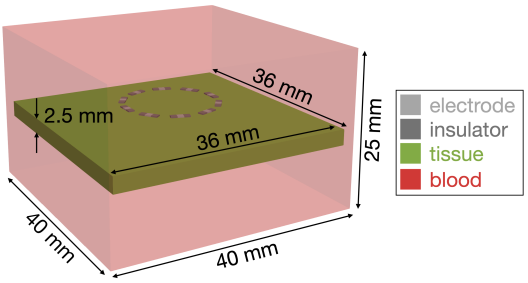

Figure 9.1: Geometrical setup for electrical forward simulation. A patch of tissue is embedded within a box of blood. A set of electrodes hovers the tissue.

of full-chamber impedance maps [73]. In view of non-satisfactory and ambiguous success rates of electrogram (EGM)-based substrate mapping, local impedance mapping could bridge the gap and unravel hidden information on the state of cardiac tissue. However, confounding factors pose major challenges to quantitative LI mapping.

This study, for the first time, introduces a purely intra-cardiac EIT system theoretically applicable to any multi-electrode mapping catheter with the aim of reconstructing local tissue impedance as a surrogate for tissue pathology. *In silico* experiments with various distributions of scar tissue within healthy myocardium were conducted to assess feasibility of this potentially novel mapping modality and outline future clinical potential.

9.2 Methods

9.2.1 Geometrical Setup

An *in silico* environment for forward simulation of the electrical field was implemented as depicted in Fig. 9.1. A patch of tissue measuring 36 mm in width and length at a thickness of 2.5 mm was embedded into a box of blood spanning 40 mm × 40 mm × 25 mm. Catheter electrodes were placed centrally above the tissue. Five different electrode geometries were realized including a zero-dimensional point electrode and four three-dimensional electrodes as depicted in Fig. 9.2. The spherical electrode was fully parametrized by its radius $r_S \in \{0.25\,\text{mm}; 0.50\,\text{mm}; 0.75\,\text{mm}\}$. The cylindrical electrode was composed of a central metallic part embraced by two insulating cylinders at the left and right. The radius of the cylinder $r_C \in \{0.25\,\text{mm}; 0.50\,\text{mm}; 0.75\,\text{mm}\}$, the length of the metallic electrode $l_C \in \{0.5\,\text{mm}; 1.0\,\text{mm}; 1.5\,\text{mm}; 2.0\,\text{mm}\}$, and the length of the insulating segments $l_I = 1\,\text{mm}$ defined the cylindrical electrode. The cuboid electrode was accordingly composed of a central metallic part lined by insulating segments to the left and right. The fixed height $z_C = 0.2\,\text{mm}$ was combined with varying width and length of the central metallic segment with $x_C = y_C \in \{0.5\,\text{mm}; 1.0\,\text{mm}; 1.5\,\text{mm}\}$. The adjacent insulating segments measured $l_I = 1\,\text{mm}$

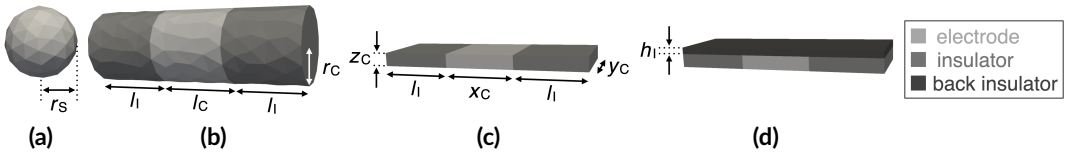

Figure 9.2: Distinct three-dimensional electrode geometries and respective parameters. (a) spherical electrode, (b) cylindrical electrode, (c) cuboid electrode, (d) cuboid electrode with insulator at the rear.

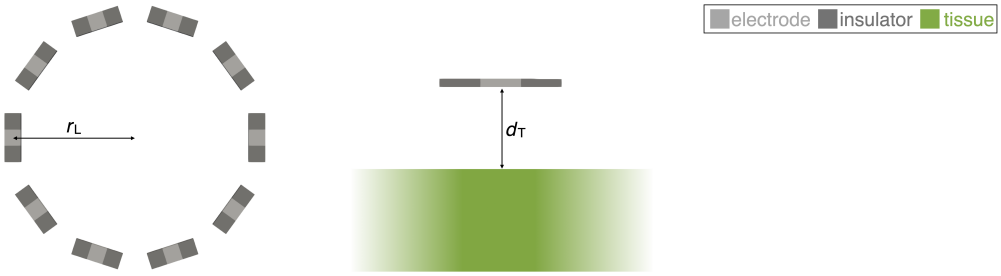

(a) 10-pole circular catheter. Top view.

(b) Cross-section of electrode elevation above the tissue surface.

Figure 9.3: Circular catheter geometry with respective parameters in top view as well as elevation above the tissue surface as cross-section.

in length. Finally, the cuboid electrode with an insulator at the rear was parametrized alike the pure cuboid electrode adding an insulating plate covering the surface facing away from the tissue. In total, 22 different electrodes resulted from the parametrizations described above.

Electrodes were arranged in a circle mimicking the Achieve Advance™ (Medtronic, Dublin, Ireland), the Advisor™ FL circular mapping catheter (Abbott, Chicago, IL, USA), or the LASSO™ catheter (Biosense Webster, Irvine, CA, USA). The circular shape comprising 10 electrodes is depicted in Fig. 9.3 (a). Two different radii $r_\mathrm{L} \in \{7.5\,\mathrm{mm}; 12.5\,\mathrm{mm}\}$ were implemented following typical clinical sizes. The distance between catheter and tissue d_T as schematically depicted in Fig. 9.3 (b) was varied from 0 mm to 2 mm in steps of 0.5 mm.

Combining all variations summed up to 22 electrodes · 2 catheter radii · 5 distances = 220 geometrical setups.

For each setup, six different tissue configurations were implemented including homogeneously physiological tissue, an equal split in physiological tissue and scar, a central line of scar of 1 mm width, a central line of scar of 3 mm width, a central cylindrical scar of 2 mm radius, and a central cylindrical scar of 5 mm radius as depicted in Fig. 9.4. All scars were transmural. As a result, 220 · 6 = 1 320 different scenarios were parsed to the simulation and reconstruction pipeline as described in the following.

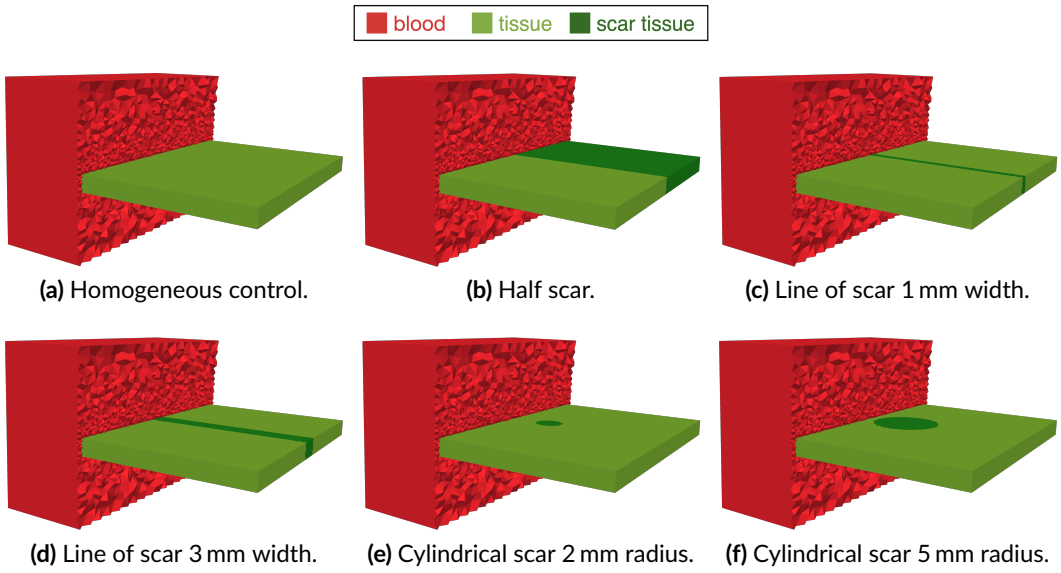

(a) Homogeneous control. **(b)** Half scar. **(c)** Line of scar 1 mm width.

(d) Line of scar 3 mm width. **(e)** Cylindrical scar 2 mm radius. **(f)** Cylindrical scar 5 mm radius.

Figure 9.4: Different pathological configurations of scar tissue and homogeneous control tissue surrounded by a box of blood represented by a partial cross-section.

9.2.2 Material Properties

The tetrahedral elements of the geometrical meshes were assigned conductivity values characteristic for the respective material at $f_1 = 14.5\,\text{kHz}$ and $f_2 = 2.5\,\text{MHz}$ for body temperature as summarized in Table 9.1. f_1 was selected as the frequency implemented in the DirectSense™ [13] technology with proven clinical feasibility. f_2 was chosen as secondary frequency for frequency-difference imaging. Fig. 9.5 shows the conductivity spectra of human blood, myocardial tissue, and connective tissue resembling myocardial lesions. Connective tissue consisting of mostly extracellular fluid shows least changes in conductivity while the conductivities of blood and myocardial tissue increase with increasing frequency due to the progressive accessibility of intracellular space with decreasing capacitive impedance of the cell membranes.

For time-difference imaging, two measurements are typically taken at two points in time that differ in the underlying spatial distribution of the conductivities of interest. One of the images is considered the background for difference imaging. As an alternative to a second measurement at a second point in time, the background image can be artificially calculated by assuming a homogeneous background. The reconstruction will then account for deviations from homogeneity. Two different homogeneous background conductivities were defined as noted in Table 9.1. σ_{BI} equals the conductivity of myocardial tissue. Since the patient specific conductivity of healthy myocardium is unknown in practice, σ_{BII} was randomly chosen to a value lower than both the myocardial and scar conductivity.

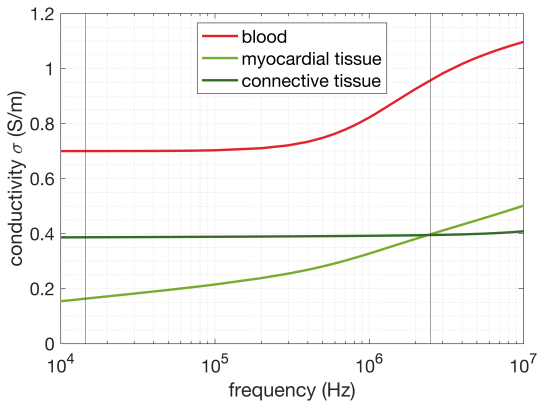

Figure 9.5: Conductivity of blood, myocardial tissue, and connective tissue between 10 kHz and 10 MHz. Vertical lines mark the frequencies $f_1 = 14.5\,\mathrm{kHz}$ and $f_2 = 2.5\,\mathrm{MHz}$. Data from [52] [68].

Table 9.1: Conductivities of relevant materials at 14.5 kHz and 2.5 MHz.

Material	Conductivity σ at 14.5 kHz (S/m)	Conductivity σ at 2.5 MHz (S/m)	Reference
metallic electrode	400 000	400 000	[67]
insulator	10^{-7}	10^{-7}	
blood	0.700	0.958	[52][68]
myocardial tissue	0.164	0.398	[52][68]
connective tissue (scar)	0.387	0.395	[52][68]
homogeneous background I	0.164	does not apply	
homogeneous background II	0.150	does not apply	

9.2.3 Stimulation Pattern

Two bipolar electrode directions were implemented for the circular catheter defined by the bipolar pairs as presented in Fig. 9.6 (a) and (b) with adjacent bipolar pairs and opposite bipolar pairs. Three different stimulation sets were implemented consisting of:

- only adjacent bipolar pairs
- only opposite bipolar pairs
- the combination of adjacent and opposite bipolar pairs.

For each set of simulations, each bipolar pair within the defined sets was chosen to be the stimulating pair once. All remaining bipolar pairs in the respective set which did not contain either of the stimulating electrodes were used as measuring bipoles sticking to four-terminal circuits throughout all simulations.

(a) Adjacent bipoles. **(b)** Opposite bipoles.

Figure 9.6: Bipolar electrode pairs for a circular catheter. Black dots represent electordes. Blue arrows denote bipolar pairs.

9.2.4 Forward Simulation

The spread of the electrical field was simulated with the software EIDORS v3.10 [69] and MATLAB R2021a (The MathWorks, Inc., Natick, MA, USA) as described in Section 3.3.1. In short, EIDORS solves the Laplace equation with a finite element model $\mathscr{F}$. The injection currents I are given as boundary conditions. The current density and the potential field are the solution. The voltage v between two electrodes is extracted as the potential difference and is dependent on the given conductivities $\boldsymbol{\sigma}$ at the elements of the model and the stimulating currents I of the electrode model with $v = \mathscr{F}(\boldsymbol{\sigma}, I)$ [69].

An alternating current of 5 mA peak-to-peak amplitude at 14.5 kHz was modeled. The complete electrode model was used [70]. For a total of M bipolar voltage measurements, the measurement vector $\boldsymbol{v} = [v_1, v_2, \ldots, v_M]$ was compiled and parsed to the inverse reconstruction as an input together with the geometrical mesh.

9.2.5 Inverse Reconstruction

Inverse reconstruction as described in Section 3.3.2 was performed by calculating the Jacobian matrix $\mathscr{J}$ and minimizing least square residuals. Both zero-order Tikhonov and Laplace regularization were applied while varying the discrete regularization parameter $\lambda = 10^x$ with x ranging from -7.5 to -4.5 in steps of 0.5. Three difference imaging approaches were followed:

- frequency-difference imaging with $f_1 = 14.5\,\text{Hz}$ and $f_2 = 2.5\,\text{MHz}$
- time-difference imaging with a homogeneous tissue background conductivity $\sigma_{\text{BI}} = 0.164\,\frac{\text{S}}{\text{m}}$
- time-difference imaging with a homogeneous tissue background conductivity $\sigma_{\text{BII}} = 0.150\,\frac{\text{S}}{\text{m}}$

For time-difference imaging, the conductivity of all tissue elements was set to σ_{BI} or σ_{BII}, respectively, while the conductivity of blood stayed indifferent.

Inverse reconstruction was performed on a two-dimensional mesh. Three-dimensional electrode positions were projected to the surface of the tissue. The enclosed surface was radially expanded by 1.5 mm and meshed with triangles with an average edge length of 0.2 mm.

Two regularization matrices, seven choices of the regularization parameter λ, three different stimulation patterns, and three different background images led to a total of 126 parametrization of the reconstruction. In combination with above-mentioned 1 320 geometrical parametrizations, a total of 166 320 reconstructions were analyzed.

9.2.6 Reconstruction Quality

The quality of the reconstruction was measured by the correlation coefficient and the mutual information between the ground truth of the spatial distribution of conductivities and the reconstructed image.

9.3 Results

All pathological geometries could be reconstructed. Reconstruction quality varied with reconstruction parameters and setup geometries and will be discussed in the following. Absolute values were not given importance to since only differences in conductivity compared to the respective background image were reconstructed. Fig. 9.7 shows reconstructed images and corresponding ground truth conductivity distributions. All distributions were captured correctly in shape. The size of the structures could not be distinguished in detail since all colorbar limits were individually set to the maximum and minimum value of the reconstruction. The range was smaller for small scar structures (line 1 mm and cylinder 2 mm) compared to the larger scar structures (line 3 mm and cylinder 5 mm).

9.3.1 Reconstruction Parameters

In a first step, the performance of different reconstruction parameters was assessed at the example of simple point electrodes with direct tissue contact. The reconstruction method was defined by the choice of the regularization matrix, the regularization parameter, the background image, and the stimulation pattern. For all other parameters, namely catheter radius, pathological geometry, electrode type, and distance to the tissue, any realization contributed to the statistics in the following. Fig. 9.8 shows that Laplace regularization was superior to zero-order Tikhonov regularization for all choices of the regularization parameter

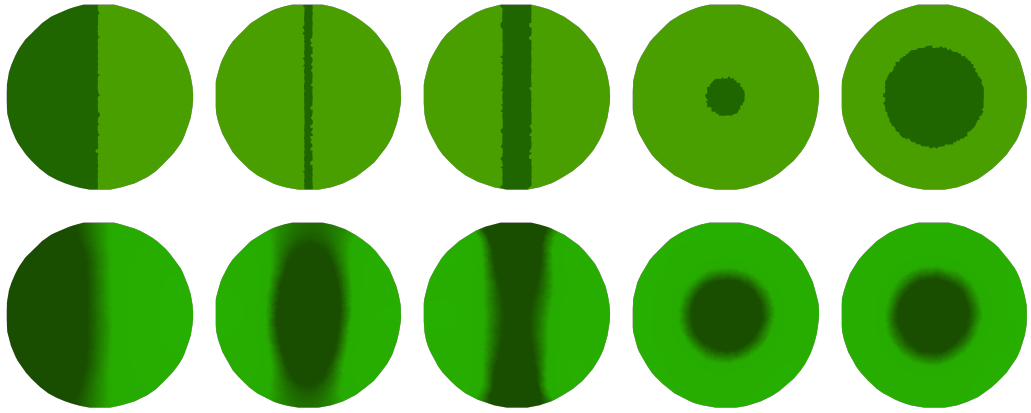

(a) 50:50. **(b)** Line 1 mm. **(c)** Line 3 mm. **(d)** Cylinder 2 mm. **(e)** Cylinder 5 mm.

Figure 9.7: Relative conductivity reconstruction examples (bottom row) with corresponding ground truth (top row) for all pathological geometries and a circular catheter radius of 7.5 mm. The colorbar of the reconstructed images was individually scaled from the maximum to the minimum value. Scar tissue is labelled in dark green, healthy myocardium in light green. Frequency-difference reconstruction with Laplace regularization, $\lambda = 10^{-6.5}$, and adjacent stimulation pattern.

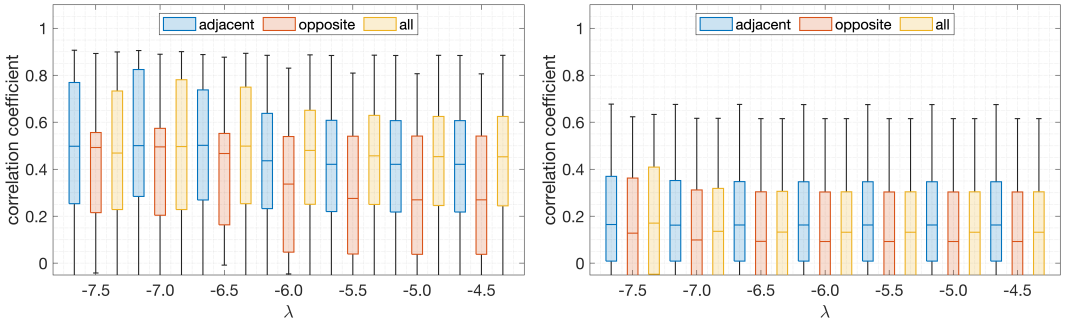

(a) Laplace regularization. **(b)** Zero-order Tikhonov regularization.

Figure 9.8: Correlation coefficient for different reconstruction parameters for point electrodes with direct tissue contact. Three different stimulation patterns are color-coded for each choice of the regularization parameter λ as noted on the horizontal axis. Laplace regularization (a) and zero-order Tikhonov regularization (b).

λ. Adjacent current injection was slightly superior to opposite current injection. The choice of the regularization parameter had little influence on the reconstruction result within the analyzed range. Adjacent current injection in combination with Laplace regularization and $\lambda = 10^{-7}$ performed best.

Fig. 9.9 compares different choices of the background image for both Laplace and zero-order Tikhonov regularization and all choices of the regularization parameter. Again, Laplace regularization was generally superior to zero-order Tikhonov regularization. Frequency-difference imaging performed best for Laplace regularization directly followed by a homo-

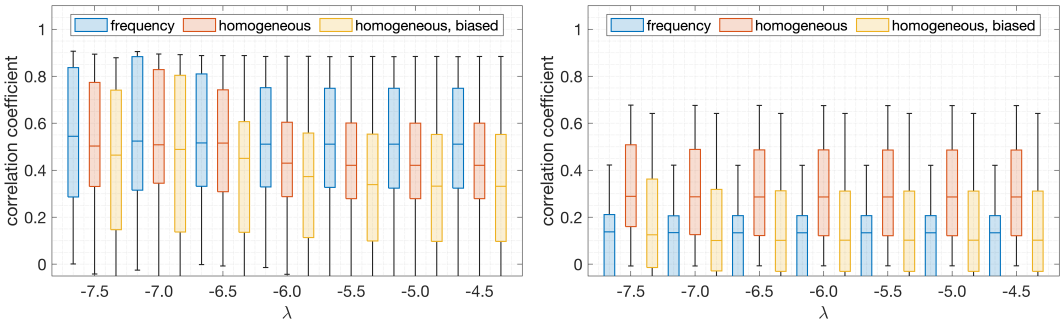

(a) Laplace regularization. **(b)** Zero-order Tikhonov regularization.

Figure 9.9: Correlation coefficient for different reconstruction parameters for point electrodes with direct tissue contact. Three different background images are color-coded for each choice of the regularization parameter λ as noted on the horizontal axis. Laplace regularization (a) and zero-order Tikhonov regularization (b).

geneous background image with σ_{BI} equalling the conductivity of healthy myocardium. A homogeneous, randomly biased background image of conductivity σ_{BII} performed worst for Laplace regularization. Again, the regularization parameter λ had little influence on the quality of the reconstruction for frequency-difference imaging.

9.3.2 Geometrical Setup

Besides the choice of above-mentioned reconstruction parameters, the actual geometrical setup took influence on the reconstruction quality and will be dug into in the following. For all upcoming comparisons, the optimal set of reconstruction parameters was chosen for each individual setup. The most common but not the exclusive choice was frequency-difference reconstruction with a regularization parameter $\lambda = 10^{-7}$, Laplace constraint and adjacent bipolar pairs for current injection and measurement.

Fig. 9.10 (a) visualizes the strong dependency of the reconstruction quality on the pathological geometry. Coarse pathological geometries such as the equal split of the issue in healthy myocardium and scar yielded correlation coefficients narrowly distributed around 0.9. Worst reconstruction quality resulted from setups with finest structures such as the line of block of 1 mm width. The distance between catheter and tissue had only little influence on the quality of the reconstruction in terms of the correlation coefficient as shown in Fig. 9.10 (b).

Fig. 9.11 (a) visualizes the influence of electrode geometry on the reconstruction quality. Point electrodes stood slightly out with a higher correlation coefficient. For all three-dimensional electrodes, neither electrode size nor geometry took significant influence on the reconstruction. Different radii of the circular catheter, on the contrary, yielded significantly different results. The smaller catheter radius of 7.5 mm performed better than the larger catheter.

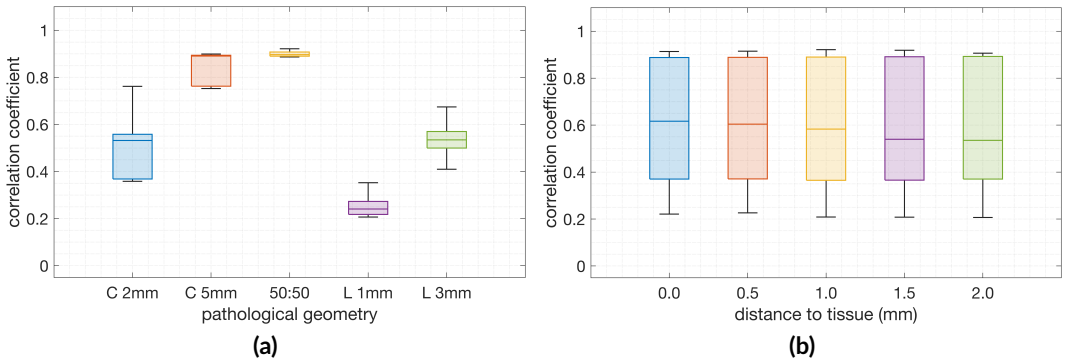

Figure 9.10: Correlation coefficient for different pathological geometries (a) and distances to the tissue (b). Best choice of reconstruction parameters for each individual setup. Pathological geometries are labelled as follows: C 2 mm: cylinder of 2 mm radius; C 5 mm: cylinder of 5 mm radius; 50:50: equal split in healthy and scar tissue; L 1 mm: linear scar of 1 mm width; L 3 mm: linear scar of 3 mm width.

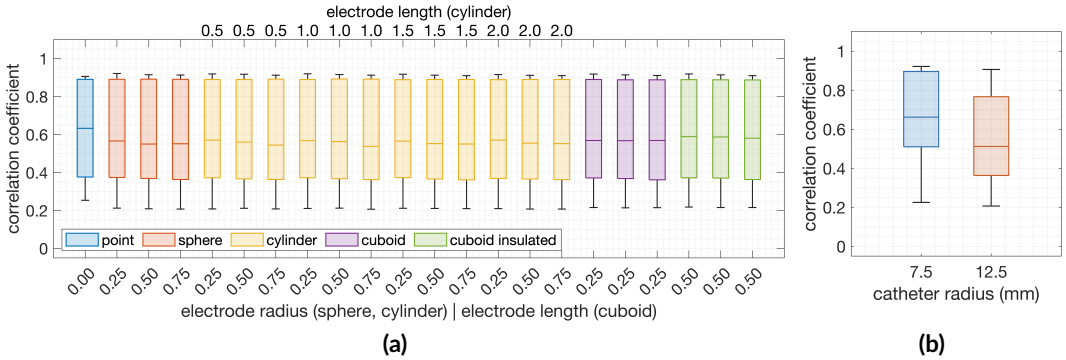

Figure 9.11: Correlation coefficient for different electrode types (a) and catheter radii (b). Best choice of reconstruction parameters for each individual setup. Electrode types are color-codes in panel (a). Dimensions are annotated on the top an bottom horizontal axis.

9.4 Discussion

This study for the first time investigated the capabilities of EIT to reconstruct relative atrial tissue conductivity from measurements with a mapping catheter. All implemented pathological geometries could be reconstructed successfully from measurements at a single catheter position. The reconstruction of the actual extent of a pathological structure was shown to be more difficult due to a lack of absolute reference. If reconstructed images were regarded to a common reference, the extent of structures might become rather comparable. In general, coarse structures were reconstructed at higher quality compared to fine structures. Due to the limited resolution of the tomographic approach, fine structures naturally tended to be blurred and reconstructed with less contrast.

The choice of the measure for reconstruction quality is crucial for all conducted analyses. In this work, the correlation coefficient and mutual information were calculated as surrogates for reconstruction quality. Both measures yielded comparable results. However, additional parameters such as the contrast between regions or the relative standard deviation could be considered for the compilation of an enhanced quality measure.

Choosing adjacent bipolar pairs for current injection and voltage measurements yielded slightly better results than opposite bipolar pairs. The fact that the number of opposite bipoles is by definition only half of the number of adjacent bipoles contributed to the inferiority. Additionally, the current path is much longer for opposite bipoles and thus integrates tissue conductivity over a longer distance than current injection from adjacent bipoles. According to the demonstrated results, afore-mentioned effects outweigh the fact that central structures are only passed directly by opposite bipolar pathways.

The optimum set of reconstruction parameters such as the regularization parameter and the choice of the regularization matrix were determined by a brute force approach in this work. Applying methods such as the L-curve to determine the optimum regularization parameter could further enhance the reconstruction quality. Additionally, two standard regularization constraints were used with the zero-order Tikhonov and the Laplace operator. Adjusting or combining different regularization constraints for the intra-cardiac application should be looked into with further detail. For clinical application, a fixed set of regularization parameters would need to be chosen or dynamically adapted based on the current measurement. Choosing the best option from a brute force approach as in this work would not be an option due to a lack of the ground truth. Convergence to an optimum set of reconstruction parameters and little dependency on the regularization parameter make a global choice feasible.

The choice of the background image is crucial for any difference-based EIT method. The approaches presented as time-difference imaging in this study may be difficult to transfer to clinical practice since the background conductivity of healthy myocardium is unknown and a random bias showed a negative influence on the reconstruction in the presented results. The conductivity of the bloodpool has been assumed to be a known factor throughout the course of this work. Although bloodpool conductivity can be easily measured in clinical practice, the influence of inaccuracies should be taken into account for time-difference approaches. However, frequency-difference imaging might be the better and more robust choice anyhow yielding the best results in this *in silico* study. Choosing two different frequencies by definition circumvents the choice of a background conductivity and includes additional information on the surrounding instead of assumptions for creating an artificial background image. Yet, the implementation in clinical hardware might be more demanding than a single measurement frequency. Entering the MHz frequency range is necessary for reaching an appropriate contrast but also challenging due to capacitive effects in the measurement equipment. Additional measurements at a second frequency by either time multiplexing or frequency multiplexing hardware do not significantly impact real-time applicability. A closer

look into the optimum choice of the measurement frequencies could further improve the results.

Despite the observed vast independence of the reconstruction quality from the distance to the tissue, the restriction to constant distances between electrodes and tissue is a major limitation of this work. Knowing that the elevation of the catheter from the tissue by few millimeters causes drops in the measured voltage amplitude in the same range as the presence of pathological structures, the assurance of tissue contact is core to meaningful measurements. An extension of this *in silico* study should further investigate the effect of varying, uneven distances between electrodes and tissue within one measurement. Ultrasound based distance measures or contact-force sensors could help to mitigate disadvantageous effects.

Although there is much room for further investigations, this pilot study elucidated the extensive potential of EIT for reconstructing relative atrial tissue conductivity from mapping catheter measurements. In a next step, *ex vivo* and *in vivo* studies should confirm the findings. Given that linear catheters with the DirectSense™ technology are already in clinical use, the step towards in human measurements with mapping catheters is a challenge but definitely within grasp.

9.5 Future Perspectives

With the circular catheter, only one possible electrode arrangement was analyzed thus far. New generation high-density mapping catheters such as the Advisor™ HD Grid (Abbott, Chicago, IL, USA) or the IntellaMap Orion™ (Boston Scientific, Malborough, MA, USA) offer a denser arrangement of electrodes. Covering also the central part of the area of interest has advantages compared to the circular catheter shape since information on the center does not need to be extrapolated.

An *in silico* model of a grid shaped catheter mimicked the Advisor™ HD Grid mapping catheter was geometrically implemented as shown in Fig. 9.12 to supersede the circular catheter of the study described above. In particular, the realization depicted in Fig. 9.12 resembles the cylindrical electrodes of the Advisor™ HD Grid. Choosing the cuboid electrode with an insulator at the rear instead could represent a geometry similar to the IntellaMap Orion™. Possible stimulation patters surpass the available options in a circular catheter. Horizontal and vertical bipoles, diagonal bipoles, as well as bipoles located at opposite edges can be defined as stimulating and measuring pairs as depicted in Fig. 9.12 (b) to (d). The close vicinity of neighboring electrodes as well as even coverage of the area of interest are advantageous for reconstruction. Especially fine structures such as the centered cylinder of 2 mm radius could be reconstructed in higher detail with a 4×4 grid compared to the circular reconstruction described above. While preliminary results indicate that reconstruction could be further improved by taking advantage of the grid arrangement, an extensive study has yet to be conducted.

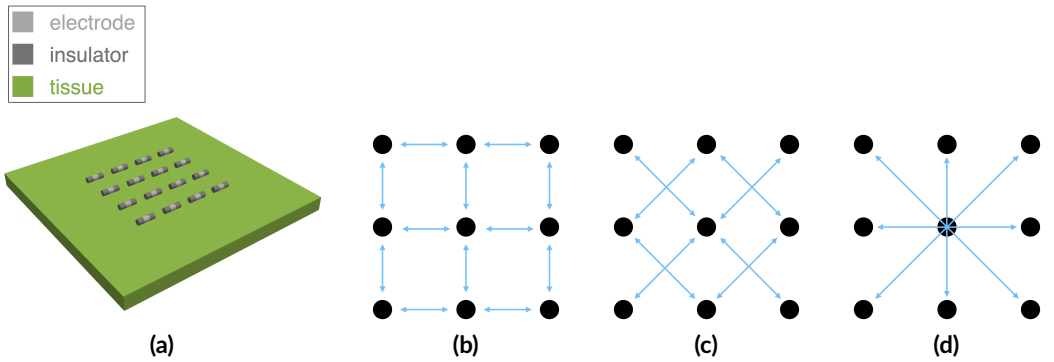

Figure 9.12: 4×4 grid shaped catheter mimicking the Advisor™ HD Grid on a slice of tissue (a). Bipolar combinations are depicted for a 3×3 grid in panels (b) to (d): horizontally and vertically adjacent bipoles, diagonally adjacent bipoles, opposite bipoles.

PART IV

CONCLUSION AND OUTLOOK

Chapter 10

Conclusion and Outlook

"Multimodal Characterization of the Atrial Substrate – Risks and Rewards of Electrogram and Impedance Mapping": Without claiming exhaustive completeness, this work shed light on a multitude of challenges and a multitude of opportunities that two fundamentally different mapping modalities offer to cardiac electrophysiology.

Remembering that the cellular composition of the atrial substrate as the target of interest can currently not be accessed directly *in human*, the combination electrogram (EGM) and local impedance (LI) based mapping seems promising. While EGMs provide information on the current spread of excitation and reflect the impact of substrate properties on excitation propagation, LI could contribute with an excitation independent estimate of tissue composition.

Both mapping modalities should undergo further investigations. For EGM based mapping, unipolar EGMs should be taken into account as well as spatio-temporal analyses relating the time courses of EGMs measured at different locations, e.g. to distinguish between near field and far field components. For LI based mapping, the inverse reconstruction of tissue conductivity should be tested *in vitro* and *in human* to delineate methodological components that need further attention for clinical application.

Special reward should be devoted to the implemented *in silico* environment for the investigation of intra-atrial LI measurements that did not only serve the purpose of this work but paved the ways for a multitude of future research projects. Supporting catheter development and further testing on methods for the reconstruction of atrial tissue conductivity are only two examples of value beyond the scope of this work.

Being aware of the risks, rewards of a modality can be exploited decisively and combined with the respective rewards of complementary modalities. This work has contributed to approaching the overall goal of picturing the pathological state of the atrial substrate by means of EGMs and LI.

List of Figures

List of Tables

References

[1] S. Silbernagel and A. Despopoulos, *Taschenatlas Physiologie*, vol. 8. Stuttgart: Thieme, 2012.

[2] D. U. Silverthorn, *Physiologie*, vol. 4. München: Pearson Studium, 2009.

[3] R. F. Schmidt and G. Thews, *Physiologie des Menschen*, vol. 26, R. F. Schmidt and G. Thews, Eds. Berlin, Heidelberg, New York: Springer, 1995.

[4] R. F. Schmidt and F. Lang, *Physiologie des Menschen mit Pathophysiologie*, vol. 30, R. F. Schmidt and F. Lang, Eds. Heidelberg: Springer, 2007.

[5] C. Schneider, *Das EPU-Labor - Einführung in die invasive elektrophysiologische Untersuchung*. Darmstadt: Steinkopff, 2005.

[6] H.-J. Trappe and H.-P. Schuster, *EKG-Kurs für Isabel*. Stuttgart: Thieme, 2017.

[7] M. Takigawa, N. Derval, P. Maury, et al., "Comprehensive multicenter study of the common isthmus in post-atrial fibrillation ablation multiple-loop atrial tachycardia." *Circulation. Arrhythmia and Electrophysiology*, vol. 11, p. e006019, 2018.

[8] G. Hindricks, T. Potpara, N. Dagres, et al., "2020 ESC guidelines for the diagnosis and management of atrial fibrillation developed in collaboration with the european association for cardio-thoracic surgery (EACTS)," *European Heart Journal*, vol. 42, pp. 373–498, 2021.

[9] M. Haissaguerre, P. Jaïs, D. C. Shah, et al., "Spontaneous initiation of atrial fibrillation by ectopic beats originating in the pulmonary veins," *New England Journal of Medicine*, vol. 339, pp. 659–666, 1998.

[10] E. J. Benjamin, P. Muntner, A. Alonso, et al., "Heart disease and stroke statistics—2019 update: A report from the american heart association," *Circulation*, vol. 139, 2019.

[11] K.-H. Kuck, J. Brugada, M. Schlüter, et al., "The FIRE AND ICE trial: What we know, what we can still learn, and what we need to address in the future." *Journal of the American Heart Association*, vol. 7, p. e010777, 2018.

[12] A. Luik, A. Radzewitz, M. Kieser, et al., "Cryoballoon versus open irrigated radiofrequency ablation in patients with paroxysmal atrial fibrillation: The prospective, randomized, controlled, noninferiority FreezeAF study," *Circulation*, vol. 132, pp. 1311–1319, 2015.

[13] M. S. Sulkin, J. I. Laughner, S. Hilbert, et al., "Novel measure of local impedance predicts catheter-tissue contact and lesion formation," *Circulation. Arrhythmia and Electrophysiology*, vol. 11, p. e005831, 2018. doi:10.1161/CIRCEP.117.005831

[14] G. H. Markx and C. L. Davey, "The dielectric properties of biological cells at radiofrequencies: applications in biotechnology," *Enzyme and Microbial Technology*, vol. 25, pp. 161–171, 1999.

[15] H. P. Schwan, "Electrical properties of tissue and cell suspensions," *Advances in Biological and Medical Physics*, vol. 5, pp. 147–209, 1957.

[16] F. Bergler, *Physikalische Chmie für Nebenfächler und Fachschüler*. Weinheim: Wiley-VCH, 2013.

[17] D. R. Lide and T. J. Bruno, *CRC handbook of chemistry and physics*, vol. 99, J. R. Rumble, Ed. Boca Raton, FL: CRC Press, 2018.

[18] P. Debye and H. Falkenhagen, "Dispersion of the conductivity and dielectric constants of strong electrolytes," *Physikalische Zeitschrift*, vol. 29, pp. 401–426, 1928.

[19] A. Chandra and B. Bagchi, "Frequency dependence of ionic conductivity of electrolyte solutions," *Journal of Chemical Physics*, vol. 112, pp. 1876–1886, 2000.

[20] K. S. Cole and R. H. Cole, "Dispersion and absorption in dielectrics I. alternating current characteristics," *The Journal of Chemical Physics*, vol. 9, pp. 341–351, 1941.

[21] J. Maxwel, *Electricity and Magnetism*. London: Oxford Press, 1892.

[22] K. W. Wagner, "Zur Theorie der unvollkommenen Dielektrika," *Annals of Physics*, vol. 40, pp. 817–855, 1913.

[23] K. R. Foster and H. P. Schwan, "Dielectric properties of tissues and biological materials: a critical review," *Crit Rev Biomed Eng*, vol. 17, pp. 25–104, 1989.

[24] R. Pethig, "Dielectrical properties of biological material: Biophysical and medical applications," *IEEE Trans. Elec. Ins.*, pp. 453–474, 1984.

[25] A. N. Tikhonov and V. Y. Arsenin, *Solutions of ill-posed problems*. Winston&Sons, New York, 1977.

[26] M. Kircher, "Towards an efficient gas exchange monitoring with electrical impedance tomography - optimization and validation of methods to investigate and understand pulmonary blood flow with indicator dilution," PhD thesis, Institute of Biomedical Engineering, Karlsruhe Institute of Technology (KIT), 2021.

[27] D. S. Holder, *Electrical Impedance Tomography: Methods, History, and Applications*, Series in Medical Physics and Biomedical Engineering. Bristol, Philadelphia: Instititute of Physics Publishing, 2005.

[28] H. Lüpschen, "Automatisierte protektive Beatmung durch Bestimmung von Ventilation und Perfusion der Lunge mittels Elektrischer Impedanztomographie," PhD thesis, Shaker Verlag, 2012.

[29] M. Takigawa, N. Derval, A. Frontera, et al., "Revisiting anatomic macroreentrant tachycardia after atrial fibrillation ablation using ultrahigh-resolution mapping: Implications for ablation." *Heart rhythm*, vol. 15, pp. 326–333, 2018.

[30] S. Sundaram, W. Choe, J. Ryan Jordan, et al., "Catheter ablation of atypical atrial flutter: a novel 3D anatomic mapping approach to quickly localize and terminate atypical atrial flutter," *Journal of Interventional Cardiac Electrophysiology*, vol. 49, pp. 307–318, 2017.

[31] T. Rostock, I. Drewitz, D. Steven, et al., "Characterization, mapping, and catheter ablation of recurrent atrial tachycardias after stepwise ablation of long-lasting persistent atrial fibrillation," *Circulation: Arrhythmia and Electrophysiology*, vol. 3, pp. 160–169, 2010.

[32] D. G. Laţcu and N. Saoudi, "High-resolution/density mapping in patients with atrial and ventricular arrhythmias," *Cardiac Electrophysiology Clinics*, vol. 11, pp. 511–524, 2019.

[33] C. Schilling, M. P. Nguyen, A. Luik, C. Schmitt, and O. Dössel, "Non-linear energy operator for the analysis of intracardial electrograms," in *IFMBE Proceedings World Congress on Medical Physics and Biomedical Engineering*, vol. 25/4, 2009, pp. 872–875.

[34] N. Pilia, C. Nagel, G. Lenis, S. Becker, O. Dössel, and A. Loewe, "ECGdeli - An open source ECG delineation toolbox for MATLAB," *SoftwareX*, vol. 13, p. 100639, 2020.

[35] J. S. Richman and J. R. Moorman, "Physiological time-series analysis using approximate entropy and sample entropy," *American Journal of Physiology-Heart and Circulatory Physiology*, vol. 278, pp. H2039–H2049, 2000.

[36] C. E. Shannon, "A mathematical theory of communication," *The Bell System Technical Journal*, vol. 27, pp. 379–423, 1948.

[37] L. A. Unger, T. G. Oesterlein, A. Loewe, and O. Dössel, "Noise quantification and noise reduction for unipolar and bipolar electrograms," in *Computing in Cardiology (CinC)*, vol. 46, Singapore, 2019.

[38] U. B. Tedrow and W. G. Stevenson, "Recording and interpreting unipolar electrograms to guide catheter ablation," *Heart Rhythm*, vol. 8, pp. 791–796, 2011.

[39] S. Schuler, M. W. Keller, T. Oesterlein, G. Seemann, and O. Dössel, "Influence of catheter orientation, tissue thickness and conduction velocity on the intracardiac electrogram," *Biomedical Engineering / Biomedizinische Technik*, vol. 58, 2013.

[40] M. Takigawa, M. Goya, H. Iwakawa, et al., "Impact of a formula combining local impedance and conventional parameters on lesion size prediction," *Journal of Interventional Cardiac Electrophysiology*, vol. 63, pp. 389–398, 2021.

[41] "Rhythmia HDx Mapping System - CLARITY for any level of complexity," https://www.bostonscientific.com/content/dam/bostonscienti fic/ep/Electrophysiology2017, online, accessed 2018-07-10.

[42] M. P. Nguyen, C. Schilling, and O. Dössel, "A new approach for automated location of active segments in intracardiac electrograms," in *IFMBE Proceedings World Congress on Medical Physics and Biomedical Engineering*, vol. 25(4), 2009, pp. 763–766.

[43] G. Lenis, N. Pilia, T. Oesterlein, A. Luik, C. Schmitt, and O. Dössel, "P wave detection and delineation in the ECG based on the phase free stationary wavelet transform and using intracardiac atrial electrograms as reference," *Biomedizinische Technik. Biomedical Engineering.*, vol. 61, pp. 37–56, 2016.

[44] S. Huck, T. Oesterlein, A. Luik, C. Schmitt, R. Wakili, and O. Dössel, "Preprocessing of unipolar signals acquired by a novel intracardiac mapping system," *Current Directions in Biomedical Engineering*, vol. 2, pp. 259–262, 2016.

[45] D. C. Shah, H. Lambert, H. Nakagawa, A. Langenkamp, N. Aeby, and G. Leo, "Area under the real-time contact force curve (force-time integral) predicts radiofrequency lesion size in an in vitro contractile model." *Journal of Cardiovascular Electrophysiology*, vol. 21, pp. 1038–1043, 2010.

[46] M. Das, J. J. Loveday, G. J. Wynn, et al., "Ablation index, a novel marker of ablation lesion quality: prediction of pulmonary vein reconnection at repeat electrophysiology study and regional differences in target values." *EP Europaces*, vol. 19, pp. 775–783, 2017.

[47] M. Das, A. Luik, E. Shepherd, et al., "Local catheter impedance drop during pulmonary vein isolation predicts acute conduction block in patients with paroxysmal atrial fibrillation: initial results of the LOCALIZE clinical trial," *EP Europace*, vol. 23, pp. 1042–1051, 2021.

[48] L. Segreti, A. De Simone, V. Schillaci, et al., "A novel local impedance algorithm to guide effective pulmonary vein isolation in atrial fibrillation patients: Preliminary experience across different ablation sites from the CHARISMA pilot study." *Journal of Cardiovascular Electrophysiology*, vol. 31, pp. 2319–2327, 2020.

[49] M. Gunawardene, P. Münkler, C. Eickholt, et al., "A novel assessment of local impedance during catheter ablation: initial experience in humans comparing local and generator measurements." *EP Europace*, vol. 21, pp. i34–i42, 2019. doi:10.1093/europace/euy273

[50] C. A. Martin, R. Martin, P. R. Gajendragadkar, et al., "First clinical use of novel ablation catheter incorporating local impedance data," *Journal of Cardiovascular Electrophysiology*, vol. 29, pp. 1197–1206, 2018.

[51] G. S. Chu, P. Calvert, P. Futyma, W. Y. Ding, R. Snowdon, and D. Gupta, "Local impedance for the optimization of radiofrequency lesion delivery: A review of bench and clinical data," *Journal of Cardiovascular Electrophysiology*, 2021. doi:10.1111/jce.15335

[52] IT'IS Foundation, "Tissue properties database v4.0," 2018. doi:10.13099/VIP21000-04-0

[53] C. Gianni, G. J. Gallinghouse, A. Al-Ahmad, et al., "Half-normal saline versus normal saline for irrigation of open-irrigated radiofrequency catheters in atrial fibrillation ablation," *Journal of Cardiovascular Electrophysiology*, vol. 32, pp. 973–981, 2021.

[54] L. A. Unger, C. M. Antón, M. Stritt, et al., "In silico study of local electrical impedance measurements in the atria - Towards understanding and quantifying dependencies in human," *IEEE Transactions on Biomedical Engineering*, pp. 1–11, 2022, ePub ahead of print. doi: 10.1109/TBME.2022.3196545

[55] S. Gabriel, R. W. Lau, and C. Gabriel, "The dielectric properties of biological tissues: II. measurements in the frequency range 10 Hz to 20 GHz," *Physics in Medicine and Biology*, vol. 41, pp. 2251–2269, 1996.

[56] S. Grimnes and O. G. Martinsen, *Bioimpedance and bioelectricity basics*. London, San Diego: Academic Press, 2000.

[57] C. Reithmann, T. Remp, E. Hoffmann, T. Matis, R. Wakili, and G. Steinbeck, "Different patterns of the fall of impedance as the result of heating during ostial pulmonary vein ablation: Implications for power titration," *Pacing and Clinical Electrophysiology*, vol. 28, pp. 1282–1291, 2005.

[58] P. C. Qian, D. M. Nguyen, M. A. Barry, et al., "Optimizing impedance change measurement during radiofrequency ablation enables more accurate characterization of lesion formation," *JACC: Clinical Electrophysiology*, vol. 7, pp. 471–481, 2021.

[59] R. van Es, J. Hauck, V. J. H. M. van Driel, et al., "Novel method for electrode-tissue contact measurement with multi-electrode catheters." *EP Europace*, vol. 20, pp. 149–156, 2017.

[60] K. Garrott, J. Laughner, S. Gutbrod, et al., "Combined local impedance and contact force for radiofrequency ablation assessment," *Heart Rhythm*, vol. 17, pp. 1371–1380, 2020.

[61] P. Kauppinen, J. Hyttinen, and M. J., "Sensitivity distribution visualizations of impedance tomography measurement strategies," *International Journal of Bioelectromagnetism*, vol. 8, pp. 63–71, 2006.

[62] "INTELLANAV MIFI™ OPEN-IRRIGATED ABLATION CATHETER, Boston Scientific Corporation," *https://www.bostonscientific.com/content/dam/bostonscientific/Rhythm%20Management/general/EP-479201-AB_IntellaNav%20MiFi%20OI%20Spec%20Sheet%20FINAL.pdf*, 2018, accessed: 2022-01-05.

[63] "INTELLANAV STABLEPOINT™ ABLATION CATHETER, Boston Scientific Corporation," *https://www.bostonscientific.com/content/dam/bostonscientific/ep/Electrophysiology%20Portfolio/Rhythmia/intellanav-stablepoint/EP-815001-AB_STABLEPOINT_SPECSHEET.pdf*, 2020, accessed: 2022-01-05.

[64] C. Geuzaine and J.-F. Remacle, "Gmsh: A three-dimensional finite element mesh generator with built-in pre- and post-processing facilities," *International Journal for Numerical Methods in Engineering*, vol. 79, pp. 1309–1331, 2009.

[65] P. G. Platonov, V. Ivanov, S. Y. Ho, and L. Mitrofanova, "Left atrial posterior wall thickness in patients with and without atrial fibrillation: data from 298 consecutive autopsies," *Journal of Cardiovascular Electrophysiology*, vol. 19, pp. 689–692, 2008.

[66] "The effect of temperature on conductivity measurement; CONDUCTIVITY METER 4520 application note: A002-001A," *http://www.jenway.com/adminimages/A02_001A_Effect_of_temperature_on_conductivity.pdf*, accessed: 2022-01-05.

[67] H. Cao, M. Speidel, J.-Z. Tsai, M. Van Lysel, V. Vorperian, and J. Webster, "FEM analysis of predicting electrode-myocardium contact from RF cardiac catheter ablation system impedance," *IEEE Transactions on Biomedical Engineering*, vol. 49, pp. 520–526, 2002.

[68] C. Gabriel, *Compilation of the dielectric properties of body tissues at RF and microwave frequencies*. Texas, USA: Occupational and Environmental Health Directorate, Radiofrequency Radiation Division, Brooks Air Force Base, 1996, report N.AL/OE-TR-1996-0037. doi:10.21236/ada303903

[69] A. Adler and W. R. B. Lionheart, "Uses and abuses of EIDORS: an extensible software base for EIT," *Physiological Measurement*, vol. 27, pp. S25–42, 2006. doi:10.1088/0967-3334/27/5/S03

[70] K.-S. Cheng, D. Isaacson, J. Newell, and D. Gisser, "Electrode models for electric current computed tomography," *IEEE Transactions on Biomedical Engineering*, vol. 36, pp. 918–924, 1989. doi:10.1109/10.35300

[71] D. Bennett, "NaCl doping and the conductivity of agar phantoms," *Materials Science and Engineering: C*, vol. 31, pp. 494–498, 2011.

[72] M. A. Kandadai, J. L. Raymond, and G. J. Shaw, "Comparison of electrical conductivities of various brain phantom gels: Developing a 'brain gel model'," *Materials Science and Engineering: C*, vol. 32, pp. 2664–2667, 2012.

[73] L. A. Unger, L. Schicketanz, T. Oesterlein, et al., "Local electrical impedance mapping of the atria: Conclusions on substrate properties and confounding factors," *Frontiers in Physiology*, vol. 12, p. 788885, 2022.

[74] D. T. Nguyen, M. Olson, L. Zheng, W. Barham, J. D. Moss, and W. H. Sauer, "Effect of irrigant characteristics on lesion formation after radiofrequency energy delivery using ablation catheters with actively cooled tips," *Journal of Cardiovascular Electrophysiology*, vol. 26, pp. 792–798, 2015. doi:10.1111/jce.12682

[75] D. T. Nguyen, K. Nguyen, L. Zheng, et al., "Effect of environmental impedance surrounding a radiofrequency ablation catheter electrode on lesion characteristics," *Journal of Cardiovascular Electrophysiology*, vol. 28, pp. 564–569, 2017.

[76] D. T. Nguyen, E. P. Gerstenfeld, W. S. Tzou, et al., "Radiofrequency ablation using an open irrigated electrode cooled with half-normal saline," *JACC: Clinical Electrophysiology*, vol. 3, pp. 1103–1110, 2017.

[77] J. Malmivuo and R. Plonsey. Oxford University Press, 1995, Chapters 25–27.

[78] G. Amorós-Figueras, E. Jorge, C. Alonso-Martin, et al., "Endocardial infarct scar recognition by myocardial electrical impedance is not influenced by changes in cardiac activation sequence," *Heart Rhythm*, vol. 15, pp. 589–596, 2018.

[79] H. Makimoto, T. Lin, A. Rillig, et al., "In vivo contact force analysis and correlation with tissue impedance during left atrial mapping and catheter ablation of atrial fibrillation," *Circulation: Arrhythmia and Electrophysiology*, vol. 7, pp. 46–54, 2014.

[80] M. Vaseghi, D. A. Cesario, M. Valderrabano, et al., "Impedance monitoring during catheter ablation of atrial fibrillation," *Heart Rhythm*, vol. 2, pp. 914–920, 2005.

[81] Q.-Q. Dong, W.-Y. Yang, Y.-P. Sun, et al., "Comparison of transthoracic echocardiography with computed tomography in evaluation of pulmonary veins," *BMC Cardiovascular Disorders*, vol. 19, p. 315, 2019.

[82] R. R. Tilz, A. Rillig, A.-M. Thum, et al., "Catheter ablation of long-standing persistent atrial fibrillation: 5-year outcomes of the Hamburg Sequential Ablation Strategy," *Journal of the American College of Cardiology*, vol. 60, pp. 1921–1929, 2012.

[83] A. Verma, R. Mantovan, L. Macle, et al., "Substrate and trigger ablation for reduction of atrial fibrillation (STAR AF): a randomized, multicentre, international trial," *European Heart Journal*, vol. 31, pp. 1344–1356, 2010.

[84] J. Vogler, S. Willems, A. Sultan, et al., "Pulmonary vein isolation versus defragmentation: The CHASE-AF clinical trial," *Journal of the American College of Cardiology*, vol. 66, pp. 2743–2752, 2015.

[85] A. Verma, C. Jiang, T. R. Betts, et al., "Approaches to catheter ablation for persistent atrial fibrillation," *The New England Journal of Medicine*, vol. 372, pp. 1812–1822, 2015.

[86] D. M. Nguyen, T. Andersen, P. Qian, T. Barry, and A. McEwan, "Electrical impedance tomography for monitoring cardiac radiofrequency ablation: a scoping review of an emerging technology," *Medical Engineering & Physics*, vol. 84, pp. 36–50, 2020.

[87] D. M. Nguyen, P. Qian, T. Barry, and A. McEwan, "Cardiac radiofrequency ablation tracking using electrical impedance tomography," *Biomedical Physics & Engineering Express*, vol. 6, p. 015015, 2020.

[88] D. M. Nguyen, P. Qian, T. Barry, and A. McEwan, "Self-weighted NOSER-prior electrical impedance tomography using internal electrodes in cardiac radiofrequency ablation," *Physiological Measurement*, vol. 40, p. 065006, 2019.

List of Publications and Supervised Theses

Journal Articles

- **Laura Anna Unger**, Carmen Martínez Antón, Michael Stritt, Reza Wakili, Annika Haas, Michael Kircher, Olaf Dössel, Armin Luik, *In Silico Study of Local Electrical Impedance Measurements in the Atria - Towards Understanding and Quantifying Dependencies in Human*, IEEE Transactions on Biomedical Engineering 2022, ePub ahead of print, doi:10.1109/TBME.2022.3196545
- **Laura Anna Unger**, Leonie Schicketanz, Tobias Oesterlein, Michael Stritt, Annika Haas, Carmen Martínez Antón. Kerstin Schmidt, Olaf Dössel, Armin Luik, *Local Electrical Impedance Mapping of the Atria: Conclusions on Substrate Properties and Confounding Factors*, Frontiers in Physiology 2022, 12:788885
- **Laura Anna Unger**, Luca Azzolin, Mark Nothstein, Jorge Sánchez, Armin Luik, Gunnar Seemann, Srinath Yeshwant, Tobias Oesterlein, Olaf Dössel, Claus Schmitt, Peter Spector, Axel Loewe, *Cycle Length Statistics during Human Atrial Fibrillation Reveal Refractory Properties of the Underlying Substrate: A Combined in Silico and Clinical Test of Concept Study*, Europace 2021, 23:i133–i142
- Armin Luik, Annika Haas, Kerstin Schmidt, **Laura Anna Unger**, Panos Tzamalis, Armin Klesius, Bernd Brüggenjürgen, Claus Schmitt, *Individualized ablation approach for left atrial tachycardia after previous catheter ablation of atrial fibrillation*, Journal of Clinical Medicine 2022, 11:1047
- Muhamed Vila, Massimo Walter Rivolta, Giorgio Luongo, **Laura Anna Unger**, Armin Luik, Lorenzo Gigli, Frederico Lombardi, Axel Loewe, Roberto Sassi, *Atrial Flutter Mechanism Detection Using Directed Network Mapping*, Frontiers in Physiology 2021, 12:749635
- Mark Nothstein, Armin Luik, Amir Jadidi, Jorge Sánchez, **Laura Anna Unger**, Eike M Wülfers, Olaf Dössel, Gunnar Seemann, Claus Schmitt, Axel Loewe, *CVAR-Seg: An Automated Signal Segmentation Pipeline for Conduction Velocity and Amplitude Restitution*, Frontiers in Physiology 2021, 12:673047
- Jorge Sánchez, Giorgio Luongo, Mark Nothstein, **Laura Anna Unger**, Javier Saiz, Beatriz Trenor, Armin Luik, Olaf Dössel, Axel Loewe, *Using Machine Learning to Characterize*

Atrial Fibrotic Substrate from Intracardiac Signals With a Hybrid in Silico and in Vivo Dataset, Frontiers in Physiology, 12:699291

- Felix Wiedmann, Christoph Beyersdorf, Xiaobo Zhou, Antonius Büscher, Manuel Kraft, Jendrik Nietfeld, Teo Puig Walz, **Laura Anna Unger**, Axel Loewe, Bastian Schmack, Arjang Ruhparwar, Matthias Karck, Dierk Thomas, Martin Borggrefe, Gunnar Seemann, Hugo A Katus, Constanze Schmidt, *Pharmacologic TWIK-Related Acid-Sensitive K+ Channel (TASK-1) Potassium Channel Inhibitor A293 Facilitates Acute Cardioversion of Paroxysmal Atrial Fibrillation in a Porcine Large Animal Model*, Journal of the American Heart Association 2020, 9:e015751
- Daniel Frisch, Tobias G Oesterlein, **Laura Anna Unger**, Gustavo Lenis, Reza Wakili, Claus Schmitt, Armin Luik, Olaf Doessel, Axel Loewe, *Mapping and Removing the Ventricular Far Field Component in Unipolar Atrial Electrograms*, Transactions on Biomedical Engineering 2020, 67:2905-2915
- Martino Alessandrini, Maddalena Valinoti, **Laura Anna Unger**, Tobias Oesterlein, Olaf Dössel, Cristiana Corsi, Axel Loewe, Stefano Severi, *A Computational Framework to Benchmark Basket Catheter Guided Ablation in Atrial Fibrillation*, Frontiers in Physiology 2018, 9:1251

Refereed Conference Articles

- **Laura Anna Unger**, Armin Luik, Annika Haas, Olaf Dössel, *Comparison of Morphology-Based and Delay-Based Measures for Reference Beat Classification during Atrial Tachycardia*, Computing in Cardiology 2020: 47:446
- **Laura Anna Unger**, Tobias G Oesterlein, Axel Loewe, Olaf Dössel, *Noise Quantification and Noise Reduction for Unipolar and Bipolar Electrograms*, Computing in Cardiology 2019, 46:288
- **Laura Anna Unger**, Tobias Oesterlein, Gunnar Seemann, Olaf Dössel, Peter Spector, Axel Loewe, *Estimating Refractory Periods during Atrial Fibrillation based on Electrogram Cycle Lengths in a Heterogeneous Simulation Setup*, Current Directions in Biomedical Engineering 2017, 3:317–320
- Leonie Schicketanz, **Laura Anna Unger**, Jorge Sánchez, Olaf Dössel, Axel Loewe, *Separating Atrial Near Fields and Atrial Far Fields in Simulated Intra-atrial Electrograms*, Current Directions in Biomedical Engineering 2021, 7:175–178
- Nick Johannes Lorenz, **Laura Anna Unger**, Armin Luik, Olaf Dössel, *Quantitative Assessment of Ventricular Far Field Removal Techniques for Clinical Unipolar Electrograms*, Current Directions in Biomedical Engineering 2021, 7:243-246
- Jorge Sánchez, Mark Nothstein, **Laura Anna Unger**, Javier Saiz, Beatriz Trénor, Olaf Dössel, Axel Loewe *Influence of Fibrotic Tissue Arrangement on Intracardiac Electrograms during Persistent Atrial Fibrillation*, Computing in Cardiology 2019, 46:342

- Tiago P Almeida, **Laura Anna Unger**, Diogo Soriano, Yin Li, Olaf Dössel, Takashi Yoneyama, Axel Loewe *Recurrence Quantification Analysis for Investigating Atrial Fibrillation Dynamics in a Heterogeneous Simulation Setup*, Annual International Conference of the IEEE Engineering in Medicine and Biology Society (EMBC) 2019, 41:2277-2280
- Claudia Nagel, Nicolas Pilia, **Laura Anna Unger**, Olaf Dössel, *Performance of Different Atrial Conduction Velocity Estimation Algorithms Improves with Knowledge about the Depolarization Pattern*, Current Directions in Biomedical Engineering 2019, 5:101-104
- Oliver Huhn, Stefan Pollnow, **Laura Anna Unger**, Olaf Dössel, Tobias Oesterlein, Armin Luik, Claus Schmitt, *High-density Mapping Reveals Short-term Reversibility of Atrial Ablation Lesions*, Current Directions in Biomedical Engineering 2018, 4:385-388
- Olaf Dössel, Tobias Oesterlein, **Laura Anna Unger**, Axel Loewe, Claus Schmitt, Armin Luik, *Spatio-temporal Analysis of Multichannel Atrial Electrograms Based on a Concept of Active Areas*, Annual International Conference of the IEEE Engineering in Medicine and Biology Society (EMBC) 2018, 40:490–493
- Mohammad Albatat, D. Ryan King, **Laura Anna Unger**, Hermenegild Arevalo, Samuel Wall, Joakim Sundnes, Jacob Bergsland, Ilangko Balasingham, *Electromechanical Model to Predict Cardiac Resynchronization Therapy*, Annual International Conference of the IEEE Engineering in Medicine and Biology Society (EMBC) 2018, 40:5446–5459

Refereed Conference Abstracts

- **Laura Anna Unger**, Carmen Martínez Antón, Tobias Oesterlein, Carina Jäger, Claus Schmitt, Olaf Doessel, Reza Wakili, Armin Luik, *Local Impedance Measurements with the INTELLANAV MIFI OI and the INTELLANAV STABLEPOINT Ablation Catheter are Linearly Related*, Heart Rhythm 2021, 21-A-6595
- **Laura Anna Unger**, Nick Johannes Lorenz, Olaf Doessel, Armin Luik, *Removing the Ventricular Far Field from Unipolar Atrial Electrograms in a Clinically Feasible Setup with a Physically Motivated Model Yields High Quality Results*, Heart Rhythm 2021, 21-A-6219
- **Laura Anna Unger**, Leonie Schicketanz, Olaf Dössel, Armin Luik, *Intra-atrial Impedance in Different Left Atrial Regions with respect to a Patient-specific Reference*, 55th Annual Conference of the German Society of Biomedical Engineering 2021
- **Laura Anna Unger**, Armin Luik, Annika Haas, Olaf Dössel, Olaf *Stability Assessment of Bipolar Coronary Sinus Sequences during Atypical Atrial Flutter*, 54th Annual Conference of the German Society of Biomedical Engineering 2020
- **Laura Anna Unger**, Tobias Oesterlein, Annika Haas, Armin Luik, Olaf Doessel, *Characterizing and Localizing Zones of Critical Conduction during Atrial Tachycardia Demands Ultra-high-resolution Electroanatomical Mapping*, Atrial Signals 2019

- **Laura Anna Unger**, Olaf Doessel, Claus Schmitt, Armin Luik, *Substrate Characterization with Local Impedance Mapping*, Annual International Conference of the IEEE Engineering in Medicine and Biology Society (EMBC) 2019
- **Laura Anna Unger**, Tobias G Oesterlein, Peter S Spector, Armin Luik, Claus Schmitt, Axel Loewe, Olaf Doessel, *Cycle Length Statistics During Atrial Fibrillation Reflect Refractory Properties of the Underlying Substrate*, 14th Annual Scientific Meeting of the European Cardiac Arrhythmia Society (ECAS) 2018
- **Laura Anna Unger**, Tobias Oesterlein, Gunnar Seemann, Olaf Dössel, Peter Spector, Axel Loewe, *Estimating Refractory Periods during Atrial Fibrillation based on Electrogram Cycle Lengths in a Heterogeneous Simulation Setup*, Atrial Signals 2017

Invited Talks

- **Laura Anna Unger**, *Electrode Size, Shape, and Configuration, Unipolar or Bipolar – What do we See and what do we Need to See?*, Atrial Signals 2021

Committee Memberships

- Olaf Dössel, Claus Schmitt, Armin Luik, **Laura Anna Unger**, Axel Loewe, Andrea Radzewitz, Organization Committee of Atrial Signals 2021, Karlsruhe, Germany

Supervised Student Theses and Projects

- Lena Heinemann, *Local Impedance Measurements in the Atria*, Student Research Project, Institute of Biomedical Engineering, Karlsruhe Institute of Technology (KIT), 2021–today
- Leonie Schicketanz, *Atrial Signal Analysis*, Student Research Project, Institute of Biomedical Engineering, Karlsruhe Institute of Technology (KIT), 2018–today
- Erik Oberschulte, *Low-Energy Pacing to Control Cardiac Arrhythmia*, Bachelor Thesis, Institute of Biomedical Engineering, Karlsruhe Institute of Technology (KIT), 2021–today
- Lena Heinemann, *Comparison of Unipolar and Bipolar Electrogram Morphology for Different Wave Propagation Phenomena*, Bachelor Thesis, Institute of Biomedical Engineering, Karlsruhe Institute of Technology (KIT), 2020–2021

- Leonie Schicketanz, *Separation of Atrial Near and Far Field Components in Electrograms during Atrial Tachycardia*, Bachelor Thesis, Institute of Biomedical Engineering, Karlsruhe Institute of Technology (KIT), 2019–2020
- Nick Johannes Lorenz, *Ventricular Far Field Removal*, Internship, Institute of Biomedical Engineering, Karlsruhe Institute of Technology (KIT), 2020–2021
- Jeanne Koch, *Enhancing Conduction Velocity Estimation by Atrial Electrogram Analysis*, Bachelor Thesis, Institute of Biomedical Engineering, Karlsruhe Institute of Technology (KIT), 2019–2020
- Sophie An, *Automated Analysis of Atrial Flutter Recorded with the Carto3 System*, Student Research Project, Institute of Biomedical Engineering, Karlsruhe Institute of Technology (KIT), 2019–2020
- Nick Johannes Lorenz, *Quantitative Assessment of Algorithms for Ventricular Far Field Removal in a Clinical Context*, Bachelor Thesis, Institute of Biomedical Engineering, Karlsruhe Institute of Technology (KIT), 2020
- Michael Stritt, *Local Impedance Mapping*, Master Thesis, Institute of Biomedical Engineering, Karlsruhe Institute of Technology (KIT), 2019–2020
- Claudia Nagel, *Robust Conduction Velocity Estimation in a Clinical Setting*, Master Thesis, Institute of Biomedical Engineering, Karlsruhe Institute of Technology (KIT), 2018–2019
- Simon Süß, *Determination of the Information Gain by Estimating the Instantaneous Phase of Biosignals*, Bachelor Thesis, Institute of Biomedical Engineering, Karlsruhe Institute of Technology (KIT), 2018
- Michael Stritt, *Signal Analysis of Endocardial Electrograms - Assessing High-Density Mapping*, Student Research Project, Institute of Biomedical Engineering, Karlsruhe Institute of Technology (KIT), 2018

Awards & Grants

- Abstract Award Finalist, Atrial Signals 2019, *Characterizing and Localizing Zones of Critical Conduction during Atrial Tachycardia Demands Ultra-high-resolution Electroanatomical Mapping*
- DAAD Travel Scholarship, Computing in Cardiology (CinC) 2019, Singapore